Efficient Simulation of Tracer Transport in Fractured Porous Media and Data-Driven Aperture Estimation

Michael Liem

Dissertation ETH No. 30234

DISS. ETH NO. 30234

EFFICIENT SIMULATION OF TRACER TRANSPORT IN FRACTURED POROUS MEDIA AND DATA-DRIVEN APERTURE ESTIMATION

A thesis submitted to attain the degree of

DOCTOR OF SCIENCES
(Dr. sc. ETH Zurich)

presented by

MICHAEL ALOIS LIEM
MSc ETH ME, ETH Zurich
born on 02.07.1992

accepted on the recommendation of

Prof. Dr. Patrick Jenny, examiner
Prof. Dr. Stephan K. Matthai, co-examiner
Dr. Daniel Meyer-Massetti, co-examiner

2024

Michael Liem
michael.alois.liem@alumni.ethz.ch

Institute of Fluid Dynamics (IFD)
ETH Zurich
Sonneggstrasse 3
8092 Zurich
Switzerland
https://ifd.ethz.ch

DOI: 10.3929/ethz-b-000685017

Titlepage: Background color gradient by Mateus Andre, Freepik

Abstract

Subsurface applications such as geothermal heat extraction or CO_2 sequestration are vital for solving today's energy and climate challenges. Their reservoir rock typically consists of fractured porous media, whose fractures can greatly affect flow, transport, and mechanics. Accurate and efficient modelling of the relevant physical processes and characterising the related parameters are crucial for performance estimation and risk assessment. This simulation-based thesis aims to enhance these aspects.

Time-dependent hyperbolic partial differential equations (PDEs) are commonly used for modelling transport phenomena and seismic activity. Adaptive time stepping methods, like the adaptive conservative time integration (ACTI) scheme, improve the efficiency of explicit time integration by allowing variable local time steps. We extend ACTI to tracer transport in fractured porous media, achieving accurate results while reducing computational costs by orders of magnitude compared to global time stepping.

Limited observability of subsurface reservoirs and substantial uncertainties, particularly concerning fractures and their apertures, pose challenges to accurate modelling. Ensemble-based data assimilation (DA) methods, like the ensemble smoother with multiple data assimilation (ESMDA), are established tools for reducing uncertainty in model parameters and improving simulation results. We demonstrate the significant impact of measurement strategies and matrix permeability on DA results, highlighting the utility of intermediate measurements during reservoir stimulation and the influence of matrix permeability on fracture parameter estimation.

Constructing a prior ensemble that accurately reflects available knowledge is crucial for ensemble-based DA methods. We introduce the far-field stress approximation (FFSA), a proxy model which projects the far-field stresses onto the fracture planes and approximates shear displacement with linear elastic theory. The FFSA efficiently generates reasonable prior realisations of fracture apertures in a realistic two-dimensional fracture network. The resulting posterior ensemble matches the flow and transport behaviour of the synthetic reference at measurement locations. It improves the estimation of the fracture apertures, markedly outperforming results from prior ensembles based on naïve stochastic approaches.

In conclusion, this thesis contributes to a more efficient and accurate simulation of fractured porous media, paving the way for improved reservoir management and decision-making in various subsurface applications.

Zusammenfassung

Unterirdische Verfahren wie die Entnahme geothermischer Wärme oder CO_2 Speicherung spielen eine entscheidende Rolle bei der Bewältigung aktueller Herausforderungen in den Bereichen Energiegewinnung und Klimaschutz. Diesen Verfahren nutzen Reservoirgesteine, welche üblicherweise aus von Brüchen durchzogenen porösen Medien bestehen. Die Brüche in diesen Gesteinen können dabei einen erheblichen Einfluss auf Strömungsverhalten, Transportprozesse und mechanischen Eigenschaften haben. Daher ist eine präzise und effiziente Modellierung der relevanten physikalischen Prozesse und Charakterisierung der zugehörigen Parameter äusserst wichtig, um Leistungsfähigkeit und Risikopotenzial der Verfahren abschätzen zu können. Die vorliegende simulationsbasierte Dissertation zielt darauf ab, diese Aspekte zu verbessern.

Zeit-abhängige hyperbolische partielle Differenzialgleichungen sind ein weitverbreitetes Werkzeug zur Modellierung von Transportverhalten und seismische Aktivitäten. Adaptive Zeitschrittverfahren, wie das *Adaptive Conservative Time Integration* (ACTI) Schema, steigern die Effizienz expliziter Zeitintegration, indem sie variable lokale Zeitschritte erlauben. Diese Arbeit erweitert das ACTI-Verfahren und wendet es auf Tracer-Transport in geklüftet-porösen Medien an. Dabei erzielen wir präzise Resultate, während die Rechenkosten im Vergleich zur globalen Zeitintegration um Grössenordnungen reduziert werden.

Die limitierte Einsehbarkeit unterirdischen Reservoire und erheblichen Unsicherheiten, insbesondere bezüglich der Bruchstrukturen und deren Öffnungen, stellen grosse Herausforderungen an ein korrektes Modellieren dar. Ensemble-basierte Datenassimilierungsmethoden, wie der *Ensemble Smoother for Multiple Data Assimilation* (ESMDA), sind etablierte Werkzeuge, um Unsicherheiten in den Modellparametern zu verringern und Genauigkeit von Simulationsergebnissen zu steigern. Unsere Untersuchungen zeigen einen wesentlichen Einfluss von Messstrategien und Matrixpermeabilität auf die ESMDA Resultate. Im Besonderen wird die Bedeutung von Messungen während der Reservoir-Stimulierung und der Effekt der Matrixpermeabilität auf die präzise Bestimmung der Bruchparametern hervorgehoben.

Wesentlich für ensemble-basierte Datenassimilierungsmethoden sind zudem ein Prior-Ensemble, welches das verfügbare Wissen über das System umfassend widerspiegelt. In diesem Zusammenhang stellen wir die *Far-Field Stress Approximation* (FFSA) vor, ein Proxy-Modell, das den Fernfeldstress auf die Bruchebenen projiziert und Scherverschiebungen mit linearer Elastizität approximiert. Die FFSA ermöglicht es, auf effiziente Weise plausible Realisierungen der Bruchöffnungen in

einem realistischen zwei-dimensionalen Bruchnetzwerk zu erzeugen. Das daraus resultierende Posterior-Ensemble reproduziert das Strömungsverhalten der synthetischen Referenz an den Messpunkten und verbessert die Abschätzung der Spaltöffnungen. Es übertrifft dabei die Resultate aus zwei naiven stochastischen Ansätzen deutlich.

Zusammenfassend leistet diese Dissertation einen Beitrag zu einem effizienteren und genaueren Simulieren von geklüftet-porösen Medien. Sie ebnet dabei den Weg für ein verbessertes Reservoirmanagement und unterstützt Entscheidungsprozesse in verschiedenen unterirdischen Anwendungen.

Acknowledgments

The successful completion of this thesis would not have been possible without the support of extraordinary people.

First and foremost, I would like to express my gratitude to my supervisor, Patrick Jenny, for his continuous support throughout my PhD. Your guidance was always available when needed, yet you also gave me plenty of freedom and autonomy, which I genuinely appreciate. Your belief in me and my work kept me motivated even during challenging times. Also, I will always look back on our legendary group adventures to the mountains with great joy. Thank you!

Next, I want to thank my co-supervisor, Stephan Matthai, for his dedication and the countless online meetings. You have taught me an incredible amount about the subsurface and fractures, even through fossils in the sandstones of conference hotel facades. Thank you for continuously pushing me towards more realistic scenarios, significantly enhancing the value and relevance of my work.

Extraordinary thanks go to Giulia Conti and Ranit Monga, who not only shared the office with me but also became good friends. I always looked forward to coming to the office, knowing you would be there. Moreover, the journeys to various conference venues would not have been the same without you. Giulia, thank you for the collaboration on the FFSA, for providing the geomechanical reference realisation used in Chapter 6, and for all your invaluable feedback and support. Ranit, thank you for accompanying me on this long journey, starting with our Master's Theses almost seven years ago.

I am grateful to Daniel Meyer-Massetti for being my co-examiner and for the insightful discussions on statistical methods and various other topics. Special thanks go to Maria and Bianca for their great and kind support in administrative manners and beyond. I would also like to thank my colleagues at IFD: Former and present members of our group include Anna, Robert, Franca, Philipp, Valentin, Stephan, Nemanja, Rajdeep, Thomas, Lorenz, Amir, Daniel O., Pasha, Oliver, Justin, Arthur, Sun, Kirstóf, Heinrich, Lukas, Daniel S., Shangyi, Yijun and Niklaus. Working at the institute was a pleasure thanks to you all.

Further, I want to thank Eddy for the interesting and fruitful discussions and helpful inputs. I'm looking forward to working with you. Thanks also to the ETH cluster support team for assisting me with the numerous issues I encountered while running countless simulations on the Euler cluster.

Finally, a huge thank you to my friends, especially Helen, Jenny, Philipp, Kerrin, Michi and Darya, and my family, Ursi, Werni, Barbara, Deborah and Leandra. Your support was invaluable, but even more so was the distraction from work.

Funding for this research was provided by the Swiss National Science Foundation Grant No. 178922 and ETH Zurich.

Contents

1 Introduction

Ensuring access to affordable, reliable, sustainable and modern energy for all is a key challenge of our time and one of the 17 sustainable development goals of the United Nations (United Nations, 2023, see also sdgs.un.org). While the amount of renewable energy obtained from water, wind and sun is increasing, we still largely depend on energy obtained from the subsurface, particularly oil, coal and natural gas (Energy Institute, 2023). The transition towards renewable energy sources does not lessen the importance of the subsurface. It remains crucial as a provider of energy and minerals and as a repository for long-term storage of waste products unwanted on Earth's surface or in the atmosphere. In the following, we have a closer look at some subsurface applications.

Petroleum engineering has historically been at the forefront of subsurface research. Oil and natural gas currently account for approximately 55% of the world's primary energy consumption (Energy Institute, 2023). Nevertheless, these resources are finite, and their utilisation contributes significantly to CO_2 emissions. One of the challenges in petroleum engineering is maximising resource extraction (enhanced oil recovery techniques, exploration of unconventional reserves such as shale gas) while minimising their environmental impact.

Harnessing geothermal energy in proximity to tectonic plate boundaries offers a renewable and sustainable energy source, as production roughly balances recharge dominated by the convection of magma and hot water (Stefansson, 2000; O'Sullivan et al., 2010). Countries such as Kenya, Iceland and New Zealand are successfully generating a significant portion of their energy from such convective geothermal systems. Away from tectonic plate boundaries, accessing geothermal heat suitable for electricity generation often requires drilling into dry and impermeable rocks at several kilometres depth. Enhanced geothermal systems (EGS) have emerged as a solution to this challenge, aiming to enhance the rock permeability through reservoir stimulation (Jia et al., 2022). While EGS is not strictly renewable due to the slow conductive thermal recharge in hot dry rocks compared to the production rate, it has the potential to bridge the gap until fully renewable clean energy is available in sufficient quantities.

In Switzerland, EGS projects in Basel and St. Gallen were stopped after causing earthquakes that were clearly felt by the population and resulted in minor non-structural damage (Häring et al., 2008; Deichmann & Giardini, 2009; Edwards et al., 2015). Nevertheless, Switzerland plans to produce 4.4 TWh of geothermal electricity annually by 2050, with new EGS projects currently in the planning and exploration phases (Driesner et al., 2021). Ongoing research at the Grimsel Test

Site and Bedretto Lab, two underground research laboratories, provides valuable insights, particularly into the physics of induced earthquakes during hydraulic stimulation (Amann et al., 2018; Gischig et al., 2020). An additional challenge lies in gaining a deeper understanding of the Swiss subsurface, which is crucial for identifying potential EGS sites and mitigating their seismic risks.

Carbon capture and storage (CCS) is a potential key instrument to mitigate climate change (e.g. Metz et al., 2005; Bui et al., 2018). Capturing CO_2 is most efficient at locations with high concentrations, e.g. at fossil fuel and waste-based power plants or in cement production. Subsequently, the CO_2 is compressed into supercritical form, transported, and stored in a suitable location. Subsurface reservoirs have the potential to store CO_2 permanently through physical and geochemical trapping (e.g. Lu et al., 2013). The former includes confining layers (caprocks) and capillary trapping, and the latter encompasses dissolution into formation fluids and mineralisation. Several (pilot) CCS projects are in operation or planning (e.g. Gunnarsson et al., 2018; Yang et al., 2023). One challenge in CCS is the accurate prediction and monitoring of CO_2 migration over extensive time periods, which is essential for ensuring storage sites' long-term effectiveness and safety (e.g. Shao et al., 2021; Flemisch et al., 2024).

Radioactive waste from nuclear power plants, as well as from medicine, industry and research, needs to be stored safely. Switzerland anticipates more than $40\,000\,\mathrm{m}^3$ of accumulated radioactive waste by the mid-21$^{\mathrm{st}}$ century, including $1500\,\mathrm{m}^3$ of high-level waste (Churakov et al., 2020). Geological disposal is generally considered the safest long-term solution, and the first sites are already in operation. In Switzerland, experiments in the Mont Terri rock laboratory provide valuable insights (Bossart et al., 2018). The incredibly long time scales involved in radioactive waste storage pose great challenges for experiments and numerical simulations (Tsang et al., 2015).

1.1 Scope of this work

These subsurface applications have in common that a thorough understanding of the reservoirs is crucial for predicting performance and assessing risks. This task includes the understanding and modelling of the relevant physical processes and the characterisation of related parameters. We thereby identify two specific needs that this thesis is addressing:

1. Improve the efficiency of transport algorithms in fractured porous media, starting with hyperbolic scalar tracer transport.

2. Improve the characterisation of uncertain fracture properties, especially their apertures.

The most significant scientific contributions of this thesis are as follows:

- Decreasing the computational costs of explicit time integration by orders of magnitude with the adaptive conservative time integration (ACTI) scheme compared to global time stepping, leading to efficient and accurate simulation results for tracer transport in fractured porous media (Chapter 3).
- Demonstrating the significant influence of measurement strategies and matrix permeability on estimating fracture properties (Chapter 5).
- Underlining the importance of accurate prior modelling in ensemble-based data assimilation by introducing the far-field stress approximation (FFSA), a proxy model for aperture calculation in shear-dominated regimes (Chapter 6).

In addition, this thesis summarises the fundamental theory and reviews the latest advancements: Chapter 2 introduces flow, transport and mechanics in fractured porous media and summarises existing simulation techniques. Chapter 4 provides an overview of data assimilation techniques, focussing on ensemble-based methods and their application to fractured porous media. Finally, Chapter 7 concludes the work and offers possible future directions.

2 Fractured Porous Media

2.1 Porous media

A porous medium comprises a solid matrix forming the material's skeleton and a void space (or pore space) which is typically filled with one or more fluids (e.g. water, air, CO_2, or oil). For a detailed definition, see e.g. Bear (1988). The ratio of pore volume V_{pores} over total volume V_{total}, i.e.

$$\phi = \frac{V_{\text{pores}}}{V_{\text{total}}} \ , \tag{2.1}$$

is called the porosity. Various materials, including rocks, bones, wood, cement, or ceramics, can be regarded as porous media. In modelling porous media, a distinction is made between microscopic behaviour at the pore scale and macroscopic behaviour at the representative elementary volume (REV) scale. An REV is defined as the domain size above which an averaged quantity becomes approximately constant (Bear, 1988). This concept allows for the modelling of quantities that vary continuously in space. This work exclusively focuses on porous media at the macroscopic scale.

2.1.1 Flow in porous media

Fluids can move through porous media when their pores are interconnected. In 1856, Henry Darcy laid the foundation for understanding fluid flow in porous media by formulating what is now known as Darcy's law (Darcy, 1856; Brown, 2002). In his experiments with sand filters, he observed that the flow rate Q of water through a vertical column of sand is proportional to the cross-sectional area A of the column, proportional to the difference in the hydraulic head $h_1 - h_2$, and inversely proportional to the length of the column L, i.e.,

$$Q = \kappa A \frac{h_1 - h_2}{L} \ . \tag{2.2}$$

The hydraulic (or piezometric) head is defined as

$$h = z + \frac{p}{\rho g} \tag{2.3}$$

and describes the energy per unit weight (ρg) of the fluid. Here, z is the elevation, p is the pressure, ρ is the density of the fluid, and g is the gravitational acceleration.

The velocity head is omitted here because the typically low fluid velocity in porous media means its contribution is usually negligible. The subscripts 1 and 2 refer to the location up- and downstream of the sand column, respectively. Darcy observed that the proportionality constant κ depends on the permeability of the sand. Later, this constant was named hydraulic conductivity and identified as

$$\kappa = \frac{k\rho g}{\mu} \,, \tag{2.4}$$

with the intrinsic permeability k of the porous medium and dynamic viscosity μ of the fluid.

Permeability describes the ability of a porous medium to allow fluid flow through it, making it a crucial parameter in various subsurface applications. The SI unit of permeability is m^2, often measured in millidarcies (md), where $1\,\mathrm{d} \approx 10^{-12}\,\mathrm{m}^2$. Typical permeability values span many orders of magnitude, starting from $10^{-7}\,\mathrm{m}^2$ for clean gravel up to $10^{-20}\,\mathrm{m}^2$ for fresh granite (Bear, 1988).

The specific discharge, also known as Darcy velocity or volumetric flux density, is defined as

$$q = \frac{Q}{A} \,. \tag{2.5}$$

It describes the flow rate per unit cross-sectional area of the porous medium. While q has the units of velocity, it differs from the average effective flow velocity (or pore velocity), given by

$$a = \frac{Q}{A_{\mathrm{pores}}} \simeq \frac{q}{\phi} \,. \tag{2.6}$$

Note that q and a are macroscopic quantities that are continuous in space and thus rely on the REV concept. The actual local flow field at the pore scale can be very complex.

In three dimensions, Darcy's law in differential form reads

$$\mathbf{q} = -\frac{\mathbf{K}}{\mu} \left(\nabla p - \rho \mathbf{g}\right) \,, \tag{2.7}$$

where $\mathbf{K}$ is the potentially anisotropic permeability tensor. This equation can be derived from the Stokes equation assuming a viscous resisting force that is linear with the velocity; for a rigorous derivation see e.g. Neuman (1977).

Darcy's law as presented in Eq. (2.7) is applicable to the steady-state laminar (i.e. low Reynolds number) flow of a single-phase, incompressible Newtonian fluid through a saturated, homogeneous porous medium. Thermal and chemical effects must be negligible. Several extensions to Darcy's law have been developed to relax one or more of these restrictions. For instance, the Forchheimer term is introduced for flows with high Reynolds numbers, accounting for inertial effects. The Brinkman term accounts for viscous effects that become significant for very small pore sizes. Multiphase flow in porous media can be modelled with the concept of relative permeability.

Elliptic pressure equation

Mass conservation of the fluid phase in a porous medium is described by the continuity equation

$$\frac{\partial(\phi\rho)}{\partial t} + \nabla \cdot (\rho \mathbf{q}) = S \,, \tag{2.8}$$

where the source term S represents the generation of fluid mass per unit volume per unit time. Assuming both the fluid and matrix of the porous medium are incompressible, this equation reduces to $\nabla \cdot \mathbf{q} = \dot{q}_{\text{Source}}$. In the absence of gravitational forces (i.e., only horizontal flow), we obtain the elliptic pressure equation

$$\nabla \cdot \left(\frac{\mathbf{K}}{\mu} \nabla p \right) + \dot{q}_{\text{Source}} = 0 \,. \tag{2.9}$$

The source term $\dot{q}_{\text{Source}} = S/\rho$ describes the volumetric flow rate ensuing from a source or sink per unit volume, where $\dot{q}_{\text{Source}} > 0$ corresponds to fluid injection and $\dot{q}_{\text{Source}} < 0$ to fluid extraction.

Pressure diffusion equation

For slightly compressible fluid and pores, i.e. $\rho = \rho(p)$ and $\phi = \phi(p)$, we obtain

$$\phi \rho c_t \frac{\partial p}{\partial t} - \frac{k\rho}{\mu} \left(\nabla^2 p + c_f \left(\nabla p \right)^2 \right) = S \tag{2.10}$$

from Eqs. (2.7) and (2.8) (see e.g. Zimmerman, 2017), where we assume a homogeneous isotropic medium (i.e., $\mathbf{K} = k\mathbf{I}$). The total compressibility

$$c_t = \frac{1}{\phi\rho} \frac{\partial(\phi\rho)}{\partial p} = \frac{1}{\phi} \frac{\partial \phi}{\partial p} + \frac{1}{\rho} \frac{\partial \rho}{\partial p} = c_\phi + c_f \tag{2.11}$$

is a combination of the pore compressibility c_ϕ and the compressibility of the fluid c_f. The term $c_f \left(\nabla p \right)^2$ is negligible for liquids, and we can rearrange Eq. (2.10) to the pressure diffusion equation

$$\frac{\partial p}{\partial t} = \frac{k}{\mu \phi c_t} \nabla^2 p \,. \tag{2.12}$$

Note that we neglect the source term here. The hydraulic diffusivity $D_H = \frac{k}{\mu \phi c_t}$ describes the rate at which fluid pressure diffuses through a porous medium. A pressure disturbance travels approximately a distance of $R = \sqrt{4 D_H t}$ per time t.

2.1.2 Transport in porous media

Transport phenomena play a crucial role in numerous applications involving porous media. Fluid tracers, for example, are used for characterising subsurface reservoirs and mapping groundwater flow paths. Heat transport is a critical factor in enhanced geothermal systems (EGS). Moreover, understanding the migration of CO_2 is essential for its safe and permanent underground storage. In this work, our focus is specifically on tracer transport.

We can calculate the transport of a scalar concentration c in a porous medium with the advection-diffusion equation

$$\frac{\partial(\phi c)}{\partial t} + \nabla \cdot (\phi c \, \mathbf{v}) - \nabla \cdot (D \nabla(\phi c)) - R = 0 \, , \tag{2.13}$$

where $\mathbf{v}$ is the advection speed, D is the diffusion coefficient, and R is the source term. Here, we assume that the density of the tracer substance is constant. Therefore, the conserved quantity is the tracer volume per unit volume, i.e., the product of porosity and scalar concentration ϕc. The advection speed corresponds to the average pore velocity (i.e., $\mathbf{v} = \mathbf{a} = \mathbf{q}/\phi$).

Neglecting diffusion ($D \to 0$), we can rewrite Eq. (2.13) as the hyperbolic advection equation

$$\phi \frac{\partial c}{\partial t} + \mathbf{q} \cdot \nabla c - \dot{q}_{\text{Source}} c_{\text{Source}} = 0 \, , \tag{2.14}$$

where we assume both the fluid and the matrix of the porous medium are incompressible. Note that Eq. (2.14) is not written in the conservation form.

2.1.3 Mechanics of porous media

Mechanical processes are omnipresent in the subsurface, where reservoir rocks are constantly subjected to tectonic stresses (Heidbach et al., 2018) and overburden pressure. Additional forces can arise from pressurised fluids, thermal variations and chemical reactions. Understanding these interactions and predicting the stability and evolution of subsurface structures is crucial in any subsurface application.

The static force balance in a solid material in the absence of volume forces is

$$\nabla \cdot \boldsymbol{\sigma} = 0 \, , \tag{2.15}$$

where $\boldsymbol{\sigma}$ is the stress tensor. Assuming linear elasticity of the porous medium, the stress tensor is related to the displacement vector $\mathbf{u}$ by

$$\boldsymbol{\sigma} = \lambda \, (\nabla \cdot \mathbf{u}) \, \mathbf{I} + G \left(\nabla \mathbf{u} + \nabla \mathbf{u}^T \right) \, , \tag{2.16}$$

where $\mathbf{I}$ is the identity matrix. Lamé's first parameter is given by

$$\lambda = \frac{E\nu}{(1-2\nu)(1+\nu)} \tag{2.17}$$

and the shear modulus G (also called Lamé's second parameter) is calculated as

$$G = \frac{E}{2(1+\nu)} \tag{2.18}$$

using Young's modulus E and Poisson's ratio ν.

Using the Cauchy stress tensor, the normal stress acting on a virtual plane in the intact material is given by

$$\sigma_n = -\hat{\mathbf{n}} \cdot (\boldsymbol{\sigma} \cdot \hat{\mathbf{n}}) \ , \tag{2.19}$$

where $\hat{\mathbf{n}}$ is the unit normal vector of the virtual plane. By this definition, σ_n is positive for compressive stress and negative for tensile stress. The shear stress in the direction of a unit tangent vector $\hat{\mathbf{t}}$ is expressed as

$$\sigma_s = \hat{\mathbf{t}} \cdot \left(\mathbf{I} - \hat{\mathbf{n}} \cdot \hat{\mathbf{n}}^T\right) \cdot (\boldsymbol{\sigma} \cdot \hat{\mathbf{n}}) \ . \tag{2.20}$$

2.2 Fractures

Fractures represent displacement discontinuities within a material body. They are three-dimensional structures consisting of two opposing surfaces along which material cohesion is lost, thereby separating the material body into two or more parts (Pollard & Aydin, 1988; Hargitai et al., 2021). Fractures exist in most rocks (see Fig. 2.1 for some examples) and can significantly impact flow and transport (Long & Witherspoon, 1985; Matthäi & Belayneh, 2004; Geiger et al., 2004; Johnston et al., 2005; Geiger et al., 2010). They range from micro-cracks at the length scale of grains to several metre-long joints and can form tectonic rifts and faults (e.g., Rhine Graben, San Andreas Fault, East African Rift) extending up to a few thousand kilometres. The following sections discuss the creation of fractures due to rock failure and the most important fracture parameters.

2.2.1 Rock failure

Fractures form when the local stress concentration (typically around flaws or at crack tips) exceeds the material's strength (Griffith, 1921; Westergaard, 1939; Irwin, 1957). The majority of fractures result from tensile failure, shear failure, or a combination of both. The following section is based on the work of Zoback (2007).

Tensile failure requires a negative effective normal stress on the fracture plane

$$\sigma_{\text{eff}} = \sigma_n - p_f \ , \tag{2.21}$$

where σ_n is the normal stress on the fracture plane, and p_f is the fluid pressure within the fracture. Due to the low tensile strength of rocks, even a small amount of excess pressure is sufficient to initiate the growth of fractures that are longer

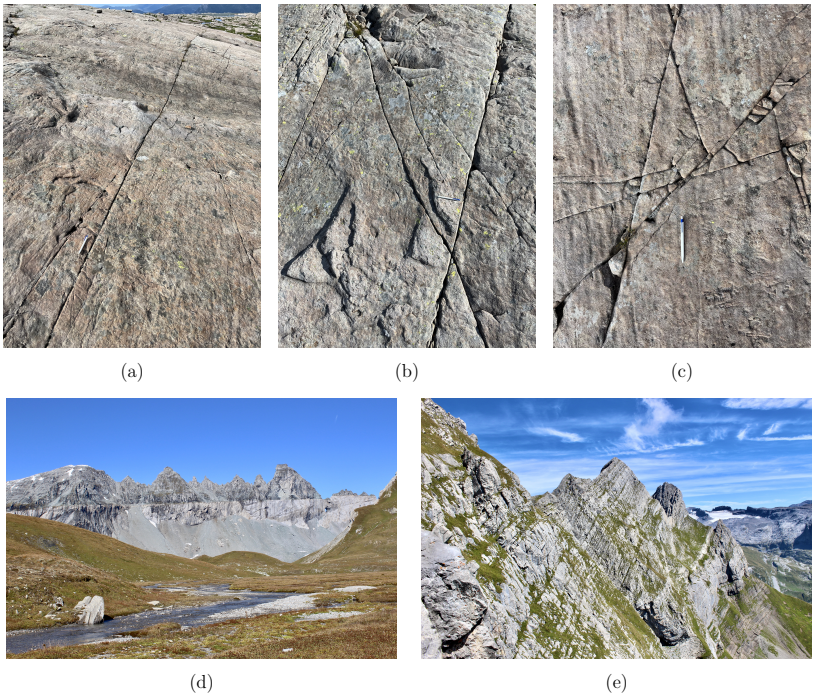

Figure 2.1: Examples of fractured rock: Old Red Sandstone of the Hornelen Basin in Western Norway (a-c), Tschingelhörner with the prominent Glarus thrust (d) and south slopes of Rigidalstock and Spitzmann in Engelberg (e). Photos taken by the author.

than a few decimetres. The resulting fractures, commonly referred to as joints (opening-mode fractures, Mode I), form perpendicular to the maximum tensile (or minimum compressive) principal stress. The relative displacement of the two sides manifests as tensile opening with no significant parallel component. Mechanisms that can lead to tensile failure include unloading (decompression), increased fluid pressure in the fracture, or shrinkage of the rock due to cooling or desiccation (i.e., reduction of water content). Tensile failure typically occurs within a few kilometres from the Earth's surface or through hydraulic fracturing, as the *in situ* stresses are always compressive at depths greater than a few tens of metres. For a detailed discussion of joints, see e.g. Pollard & Aydin (1988).

A brittle material under compressive stress, when subjected to sufficiently high confining stress, can fail through shearing (Szwedzicki, 2007; Jaeger et al., 2007).

This type of failure is often described by the Mohr-Coulomb criterion, a linearised approximation of the true Mohr failure envelope. According to this criterion, shear failure occurs when

$$|\sigma_s| > \tau = C + \sigma_{\text{eff}} \tan \phi_i \ , \tag{2.22}$$

where τ is the shear strength, C is the cohesion, and ϕ_i is the angle of internal friction. The resulting shear planes are oriented roughly at an angle of 30° from the maximum principal stress and run parallel to the intermediate principal stress. These features, commonly referred to as faults, experience a displacement that is predominantly parallel to their plane. The direction of shearing can be perpendicular to the fracture tip (in-plane shearing, Mode II) or parallel to the fracture tip (out-of-plane shearing, Mode III). Additionally, shearing can lead to secondary tensile fractures known as wing cracks (e.g. Horii & Nemat-Nasser, 1986; Baud et al., 1996).

According to Anderson's fault theory, one of the principal stresses is vertical, as the Earth's free surface is stress-free (Anderson, 1905, 1951). Consequently, the other two principal stresses are horizontal. Different fault regimes emerge depending on the magnitude of the vertical stress σ_v compared to the magnitude of the maximum and minimum horizontal principal stress, σ_H and σ_h, respectively. When $\sigma_v > \sigma_H$, the hanging wall moves downward relative to the footwall (i.e. normal faulting). Conversely, when $\sigma_h > \sigma_v$, the hanging wall moves upward relative to the footwall (i.e. reverse faulting). Strike-slip faulting of nearly vertical faults occurs when $\sigma_H > \sigma_v > \sigma_h$.

Compared to the shearing of an intact rock mass described in Eq. (2.22), the shearing of pre-existing fractures is cohesionless and thus occurs at lower shear stresses. A pre-existing fracture begins to slip when the shear stress σ_s acting on it exceeds the (static) frictional sliding strength $\tau_{\max}$ of the fracture plane, i.e.,

$$|\sigma_s| > \tau_{\max} \ . \tag{2.23}$$

This cohesionless frictional sliding strength can be modelled by the Coulomb friction law

$$\tau_{\max} = \begin{cases} \sigma_{\text{eff}} \tan \phi', & \sigma_{\text{eff}} > 0 \\ 0, & \text{otherwise} \ , \end{cases} \tag{2.24}$$

where σ_{eff} denotes the effective normal stress at the fracture, and ϕ' is the friction angle. Note that the frictional sliding strength is zero for negative effective normal stresses. As the fracture slips, the shear stress relaxes until the arrest criterium

$$|\sigma_s| \leq \tau_{\max} \tag{2.25}$$

is satisfied. In practice, the friction angle varies with shear displacement, and dynamic effects play a role.

2.2.2 Fracture parameters

Understanding fractures in geological formations involves examining various parameters that define their characteristics. Some of these are illustrated in Fig. 2.2 for idealised fractures in a 2D domain. This section discusses the most important fracture parameters for flow, transport and mechanics by building upon Singhal & Gupta (2010).

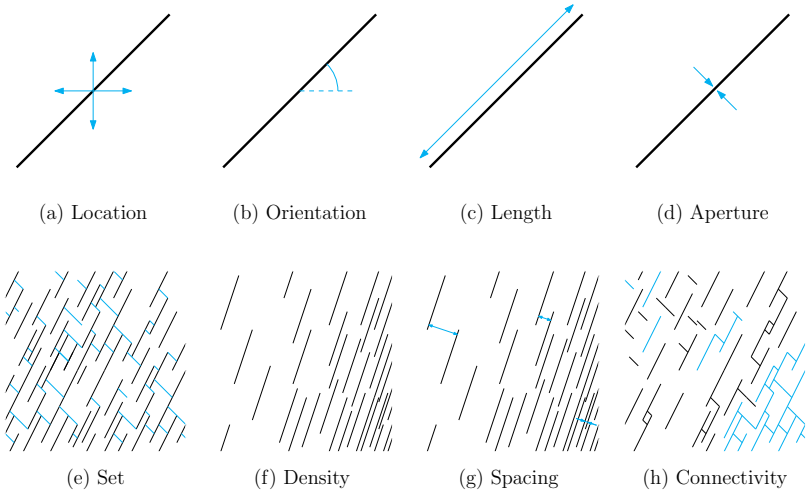

(a) Location (b) Orientation (c) Length (d) Aperture

(e) Set (f) Density (g) Spacing (h) Connectivity

Figure 2.2: Fracture parameters of idealised fracture lines in a 2D domain.

A single fracture is foremost determined by the extent of its surface characterised by location, orientation, size and shape. Furthermore, the fracture aperture describes the opening of the fracture, i.e., the distance between the two opposing fracture surfaces. This vital parameter for flow and transport in fractured porous media is discussed in more detail in the following section. In fracture mechanics, the friction angle of the fracture surface is essential. It depends on the rock material (described e.g. by the basic friction angle) and on the roughness of the fracture surface (described e.g. by the joint roughness coefficient). Different models exist for determining the friction angle; one is the empirical model of Barton and Bandis described in detail in Appendix A.

Fractures of similar orientation and formed under comparable conditions are grouped into a set. They tend to be of similar age and exhibit coherent orientation and length statistics. A rock mass can contain fractures from multiple sets. Preexisting ones often influence the formation of newer fractures. Newer fractures can, for example, terminate at existing fractures and thus show different length

statistics (Rawnsley et al., 1998). A fracture set is characterised by its spacing (i.e. the perpendicular distance between individual fractures) and the fracture density. Fracture density refers to the fracture surface area per unit rock volume in 3D (P32) or fracture length per unit area in 2D (P21). Those properties are intrinsically linked to the volumetric fracture count, which is the number of fractures per unit rock volume.

Fractures can form highly conductive flow paths. Those preferential flow paths rely on a network of interconnected open fractures, especially in low-permeable rocks. In contrast, open but isolated and interconnected but closed fractures typically contribute only little to the overall flow and transport behaviour. The degree of connectivity can be described with percolation theory (e.g. Adler et al., 2012). While the fractures can be responsible for most of the flow through a porous medium, the total volume of all fractures is typically small compared to the total pore volume of the rock mass. As a result, the matrix serves as the primary storage for fluids in most cases.

2.2.3 Fracture aperture

The aperture of fractures plays a significant role in governing fluid flow and transport within fractured porous media. While open fractures generally enhance the flow through a rock mass, those filled with minerals can create barriers. The aperture particularly depends on the fracture's orientation relative to the prevailing stress field. Studies have shown that critically stressed fractures, i.e. those with a high ratio of shear to normal stress, tend to be hydraulic conductive, whereas others are likely to be closed (Barton et al., 1995; Townend & Zoback, 2000). In this section, we discuss various mechanisms that can lead to the opening or closing of fractures and introduce the concept of equivalent aperture. Fracture apertures exist at various scales; in this work, we consider apertures larger than the average pore diameter in sandstone.

Mechanisms influencing fracture aperture

Ordinarily, opposing fracture surfaces are not exactly identical, which leaves a small gap under stress-free conditions (Fig. 2.3a). In the empirical joint constitutive model of Barton and Bandis (Appendix A), this gap is called the initial fracture aperture and is modelled with Eq. (A.2). It sets the baseline for responding to subsequent stress changes. Under compressive stress, the fracture aperture is reduced following Eq. (A.3) for normal closure.

When a fracture experiences shearing, the mismatch between the opposing fracture surfaces typically increases (Fig. 2.3b). Thus, shearing leads to an increase in fracture aperture, referred to as shear dilation. The dilation angle ϕ_d relates an increment in shear displacement $\mathrm{d}\delta_s$ to an increment in shear dilation $\mathrm{d}\delta_d$, i.e.,

$$\mathrm{d}\delta_d = \mathrm{d}\delta_s \tan(\phi_d) \ . \tag{2.26}$$

It is a complex function influenced by fracture and rock parameters and varies throughout the shearing process. Many joint constitutive models, including that of Barton and Bandis (Eq. (A.5)), consider a dilation angle that changes with shear displacement (Lei, 2022). Accordingly, to calculate the total shear dilation, δ_d, one must integrate the tangent of the dilation angle over the shear displacement, δ_s, as follows:

$$\delta_d = \int_0^{\delta_s} \tan\left(\phi_d\right) \mathrm{d}\delta_s \ . \tag{2.27}$$

Other models assume a constant dilation angle, which simplifies the calculation of shear dilation to

$$\delta_d = \delta_s \tan\left(\phi_d\right) \ . \tag{2.28}$$

While shearing under low compressive stresses typically increases the aperture (Vilarrasa et al., 2011), shearing under high compressive stress can crush and grind asperities and subsequently decrease the aperture (Karami & Stead, 2008; Asadi et al., 2012; Zhao et al., 2018). In addition, the fragments of the crushed and ground asperities can fill the remaining opening and effectively close the fracture.

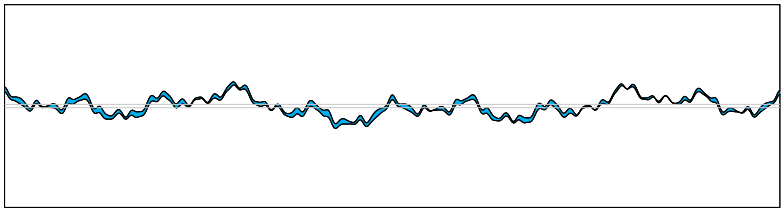

(a)

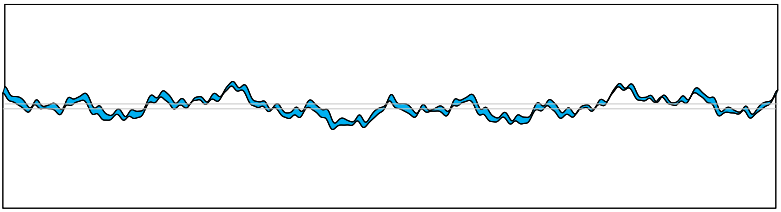

(b)

Figure 2.3: Small gap under stress-free conditions as the two opposing fracture surfaces are not exactly identical (a). Shear dilation describes the aperture increase through shearing (b). The grey lines indicate the arithmetic mean of the local apertures.

Tensile (i.e. negative compressive) stress represents another mechanism that can increase a fracture's aperture. In subsurface environments, where far-field stresses are typically compressive, tensile openings are most commonly created by shearing or hydraulic fracturing. Examples of the latter are wing cracks and dilational jogs formed by shearing of segmented or en echelon fractures (e.g. Segall & Pollard, 1980; Sibson, 1985; Horii & Nemat-Nasser, 1986; Baud et al., 1996). In order to ensure that fractures created by hydraulic fracturing stay open after the pressure is released, a proppant such as sand is injected.

Chemical processes can also play a significant role in altering fracture aperture (e.g. Elsworth & Yasuhara, 2010). For instance, rock dissolution, prominently occurring in karst formations, can increase fracture aperture. Conversely, mineralisation can narrow or completely seal a fracture. This process often results in the formation of mineral veins, which can act as barriers to fluid flow.

Given the mechanisms described above, fracture apertures can vary markedly from one fracture to another (Barton et al., 1995; Baghbanan & Jing, 2008; Barton & Quadros, 2015; Zhang et al., 2021b). Therefore, numerical models need to account for this variability. Relying on a single, uniform aperture value for all fractures, on the other hand, can lead to inaccurate representations of flow and transport behaviour in fractured porous media.

Equivalent aperture and fracture permeability

The aperture is rarely constant within a single fracture, but fluctuates considerably across the fracture's extent due to the roughness of the opposing fracture surfaces. Part of these fluctuations can be effectively modelled as a spatially correlated random field (Adler et al., 2012).

In many situations, resolving these local aperture fluctuations is impractical and dispensable. In this case, an equivalent aperture is employed in simulations. A common approach is using the arithmetic mean of the local aperture values, which is referred to as the mechanical or void aperture. The equations presented earlier in this section and Appendix A apply to this definition of aperture.

The hydraulic (or cubic law) aperture, on the other hand, is relevant for flow and transport simulations. This term describes the aperture of a hypothetical smooth-walled parallel plate channel that yields flow rates equivalent to those through the actual rough-walled fracture under the same pressure difference. Assuming a plane Poiseuille flow between the two smooth walls, the flow rate per unit width W is given by

$$\dot{Q}/W = -\frac{D^3}{12\mu}\nabla p \,, \tag{2.29}$$

where D is the distance of the two plates (i.e. the channel height). This relation is referred to as the cubic law; for a detailed derivation, see Adler et al. (2012). When modelling the fracture as a porous medium with aperture a_f and applying

Eq. (2.7), the flow rate per unit width can be expressed as

$$\dot{Q}/W = -a_f \frac{k_f}{\mu} \nabla p \, . \tag{2.30}$$

By comparing this equation with the Poiseuille flow formula Eq. (2.29), we obtain the fracture permeability

$$k_f = \frac{a_f^2}{12} \, . \tag{2.31}$$

Here, a_f refers to the hydraulic fracture aperture.

A comprehensive discussion on different equivalent apertures and their interrelationships can be found in Tsang (1992), Renshaw (1995) and Taylor et al. (1999). Although mechanical and hydraulic apertures generally differ in this work, we assume they are equivalent for simplicity.

2.3 Measuring subsurface fractures

While fractures influence the flow, transport and mechanics of a subsurface rock mass, detecting them and measuring their properties is challenging. Adapted from Liem et al. (2023b, Preprint), this section provides a brief overview of this topic.

Several established techniques exist that detect and characterise fractures in the vicinity of boreholes, such as image logging, core analysis or spinner logs (Genter et al., 1997; Prensky, 1999; Al-Dhafeeri & Nasr-El-Din, 2007; Ali et al., 2021). However, boreholes are typically sparse, and borehole imaging methods do not cover the space between them. On the other hand, measuring seismic anisotropy provides statistical or average information about fractures in a whole reservoir. However, only the fracture orientation, density, and, to some extent, length distribution can be deduced, while the apertures and exact geometry of fractures remain unknown (Liu & Martinez, 2012). Outcrops show concrete realisations of the fracture geometry, albeit only at the earth's surface. They serve as analogues from which statistical information about the fracture geometry in the subsurface reservoir can be inferred (Casini et al., 2016; Gutmanis et al., 2018). Geostatistical tools such as variograms and (co)kriging analyse and predict distributions of spatially correlated subsurface properties (Chilès & Delfiner, 2012).

Consequently, fracture parameters, particularly fracture aperture, are subject to high levels of uncertainty.

2.4 Modelling of fractured porous media

Fractured porous media pose many challenges for modelling. The size of fracture apertures is typically in the order of millimetres, while the domain of interest can extend over several kilometres. The wide range of scales involved makes a fully resolved equidimensional mesh impractical. Additionally, the frequency of

fractures typically increases with decreasing fracture length. While usually, only a handful of long fractures exist that potentially even extend throughout the whole reservoir, there are countless small fractures and micro-cracks present in the host rock. Resolving fractures at all length scales is impossible, so we typically upscale fractures below a certain length into the matrix properties. Various methods have been developed to discretise and model fractured porous media, some representing the fractures explicitly while others treat them only implicitly. This section briefly overviews some popular methods based on Berre et al. (2018). However, this overview is not exhaustive, and numerous methods exist that are not covered here.

2.4.1 Explicit fracture representation

When fractures are represented explicitly, their geometrical and topological information is partially preserved, leading to accurate but complex meshes. We can categorise different modelling approaches based on how they treat the matrix domain.

Discrete fracture matrix (DFM) models represent the matrix with a conforming mesh (e.g. Geiger et al., 2004; Karimi-Fard et al., 2004; Dietrich et al., 2005; Reichenberger et al., 2006; Matthäi et al., 2007; Paluszny et al., 2007; Hægland et al., 2009; Stefansson et al., 2021). DFM models require an unstructured mesh unless the fracture geometry is highly regular. Creating such a mesh is challenging, especially when fractures intersect at small angles or almost coincide. A large number of grid cells and grid cells with large aspect ratios can result, hampering the efficiency and accuracy of simulations. However, once the mesh has been generated, modelling of the relevant physics is relatively straightforward. Typically, DFM models treat the fractures as lower-dimensional features (mixed-dimensional models), but equidimensional approaches also exist.

On the other hand, embedded discrete fracture matrix (EDFM) models represent the matrix domain with a non-conforming mesh (Li & Lee, 2008; Hajibeygi et al., 2011; Moinfar et al., 2013). The fractures are modelled as lower-dimensional features embedded in the matrix. EDFM models enable simple, regular meshes, which are much easier to generate than the unstructured ones for DFM models. However, it is more challenging to model the relevant physics, particularly the interactions between fracture and matrix. Examples of EDFM are the extended finite element method (XFEM) (Huang et al., 2011; D'Angelo & Scotti, 2012; Schwenck et al., 2015) and the extended finite volume method (XFVM) (Deb & Jenny, 2017a,b; Conti et al., 2023, 2024). Flemisch et al. (2018) compare several DFM and EDFM methods in a benchmark study.

Finally, discrete fracture network (DFN) models ignore the matrix domain and only consider the fracture domain (e.g. Jing & Stephansson, 2007). DFN models are appropriate in, for example, densely-fractured low-permeability rocks.

2.4.2 Implicit fracture representation

Continuum models represent the fractures only implicitly, losing the geometrical and topological information of the fractures to a large extent. We distinguish between single- and multi-continuum models.

Single-continuum models aim to capture the influence of the fractures by adapting the matrix properties, in particular the matrix permeability. Various techniques exist for this upscaling process; Section 2.4.3 discusses one of them. Single-continuum models are relatively simple, and one can effortlessly reuse existing frameworks for non-fractured porous media. While they can accurately model steady-state single-phase flows, they are rarely appropriate for more complex transport calculations as they over-simplify the system.

Multi-continuum models treat fractures as one or several superimposed media on top of the matrix domain (Dietrich et al., 2005). These models consolidate the impact of the fractures within parameters such as permeability and porosity of the corresponding fracture continuum. All continua have their own conservation equations and constitutive laws, and source terms model the transfer between the different continua. The key challenge in multi-continuum modelling lies in accurately defining these source terms. Popular multi-continuum models include the dual-porosity (DP) model (Barenblatt et al., 1960; Warren & Root, 1963; Kazemi et al., 1976) and the dual-porosity, dual-permeability (DPDP) model (Blaskovich et al., 1983; Hill & Thomas, 1985; Uleberg & Kleppe, 1996).

2.4.3 Upscaling of permeability and porosity

As discussed above, the practical implementation of fracture models requires upscaling of all or at least the smallest fractures. Upscaling aims to find equivalent values of model parameters, particularly permeability and porosity, that combine the influence of fractures and matrix into a single medium. The equivalent permeability of a fractured porous medium thereby depends on the geometry of the fractures and the surrounding mechanical and hydraulical environment, in particular on fracture length and aperture distributions, surface roughness, number of intersections and dead ends in the fracture network, hydraulic gradient, boundary stress, anisotropy and scale. Liu et al. (2016) review the influence of those parameters on the equivalent permeability and discuss corresponding upscaling techniques. A popular choice for well-interconnected fracture networks is the upscaling method presented by Oda (1985).

In Chapters 3 and 5 of this work, we consider fractured porous media with relatively few fractures. Notwithstanding, fully resolving the fractures with a Cartesian grid is too expensive due to the huge number of required grid cells. Instead, we use a coarser grid whose grid cell heights are several magnitudes larger than the fracture aperture but small enough that no more than two fractures intersect with a single grid cell. We can then calculate the upscaled permeability

from the isotropic fracture and matrix permeabilities using the analytical equations from Kasap & Lake (1990). The resulting upscaled permeability is typically anisotropic. Those equations assume straight streamlines in all homogeneous regions within a grid cell. When this is not the case, we obtain only approximate values; however, the errors are expected to be negligible for a reasonably fine grid. In the following, we explain this upscaling process in more detail.

For a single fracture oriented in x-direction and passing through a two-dimensional grid cell with dimensions $h_x \times h_y$, the upscaled permeability tensor and its components are

$$\widetilde{\mathbf{K}} = \begin{bmatrix} \tilde{k}_{xx} & \tilde{k}_{xy} \\ \tilde{k}_{xy} & \tilde{k}_{yy} \end{bmatrix} , \tag{2.32}$$

$$\tilde{k}_{xx} = \frac{h_y - a_f}{h_y} k_m + \frac{a_f}{h_y} k_f , \tag{2.33}$$

$$\frac{1}{\tilde{k}_{yy}} = \frac{h_y - a_f}{h_y} \frac{1}{k_m} + \frac{a_f}{h_y} \frac{1}{k_f} \quad \text{and} \tag{2.34}$$

$$\tilde{k}_{xy} = 0 . \tag{2.35}$$

When a grid cell contains more than one fracture or a fracture ends in the interior of a grid cell, we divide this particular grid cell into axillary regions and calculate their upscaled permeability values using Eqs. (2.32) to (2.35) (Fig. 2.4). Subsequently, we obtain the upscaled permeability of the entire grid cell from the values of the regions using the same equations. This procedure is only approximative as we obtain lower or upper limits of the equivalent permeability depending on the choice of the axillary regions.

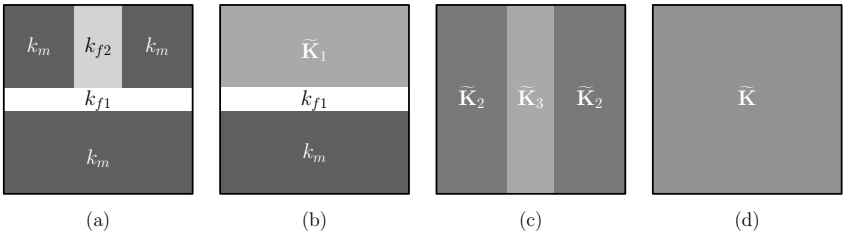

Figure 2.4: Upscaling process of Kasap & Lake (1990) for grid cells containing two fractures (a), where the choice of auxiliary regions, i.e., either (b) or (c), influences the resulting upscaled permeability $\widetilde{\mathbf{K}}$ of the cell (d).

Further, we obtain the upscaled porosity $\widetilde{\phi}$ through volume averaging, i.e.,

$$\widetilde{\phi} = \frac{V - V_f}{V}\phi_m + \frac{V_f}{V}\phi_f \ . \tag{2.36}$$

Consequently, the upscaled porosity is a function of the ratio of fracture volume V_f to grid cell volume V. Fig. 2.5 shows the upscaled porosity and permeability fields obtained from Eqs. (2.32) to (2.36) for a simple geometry consisting of two fractures and a Cartesian grid.

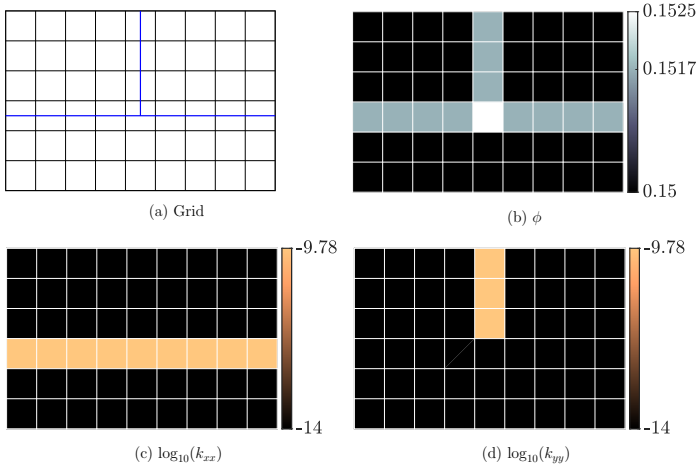

(a) Grid (b) ϕ (c) $\log_{10}(k_{xx})$ (d) $\log_{10}(k_{yy})$

Figure 2.5: Simple fracture geometry with two fractures ($a_f = 1\,\text{mm}$, $\phi_f = 1$) and Cartesian grid ($h_x = h_y = 0.5\,\text{m}$) (a), the corresponding upscaled porosity (b) and logarithm of the upscaled horizontal and vertical permeability components (c,d). Note that the off-diagonal components of the upscaled permeability tensor are assumed to be zero. Figure adapted from Liem et al. (2022a).

The upscaling approach presented here is accurate for steady-state single-phase flow. The upscaled permeability and porosity fields generate flow patterns that closely resemble those derived from the original fully resolved permeability and porosity fields. However, the results might deviate for more complex problems, such as tracer breakthrough or multiphase flow. Notably, the coarse upscaled grid assumes perfect mixing within the grid cells, introducing numerical diffusion. Therefore, a mixed-dimensional DFM or EDFM approach might be more appropriate to address such transport scenarios.

3 Adaptive Conservative Time Integration for Transport in Fractured Porous Media

This chapter is adapted from the article "Adaptive conservative time integration for transport in fractured porous media" (Liem et al., 2022a).

3.1 Introduction

Time-dependent hyperbolic partial differential equations (PDEs) play an essential role in many areas of science and engineering, including fluid dynamics, acoustics, and the propagation of waves in elastic media. In subsurface contexts, they are instrumental in modelling transport phenomena (see Section 2.1.2) and seismic activity.

When solving time-dependent hyperbolic PDEs with a finite volume method (FVM), time is traditionally advanced with a global time step, i.e., in spatially uniform time intervals. The time integration technique is either explicit if the unknown variables of the current time step only depend on quantities already calculated previously, or implicit if the unknown variables also depend on quantities still to be calculated at the current time step. For both schemes, the size of the integration time step is bounded. The Courant-Friedrichs-Lewy (CFL) criterion restricts the integration time step for explicit schemes to guarantee stability (Courant et al., 1928). Implicit schemes generally allow larger integration time steps. There even exist unconditionally stable implicit schemes for PDEs with S-shaped flux functions (Jenny et al., 2009); however, the integration time step is limited by the desired accuracy.

When grid cell size or wave speed (e.g. advection speed of a tracer) vary significantly throughout the domain, the optimal time step of each grid cell can vary over several orders of magnitudes. As a result, a small number of grid cells dictate the global time step, while many grid cells are advanced in time with an integration step much smaller than necessary. One example of such a system is flow through fractured porous media, where the permeability and subsequently also the flow velocity can be several orders of magnitude higher in the fractures than in the rock matrix (Matthäi & Belayneh, 2004; Geiger et al., 2004). Transport of tracers, contaminants, and other dissolved chemicals in water-saturated fractured porous media is often anomalous (Edery et al., 2016). Good spatial resolution in the vicinity of highly conductive fractures is required to accurately capture flow and transport in these areas and calculate detailed breakthrough curves. With

global time stepping it is extremely costly to solve transport in such systems, especially when considering a reasonable domain size. Therefore, more efficient time integration schemes are needed.

Various local time stepping methods have been developed to improve the efficiency of time integration and to reduce the computational cost for such systems and applications. Those methods allow individual time steps for each grid cell under the constraint of a local CFL criterion.

Osher & Sanders (1983) presented one of the first local time stepping methods. Their method relies on a conservative predictor-corrector scheme, and they proved convergence for one-dimensional non-linear scalar conservation laws. Dawson & Kirby (2001) extended the method to a higher-order time stepping scheme. Berger & Oliger (1984) introduced a conservative interface equation to pass information between coarse and refined grids that are overlain in regions where a more accurate solution is required. Their method automatically takes smaller time steps in those refined regions and integrates the grids independently, allowing higher-order time integration. Zhang et al. (1994) applies local time stepping only to the flux calculation. Dawson (1995) introduced a local time stepping method that enforces flux continuity across the cell interfaces.

Pervaiz & Baron (1989), Kleb et al. (1992) and Jenny (2020) use local time steps which relate to each other by factors of powers of two. However, the time variable that determines the sequence in which the cells are integrated is different. Kleb et al. (1992) integrate the cells with the lowest current time first, while Pervaiz & Baron (1989) advance cells according to their current time plus half of their local time step. Jenny (2020) updates those cells first whose next time (i.e. their current time plus one local time step) is lowest, with the additional constraint that cells with a larger time step are never ahead of ones with a smaller time step. Similar to Dawson (1995), this method accumulates the flux through the interface between two cells with different local time steps when it is calculated for the cell with the smaller time step. The accumulated flux is used later for updating the cell with the larger time step; therefore, this method is conservative by design. Kulka & Jenny (2022) extended the method to unsteady compressible flow.

Related approaches include discrete event simulation (DES), which is a totally asynchronous time stepping method (Nutaro et al., 2003; Shao et al., 2019), and multirate methods which integrate each component of the system using a different time step (Constantinescu & Sandu, 2007; Delpopolo Carciopolo et al., 2019, 2020).

This work extends the method of Jenny (2020), called adaptive conservative time integration (ACTI), to tracer transport in fractured porous media and applies it to two-dimensional models where we compare the accuracy and computational cost of ACTI with those of global time stepping. Furthermore, we empirically investigate the stability of several flux discretisation schemes when they are combined with ACTI.

This chapter of the thesis is organised as follows: Section 3.2 introduces our solver for hyperbolic scalar transport equations including different schemes for numerical flux discretisation and discusses the adaptive time stepping method. In Section 3.3, we present the results of the two-dimensional test cases. We demonstrate a considerable reduction of computational cost when using ACTI as compared to global time stepping.

3.2 Method

In this section, we first describe our transport solver and then introduce the adaptive conservative time integration (ACTI) scheme.

3.2.1 Transport

We consider the hyperbolic scalar transport equation for porous media as presented in Section 2.1.2,

$$\phi \frac{\partial c}{\partial t} + \mathbf{q} \cdot \nabla c - \dot{q}_{\text{Source}} c_{\text{Source}} = 0 \,, \tag{3.1}$$

where c denotes the concentration of the scalar tracer, $\mathbf{q}$ the volumetric flux density (also called Darcy velocity) and ϕ the porosity. Here, the advection speed is approximated as the pore velocity $\mathbf{a} = \mathbf{q}/\phi$. Note that Eq. (3.1) is not in its conservative form, and we neglect diffusion. We discretise Eq. (3.1) with a cell-centred FVM using a Cartesian grid, and obtain concentration values at the time $t^{n+1} = t^n + \Delta t$ for a two dimensional case with

$$c_{i,j}^{n+1} = c_{i,j}^{n} + \frac{\Delta t}{\phi_{i,j}} \left(\frac{F_{i-\frac{1}{2},j}^{n\to n+1} - F_{i+\frac{1}{2},j}^{n\to n+1}}{h_{x_{i,j}}} + \frac{F_{i,j-\frac{1}{2}}^{n\to n+1} - F_{i,j+\frac{1}{2}}^{n\to n+1}}{h_{y_{i,j}}} + \dot{q}_{\text{Source}} c_{\text{Source}} \right) \,, \tag{3.2}$$

where the subscripts i and j denote the cell indices in the first and second direction respectively and the superscript n the time index. h_x and h_y are the size of the grid cell in x and y direction, respectively. The fluxes $F^{n\to n+1}$ can be discretised with a wide variety of numerical schemes. In this work, we explore four different explicit schemes, one of which is of first spatial order and the other three of higher-order. In the following, we focus on the flux through the right interface $\Omega_{i,j}$, that is,

$$F_{i+\frac{1}{2},j}^{n\to n+1} = q_{i+\frac{1}{2},j} c_{i+\frac{1}{2},j}^{n\to n+1} \,; \tag{3.3}$$

all other fluxes are obtained analogously. The concentration at the right interface is approximated as

$$c^{n\to n+1}_{i+\frac{1}{2},j} = \begin{cases} c^n_{i,j} \quad + \beta_1 \sigma 1_{i,j} \dfrac{h_{x_{i,j}}}{2} \qquad - \beta_2 \sigma 1_{i,j} \dfrac{q_{i+\frac{1}{2},j}}{\phi_{i+\frac{1}{2},j}} \dfrac{\Delta t}{2} \quad - \beta_3 \sigma 2_{i,j} \dfrac{q_{2i,j}}{\phi_{i,j}} \dfrac{\Delta t}{2} \\ \qquad\qquad\qquad\qquad\qquad\qquad\qquad\qquad\qquad\qquad\qquad\qquad \text{if } q_{i+\frac{1}{2},j} > 0 \\ c^n_{i+1,j} - \beta_1 \sigma 1_{i+1,j} \dfrac{h_{x_{i+1,j}}}{2} - \beta_2 \sigma 1_{i+1,j} \dfrac{q_{i+\frac{1}{2},j}}{\phi_{i+\frac{1}{2},j}} \dfrac{\Delta t}{2} - \beta_3 \sigma 2_{i+1,j} \dfrac{q_{2i+1,j}}{\phi_{i+1,j}} \dfrac{\Delta t}{2} \\ \qquad\qquad\qquad\qquad\qquad\qquad\qquad\qquad\qquad\qquad\qquad\qquad \text{otherwise,} \end{cases} \tag{3.4}$$

where the parameters β_1, β_2 and β_3 determine the flux scheme. For $\beta_1 = \beta_2 = \beta_3 = 0$, Eq. (3.4) reduces to the first-order explicit upwind scheme. $\beta_1 = 1$ gives a higher-order scheme, where $\beta_2 = \beta_3 = 0$ corresponds to a MUSCL upwind scheme without slope advection, $\beta_2 = 1$ and $\beta_3 = 0$ to a MUSCL with slope advection (LeVeque, 2002) and $\beta_2 = \beta_3 = 1$ to a MUSCL scheme with advection of inclined reconstruction (MUSCL-AIR) (Jenny, 2020). In Section 3.3.1, we show the superiority of MUSCL-AIR over the other two MUSCL schemes. Therefore, we use MUSCL-AIR along with the 1$^{\text{st}}$ order scheme for the most part of this work.

In Eq. (3.4), σ_1 and σ_2 are the slope components normal and parallel to the interface, respectively. For the former, we use the Koren limiter (Koren, 1993) which is defined as

$$\sigma_1 = \sigma_1(s_1, s_2) = s_2 \max\left(\min\left(\min\left(\frac{s_2 + 2s_1}{3s_2}, 2\right), \frac{2s_1}{s_2}\right), 0\right) , \tag{3.5}$$

where for $q_{i+\frac{1}{2},j} > 0$

$$s1_{i,j} = 2\frac{c_{i+1,j} - c_{i,j}}{h_{x_{i+1,j}} + h_{x_{i,j}}} \quad \text{and} \quad s2_{i,j} = 2\frac{c_{i,j} - c_{i-1,j}}{h_{x_{i,j}} + h_{x_{i-1,j}}} . \tag{3.6}$$

The slope component parallel to the interface for $q_{i+\frac{1}{2},j} > 0$ is calculated as

$$\sigma 2_{i,j} = \begin{cases} 2\frac{c_{i,j} - c_{i,j-1}}{h_{y_{i,j}} + h_{y_{i,j-1}}} & \text{if } q_{2i,j} = \frac{1}{2}\left(q_{i,j-\frac{1}{2}} + q_{i,j+\frac{1}{2}}\right) > 0 \\ 2\frac{c_{i,j+1} - c_{i,j}}{h_{y_{i,j+1}} + h_{y_{i,j}}} & \text{otherwise.} \end{cases} \tag{3.7}$$

All other slopes are obtained analogously.

For explicit schemes the size of the integration time step Δt is limited by the CFL criterion (Courant et al., 1928). In this work, we use the formula for Donor-Cell Upwind

$$\left|\frac{a_1 \Delta t}{h_1}\right| + \left|\frac{a_2 \Delta t}{h_2}\right| \leq CFL_{\max} \tag{3.8}$$

proposed by LeVeque (2002).

3.2.2 Adaptive Conservative Time Integration (ACTI)

The adaptive conservative time integration (ACTI) algorithm proposed by Jenny (2020) uses local time steps of size

$$\Delta t_I = \frac{\Delta t_{\max}}{2^{L_I}} \ , \tag{3.9}$$

equal to the maximum desired time step size divided by powers of two. Grid cells are synchronised after each maximum step. The integer variable $L_I \geq 0$ denotes the time refinement level of a particular grid cell, where a high level corresponds to a small local time step. For every grid cell I we choose the lowest possible level L_I that still satisfies the local CFL criterion, i.e.,

$$\Delta t_I = \frac{\Delta t_{\max}}{2^{L_I}} \leq \Delta t_I^{CFL} = CFL_{\max} \left(\left| \frac{a_{1_I}}{h_{1_I}} \right| + \left| \frac{a_{2_I}}{h_{2_I}} \right| \right)^{-1} < \frac{\Delta t_{\max}}{2^{L_I - 1}} \ . \tag{3.10}$$

The sequence in which the grid cells are advanced in time is such that the time difference between cells is minimal and a cell with a larger local time step is never ahead of a cell with a smaller time step. When a cell I is advanced further in time than its neighbour J (which implies $\Delta t_I \leq \Delta t_J$), the corresponding flux between them is stored and recalled later when the neighbouring cell catches up, that is,

$$\Delta t_J F_{I \to J}^{t \to t + \Delta t_J} = -\Delta t_I \sum_{m=1}^{\Delta t_J / \Delta t_I} F_{J \to I}^{t + (m-1)\Delta t_I \to t + m \Delta t_I} \ . \tag{3.11}$$

Therefore, strict conservation at the global time resolution is guaranteed.

When we calculate the flux with a MUSCL scheme, we need to account for the potential time difference between cells where the characteristic line originates from the adjacent cell. We therefore replace $\frac{\Delta t}{2}$ in the second line of Eq. (3.4) with $\frac{\Delta t_{i,j}}{2} + t_{i,j} - t_{i+1,j}$. As this does not deal with potential time differences between cells that are used for the calculation of the slope components σ_1 and σ_2 (Fig. 3.1), the slopes might be estimated imprecisely near the interface between different levels. This might lead to a loss of accuracy in the higher-order schemes. This issue does not occur with the 1$^{\text{st}}$ order scheme, since there only the concentration value from the upwind cell determines the concentration at the cell interface. It will be shown that related inaccuracies are only local and do not affect overall simulation results.

In this work, we only consider 2D test cases. Since dimensional splitting is used in the discretisation of Eq. (3.1) it is straight forward to extend the framework to 3D Cartesian grids. In essence, an additional term for the third dimension would appear in the CFL criterion (Eq. (3.8)) and a second slope component parallel to the interface is required in MUSCL-AIR. A pseudo code representation of the ACTI algorithm is presented in Appendix B. The ACTI scheme as presented in Algorithm 5 does not make any assumptions on the dimensionality of the problem.

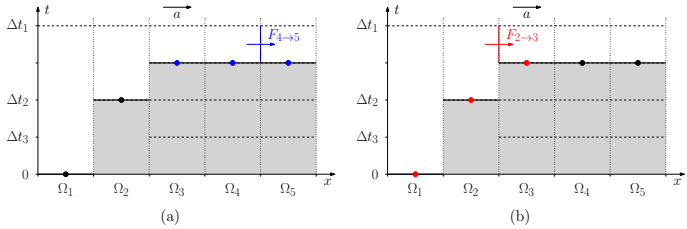

Figure 3.1: 1D domain with 5 grid cells where $\Delta t_1 = 2\Delta t_2 = 4\Delta t_{3,4,5}$. Cells used for flux calculation with a MUSCL scheme can be on the same time level (a) or on different time levels (b).

3.2.3 Test cases

In this study, we only consider single-phase flow in a horizontal layer of a fractured porous medium where we can neglect the influence of gravity. We obtain the steady-state volumetric flux density $\mathbf{q}$ from Darcy's law where we assume that the fluid and the porous material are incompressible (see Section 2.1.1). We discretise the elliptic pressure equation (Eq. (2.9)) with the FVM and use a direct solver. We then inject a tracer which follows the flow perfectly and does not alter the pressure field. We compare the concentration fields obtained with ACTI to the ones obtained from global time stepping.

We study three test cases, one without any fractures, one with a synthetic fracture network and one with a single fracture and local grid refinement (Table 3.1). All fractures are straight, grid aligned, and embedded in a porous matrix with constant and isotropic permeability k_m and porosity ϕ_m. For the latter two cases, we assume that the hydraulic aperture a_f is constant over the length of a fracture and we calculate fracture permeability from plane Poiseuille flow between parallel plates (Eq. (2.31)). In all test cases, we use volume flow boundary conditions at the inlet and pressure boundary conditions at the outlets. Initially, the concentration field is zero everywhere. At $t = 0$ we start injecting a tracer with concentration $c = 1$ through the inlet. Table 3.2 lists the parameter values used in all simulations of this study.

	Test Case	Number of Fractures	Local Grid Refinement
1	Uniform Matrix	0	No
2	Fracture Network	22	No
3	Single Fracture	1	Yes

Table 3.1: Test cases used in this study.

Fluid viscosity	$\mu = 1 \times 10^{-3}\,\mathrm{Pa\,s}$
Matrix permeability	$k_m = 1 \times 10^{-14}\,\mathrm{m}^2$
Matrix porosity	$\phi_m = 0.15$
Fracture aperture	$a_f = 1 \times 10^{-3}\,\mathrm{m}$
Fracture permeability	$k_f = a_f^2/12 = 8.333 \times 10^{-8}\,\mathrm{m}^2$
Fracture porosity	$\phi_f = 1.0$
Pressure at outlets	$p_{\mathrm{out}} = 1\,\mathrm{Pa}$

Table 3.2: General simulation parameters.

3.3 Results

3.3.1 Test case 1: uniform matrix (without any fractures)

First, we study the stability of the four flux schemes presented in Section 3.2.1 for a relatively small test case with uniform permeability and porosity. In this test case, the fluid enters the domain through the left boundary with $\dot{q}_{\mathrm{left}} = 1 \times 10^{-5}\,\mathrm{m/s}$ and leaves the domain at the top-right corner through a sink of size $0.1 \times 0.1\,\mathrm{m}^2$ (Fig. 3.2). Tracer is injected at three boundary segments of length 0.1 m on the left boundary and tracked over time. The transport is calculated for three different CFL values, $CFL_{\max} \in \{0.3, 0.5, 0.9\}$.

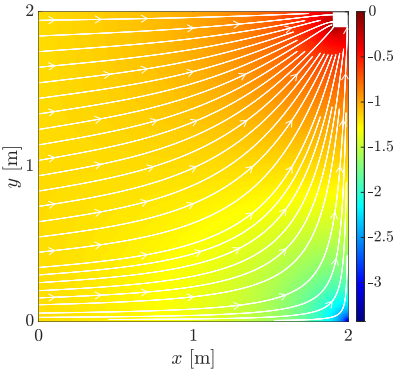

Figure 3.2: Logarithm of the magnitude of the normalised steady-state volumetric flux density, $\log_{10}(|\mathbf{q}|/|\mathbf{q}_{max}|)$. The flow accelerates towards the sink in the top-right corner. Flow paths are illustrated by streamlines.

For the 1st order scheme, the concentration fields calculated with ACTI agree very well with the ones obtained by global time stepping, see Fig. 3.3. Concentration fields are shown only for $CFL_{\max} = 0.9$, as the results are very similar for

all $CFL_{\max}$ values. As expected, the concentration front gets much sharper with the MUSCL schemes than with the 1st order scheme (Fig. 3.4). For global time stepping all three MUSCL schemes produce very similar results independent of the choice of $CFL_{\max}$. For ACTI, on the other hand, spurious oscillations arise in the concentration fields if MUSCL without slope advection is employed. Those oscillations are less pronounced if MUSCL with slope advection is used, and they generally grow with increasing $CFL_{\max}$. Yet, MUSCL-AIR with ACTI produces stable results that are practically identical to the ones obtained with global time stepping for all three $CFL_{\max}$ values.

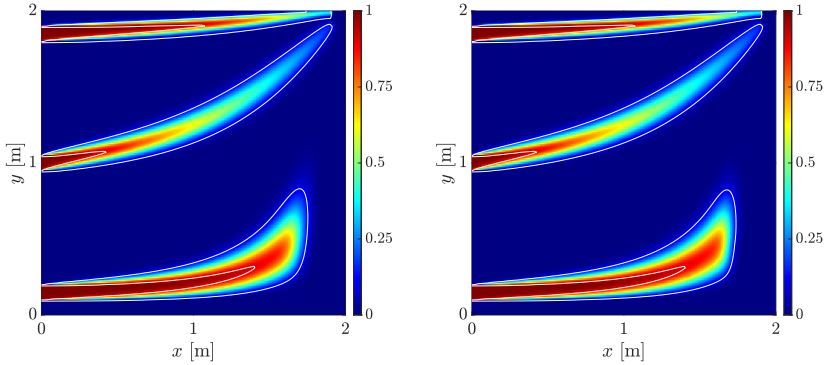

(a) Without ACTI (b) With ACTI

Figure 3.3: Concentration field after 22 h for global time stepping (a) and ACTI (b) for the 1st order scheme and $CFL_{\max} = 0.9$. The contour lines mark concentration values of 0.1 and 0.9.

As expected, global time stepping is stable for all four flux schemes because local CFL is tiny in a large portion of the domain (Fig. 3.5a). Only the cells near the point sink have a local CFL number close to $CFL_{\max}$. Therefore, global time stepping provides a certain margin for error in the time discretisation scheme. With ACTI, on the other hand, all cells have a local CFL number higher than half of $CFL_{\max}$ (Fig. 3.5b). Hence ACTI is less forgiving than global time stepping, and we need to pay special attention to the discretisation scheme.

With this test case, we demonstrate that the 1st order scheme is suitable for combination with ACTI. Of the three higher-order flux reconstruction schemes, only MUSCL-AIR performs well in combination with ACTI. MUSCL without and with slope advection, on the other hand, become unstable when combined with ACTI and $CFL_{\max}$ close to one. We presume that the instabilities seen for MUSCL without slope advection arise because it estimates the concentration values at the cell interfaces inaccurately. For a piecewise linear reconstruction,

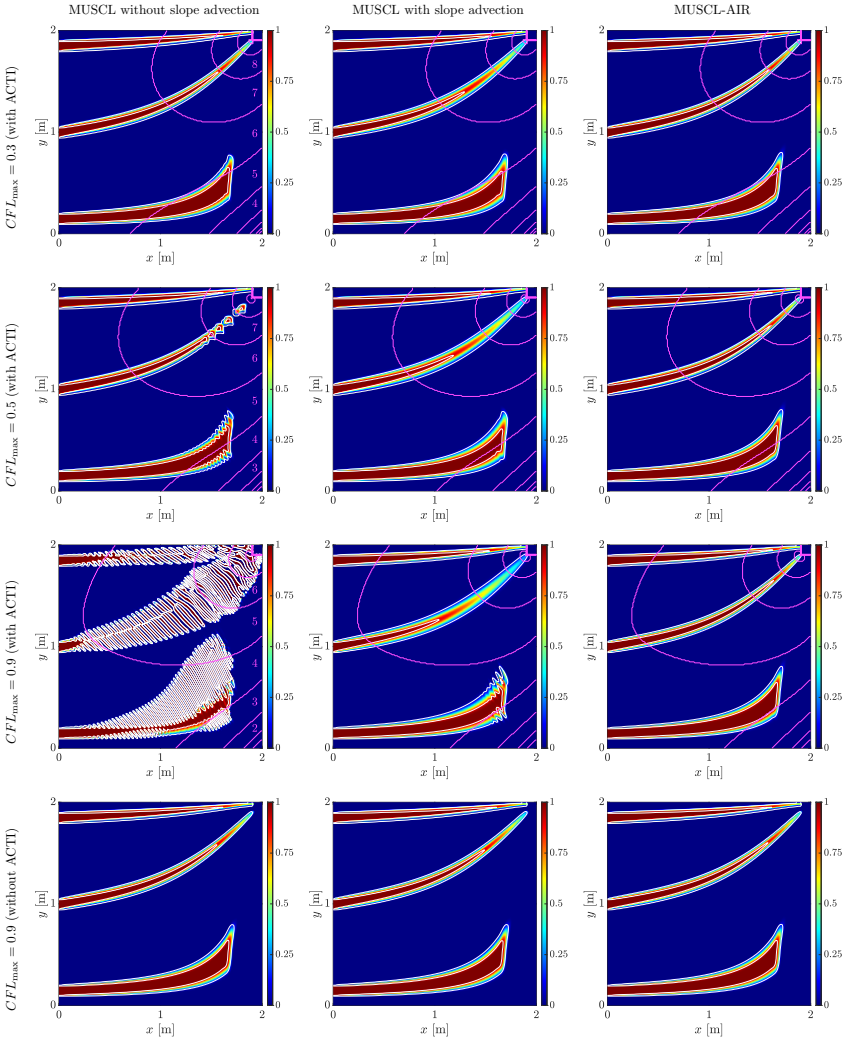

Figure 3.4: Concentration field after 22 h for three different MUSCL schemes. The first three rows show the results for ACTI for three choices of $CFL_{\max}$. The last row shows the results for global time stepping and $CFL_{\max} = 0.9$ (results with $CFL_{\max} = 0.3$ and 0.5 look almost identical). The white contour lines mark concentration values of 0.1 and 0.9. The pink contour lines depict the boundaries of the level L_I of ACTI.

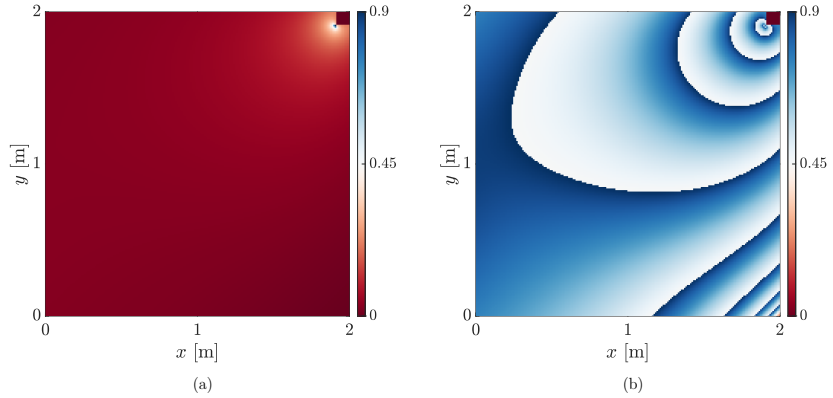

Figure 3.5: Local CFL numbers without (a) and with ACTI (b) for $CFL_{\max} = 0.9$. The plots for $CFL_{\max} = 0.3$ and 0.5 are qualitatively similar. Note that the discontinuities in the local CFL number in the case with ACTI stem from level jumps where the local time step is modified by a factor of two to ensure that the local CFL number is always greater than $CFL_{\max}/2$ but less than or equal to $CFL_{\max}$.

the exact solution of the interface value averaged over a time step is equal to the interface value at half of the time step (see reconstruct–evolve–average (REA) algorithm in e.g. LeVeque (2002)). However, MUSCL without slope advection uses the value at the beginning of the time step. MUSCL with slope advection estimates the concentration values at the cell interfaces correctly, but it does not account for diagonal flow. Consequently, the scheme is stable in regions where the flow is approximately parallel to the grid lines, but unstable in regions where the flow is not aligned. It is possible to stabilise these schemes at a lower $CFL_{\max}$ or by using a more diffusive limiter (see Appendix C for an example with the minmod limiter).

Some of the instabilities shown in Fig. 3.4 coincide with contour lines of the levels. However, level jumps are unlikely to be a dominant factor causing these instabilities because they remain at the same location when the contour lines are shifted by increasing or decreasing $CFL_{\max}$.

In the remaining part of this analysis we use only the 1^{st} order scheme and MUSCL-AIR and set $CFL_{\max} = 0.5$. This value is chosen empirically because a rigorous stability analysis for adaptive time stepping in two-dimensional models with variable porosity and/or grid spacing is beyond the scope of this work.

3.3.2 Test case 2: fracture network

Our second test case is a synthetic two-dimensional fracture network (Fig. 3.6a) consisting of 9 horizontal and 13 vertical fractures with a hydraulic aperture of 1 mm. This fracture network which was also used in a previous publication (Liem & Jenny, 2020) is chosen purely for demonstration purposes and represents a simplified model of large-scale fractures. We discretised the domain with a equidistant Cartesian grid, where the grid spacing in horizontal and vertical directions is 500 times larger than the hydraulic aperture of the fractures (Fig. 3.6b). The effect of the fractures is accounted for by upscaling. For grid cells which intersect with fractures we calculate upscaled permeability values using the analytical equations derived by Kasap & Lake (1990) and upscaled porosity values by volume averaging (Fig. 3.6c–e). This upscaling process is described in detail in Section 2.4.3 and in Liem & Jenny (2020). Table 3.3 lists the resulting upscaled values alongside other parameter values applied to the fracture model. In this test case, we use a point source at the lower left corner and sinks at all other corners. The source and sinks have a size of $2.5 \times 2.5\,\mathrm{m}^2$ and consist of 25 grid cells each.

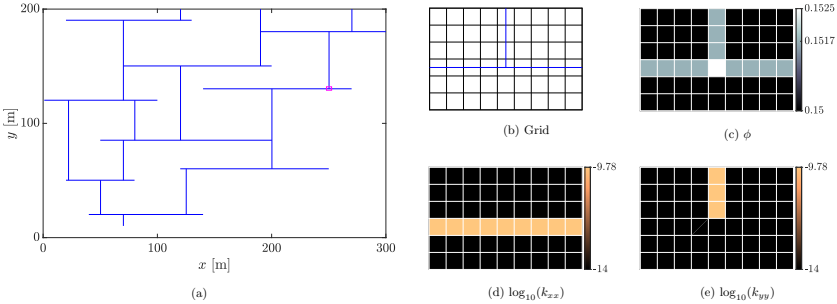

Figure 3.6: Geometry of fracture network (a), zoom-in on a fracture intersection (b) marked by the pink rectangle in (a), the corresponding upscaled porosity (c) and logarithm of the upscaled horizontal and vertical permeability components (d,e). Note that the off-diagonal components of the upscaled permeability tensor are assumed to be zero.

The resulting flow field is visualised in Fig. 3.7a as the logarithm of the magnitude of the normalised steady-state volumetric flux density, $\log_{10}(|\mathbf{q}|/|\mathbf{q}_{max}|)$, along with streamlines. In the following, we use the term velocity instead of the volumetric flux density. As expected, the highest velocities occur within the fractures and near the source and sinks. We observe several stagnation points in the matrix which lie either next to fractures or at the domain boundary. Fig. 3.7b shows the corresponding histogram. Most cells have a velocity which is around three orders of magnitude smaller than the maximum velocity and only a few cells

Size of domain	$300 \times 200 \times 1\,\mathrm{m}^3$
Number of grid cells	$600 \times 400 \times 1 = 240000$
Size of grid cells	$0.5 \times 0.5 \times 1\,\mathrm{m}^3$
Maximal time step for ACTI	$\Delta t_{\max} = 10\,\mathrm{d}$
CFL criterion	$CFL_{\max} = 0.5$
Flow rate through inlet	$\dot{Q}_{\mathrm{in}} = 2 \times 10^{-4}\,\mathrm{m}^3/\mathrm{s}$
Upscaled values for cells which contain a fracture	
Permeability in direction of fracture	$\tilde{k}_{\parallel} = 1.667 \times 10^{-10}\,\mathrm{m}^2$
Permeability perpendicular to fracture	$\tilde{k}_{\perp} = 1.002 \times 10^{-14}\,\mathrm{m}^2$
Porosity	$\tilde{\phi} = 0.1517$

Table 3.3: Simulation parameters of fracture network.

experience a high velocity. We expect that ACTI gives considerable speed benefits in a setup with such a velocity distribution.

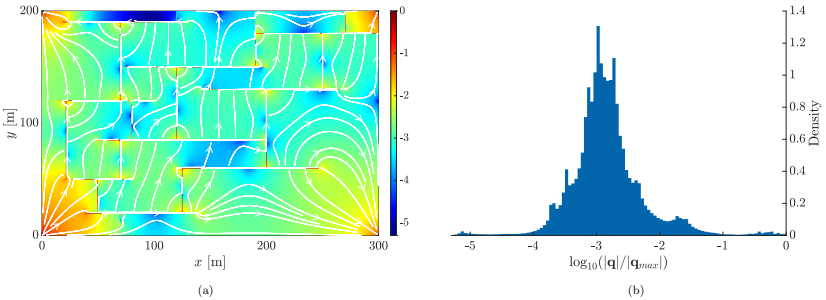

Figure 3.7: Logarithm of the magnitude of the normalised steady-state volumetric flux density, $\log_{10}(|\mathbf{q}|/|\mathbf{q}_{max}|)$, together with some streamlines (a) and the corresponding histogram (b).

ACTI partitions the grid cells into 13 levels ($0 \leq L_I \leq 12$) (Fig. 3.8a), which means that the smallest time step is $\Delta t_{\max}/2^{12} = 3.52\,\mathrm{min}$. If we use global time integration, the global time step obtained from the CFL criterion is 4.04 min. Note that this value is slightly larger than the minimum local time step in the case with ACTI, since there the local time steps are restricted to the maximal time step divided by powers of two. With ACTI, most grid cells have a local CFL number between 0.25 and 0.5 (Fig. 3.8b). Grid cells with a local CFL number below 0.25 are coloured in red and could be integrated with double the maximal time step or even more. However, we would not gain much because there are only

a few of those cells. The local CFL number for global time stepping is tiny for most of the domain (Fig. 3.8c).

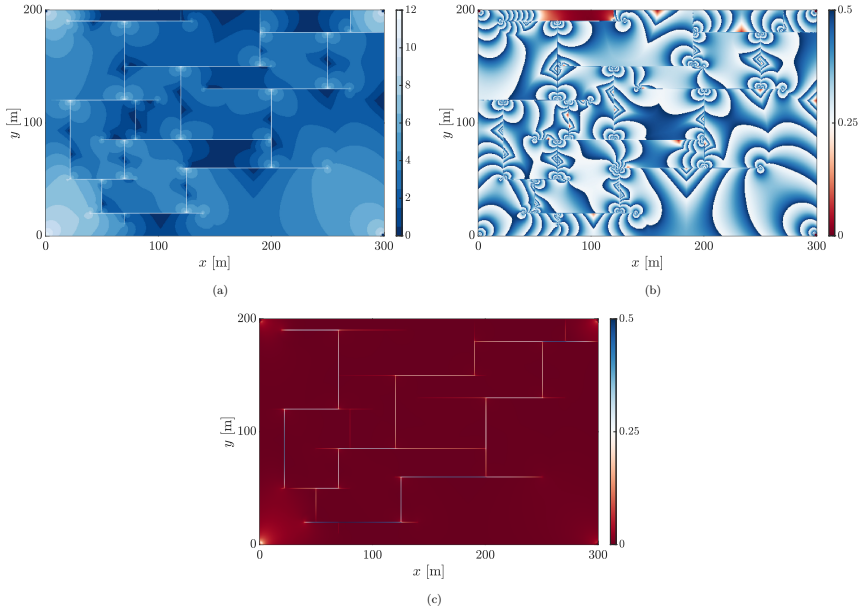

Figure 3.8: Levels (a) and local CFL numbers (b) with ACTI as well as local CFL numbers for global time stepping (c).

The resulting concentration fields calculated with ACTI and with global time stepping agree very well (Fig. 3.9). Most importantly, the concentration front is exact at the same location. For the 1st order scheme, we even obtain slightly sharper concentration fronts with ACTI than with global time stepping since higher local CFL numbers are beneficial for explicit schemes (note that they are limited to 0.5 in this test case). With MUSCL-AIR, there are a few locations where the concentration field differs. All of them lie in regions where the fluid flow crosses a fracture. MUSCL-AIR shows more pronounced numerical errors in these specific areas, if the local CFL number is large. However, these differences are only local and do not grow over time. For both flux schemes ACTI and global time stepping produce almost identical arrival curves at the three sinks. Fig. 3.10 shows the arrival curve at the sink in the bottom-right corner. The largest differences occur for the 1st order scheme and are due to the sharper concentration front with ACTI.

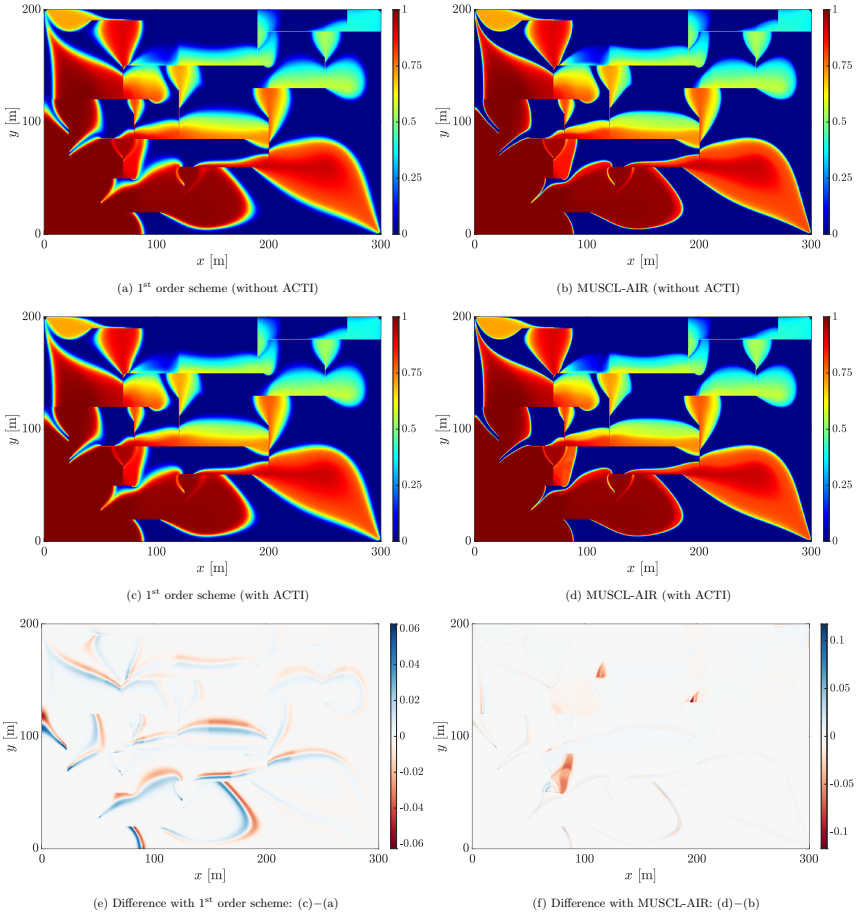

(a) 1st order scheme (without ACTI)

(b) MUSCL-AIR (without ACTI)

(c) 1st order scheme (with ACTI)

(d) MUSCL-AIR (with ACTI)

(e) Difference with 1st order scheme: (c)−(a)

(f) Difference with MUSCL-AIR: (d)−(b)

Figure 3.9: Concentration field after 300 days for global time stepping (a,b) and ACTI (c,d) as well as the difference between those fields (e,f) with the 1st order scheme (left) and MUSCL-AIR (right).

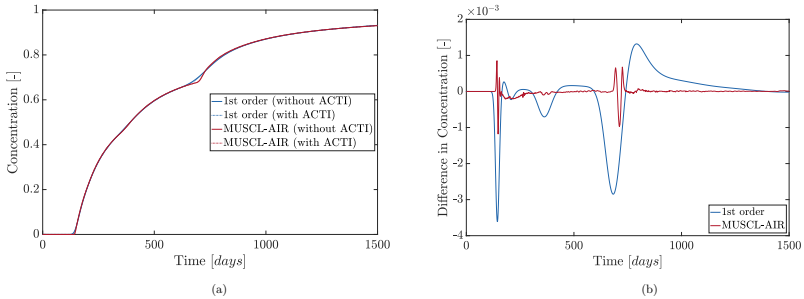

Figure 3.10: Arrival curves at the sink in the bottom-right corner (a) and the difference in the arrival curves obtained with ACTI and global time stepping (b).

If we use ACTI instead of global time stepping for this test case, 59 times fewer flux calculations and 75 times fewer cell updates are needed. Those values are directly related to the time refinement levels (Fig. 3.8a). The computational time is reduced likewise by a factor of 61 for the 1^{st} order scheme and 59 for MUSCL-AIR (Fig. 3.11). Here, we ran 600 separate simulations, each of which calculated tracer transport for a time period of $\Delta t_{\max}$ once with ACTI and once with global time stepping, to obtain mean and standard deviation of the ratio of computational time. The computational time scales roughly with the number of flux calculations, since this is the most expensive part of the simulation.

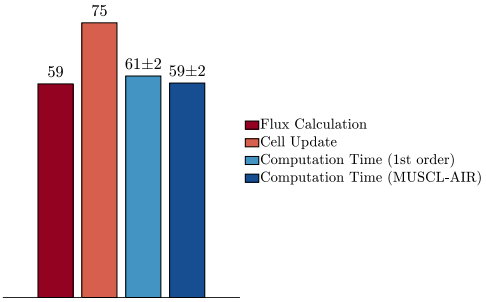

Figure 3.11: Ratio $[\,.\,]_{\text{withoutACTI}}/[\,.\,]_{\text{withACTI}}$ for number of flux calculations, number of cell updates and computational time. Mean and standard deviation of the ratio of computational time are obtained from 600 separate simulations.

3.3.3 Test case 3: single fracture with local grid refinement

Our third test case consists of a single horizontal fracture (Fig. 3.12a). In this case, we discretise the domain with a Cartesian grid with gradual refinement perpendicular to the fracture, such that the fracture contains 50 grid cells across (Fig. 3.12b). The height of the smallest grid cells is 1250 times smaller than the one of the largest ones. In this test case, inflow occurs through the left and outflow through the right boundary. Table 3.4 lists the parameter values of this test case.

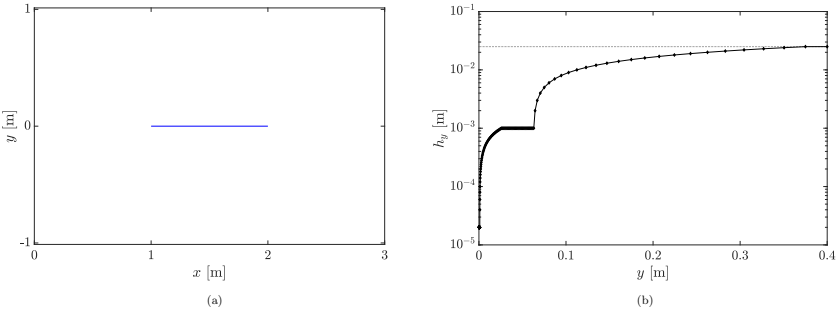

Figure 3.12: Geometry of the test case with a single horizontal fracture (a) and refinement h_y in and around the fracture (since the grid is symmetric, only the part of $y > 0$ is shown here) (b).

Size of domain	$3 \times 2.025 \times 1\,\mathrm{m}^3$
Number of grid cells	$300 \times 372 \times 1 = 111600$
Size of largest grid cell	$0.01 \times 0.025 \times 1\,\mathrm{m}^3$
Size of smallest grid cell	$0.01 \times 0.00002 \times 1\,\mathrm{m}^3$
Length of fracture	$l_f = 1\,\mathrm{m}$
Maximal time step for ACTI	$\Delta t_{\max} = 600\,\mathrm{s}$
CFL criterion	$CFL_{\max} = 0.5$
Flow rate through left boundary	$\dot{Q}_{\mathrm{left}} = 1 \times 10^{-5}\,\mathrm{m}^3/\mathrm{s}$

Table 3.4: Simulation parameters for the single fracture test case.

Fig. 3.13a shows the resulting flow field. Here, the highest velocities occur within the fracture and close to its tips. The lowest velocities are obtained at the stagnation points in the matrix just next to the midpoint of the fracture. The corresponding histogram (Fig. 3.13b) reveals that most cells have a velocity which is around three orders of magnitude smaller than the maximum velocity. This narrow peak in the histogram is due to the far field. Again, we expect that ACTI

performs well for such a broad velocity spectrum. Since the highest velocities coincide with regions where the grid is refined, we expect a huge performance increase with ACTI for this setup.

ACTI divides the grid cells into 15 levels (Fig. 3.14a), and the smallest local time step is $\Delta t_{\max}/2^{14} = 0.0366\,\mathrm{s}$. As expected, cells with a high level (i.e. small local time step) are located in the high-permeable fracture where the grid resolution is maximal. For global time integration, the time step obtained from the CFL criterion is 0.0391 s. With ACTI, the local CFL number is between 0.25 and 0.5 in all cells (Fig. 3.14b), whereas it is tiny in most of the domain for global time stepping (Fig. 3.14c).

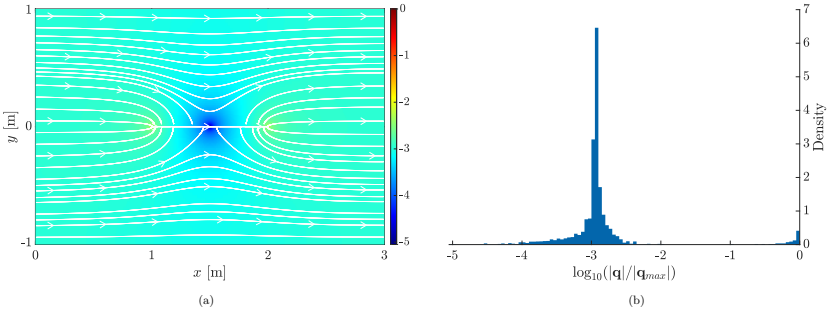

Figure 3.13: Logarithm of the magnitude of the normalised steady-state volumetric flux density, $\log_{10}(|\mathbf{q}|/|\mathbf{q}_{max}|)$, together with some streamlines (a) and the corresponding histogram (b).

The concentration fields calculated with ACTI and with global time stepping are very similar (Fig. 3.15). Like in the previous test case, the concentration front is exactly at the same location. For the 1$^{\mathrm{st}}$ order scheme, the concentration front is again slightly sharper with ACTI than for global time stepping. This is also visible in the arrival curves (Fig. 3.16). In addition, this test case nicely illustrates that the concentration front is much sharper with MUSCL-AIR as compared to the 1$^{\mathrm{st}}$ order scheme. The computation time with ACTI is around 80 times less than with global time stepping (Fig. 3.17). The numbers of flux calculations and cell updates are reduced by a similar factor. This speed-up allows us to obtain the concentration fields shown in Fig. 3.15 after only 1.5 hours instead of 5 days as in the case with global time stepping.

3.4 Discussion and conclusions

In this study, we have extended the adaptive conservative time integration (ACTI) scheme to transport of a scalar tracer concentration in fractured porous media and

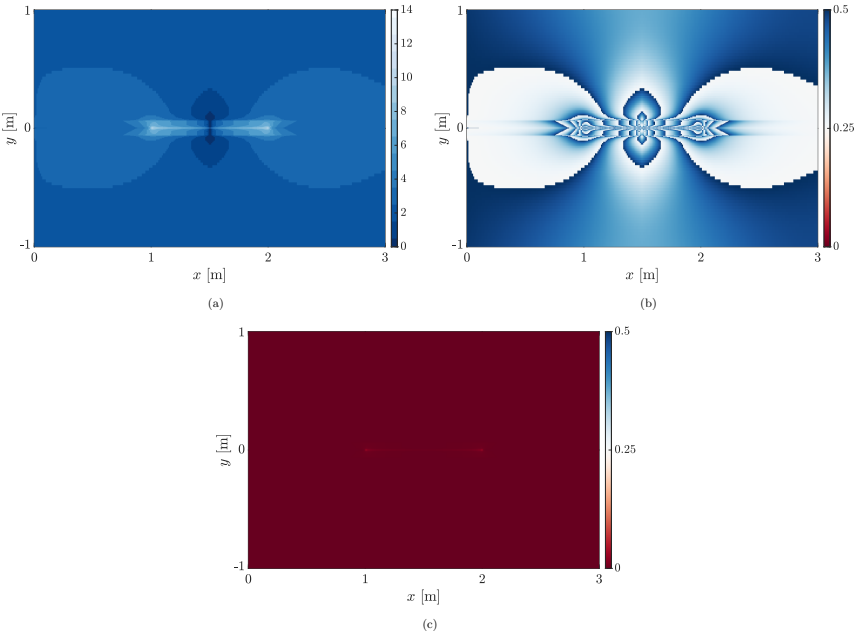

Figure 3.14: Levels (a) and local CFL numbers (b) with ACTI as well as local CFL numbers for global time stepping (c).

showed empirically that it produces accurate results at a much lower computational cost. In our test cases, we obtained impressive speed-up factors up to around 80 as compared to global time stepping. These speed-up factors stem from a comparable reduction in the number of flux calculations and cell updates.

Although we only used two idealised continuum models of fractured permeable rock in this study, one with a simplified synthetic fracture network and one with a single fracture and local grid refinement, we expect that our findings also apply to more realistic cases. Since the fractures are represented as heterogeneities in the matrix, either by upscaling or resolving them, the framework can be applied to any porous media where such permeability and porosity fields are available. Essentially, ACTI performs particularly well, if only a few cells require a very small time step, while most cells can be integrated with a much larger time step. Such huge differences in the local time step requirement can arise from channelling along nested preferential flow paths as well as from variable grid refinement.

The ACTI scheme is easy to implement and can be used with any explicit transport scheme. It works very well in combination with the first-order upwind

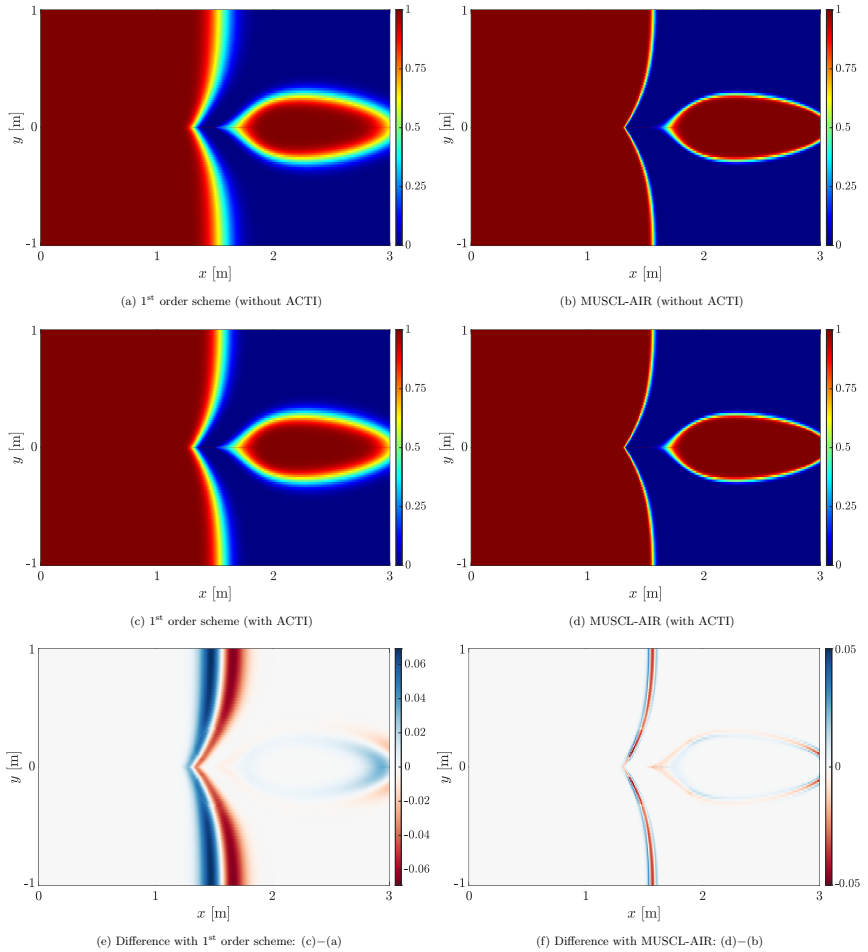

Figure 3.15: Concentration field after 15 h for global time stepping (a,b) and ACTI (c,d) as well as the difference between those fields (e,f) with the 1st order scheme (left) and MUSCL-AIR (right).

scheme that is still widely used in many applications. If we combine ACTI with a higher-order flux scheme to get sharper concentration fronts, we need to pay special attention to the stability of this scheme. A flux scheme that is stable for global time stepping is not necessarily stable in combination with ACTI due to

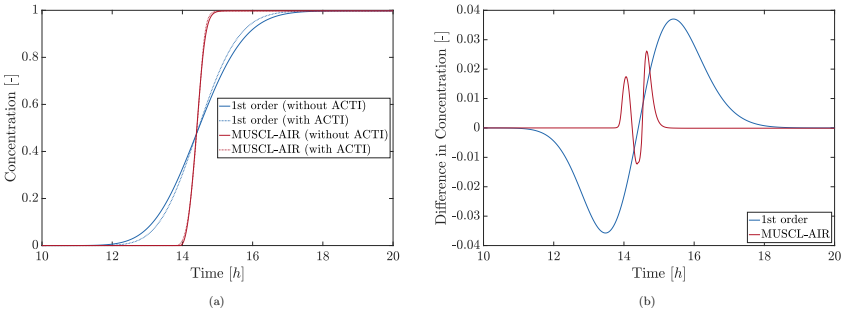

Figure 3.16: Arrival curves at the location $(x = 3, y = 0)$ (a) and the difference in the arrival curves obtained with ACTI and global time stepping (b).

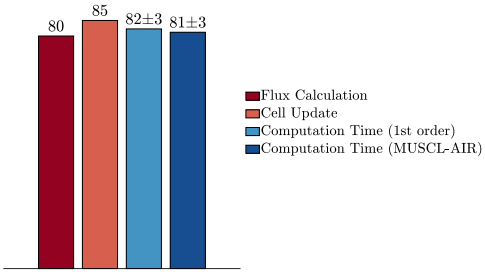

Figure 3.17: Ratio $[\,.\,]_{\text{withoutACTI}}/[\,.\,]_{\text{withACTI}}$ for number of flux calculations, number of cell updates and computational time. Mean and standard deviation of the ratio of computational time are obtained from 600 separate simulations.

the higher local CFL numbers. In this study, we empirically showed that the MUSCL scheme with advection of inclined reconstruction (MUSCL-AIR) fulfils this requirement. Future work is required to analytically investigate the stability of higher-order schemes in combination with ACTI.

In practice, the lower computational cost of ACTI compared to conventional global time stepping means that for given computational resources, ACTI allows for more accurate solutions as can be achieved by using a higher-order flux scheme and/or a finer spatial grid resolution. This is essential when sharp concentration fronts are present and numerical dispersion must be kept to a minimum. One example, indicated by a very high Péclet number, is advection-dominated transport at the reservoir scale. Another example is non-diffusive, non-reactive tracer transport in a viscous fluid as characterised by a high Schmidt number. Almost

no mixing would occur within a fracture if the flow was laminar and creeping, as famously demonstrated by the Taylor-Couette flow reversibility. This effect can only be captured if the grid is sufficiently refined within the fracture. Test case 3 somewhat resembles such a situation where we obtain a sharp concentration front at the exit of the fracture by using 50 grid cells across the fracture aperture and a higher-order flux scheme, albeit without resolving velocity variations across the fracture using the Stokes equation. However, the precipitation of minerals by fluid mixing within fractures is one of the reasons why one finds high-grade ore mineralisation within them (e.g. Phillips, 1990). In test case 2, we represent the fractures with a single pixel row which corresponds to the case of perfect mixing across the fracture aperture. Consequently, the concentration front at the exit of fractures is less sharp.

With adaptive time stepping methods such as ACTI, explicit time integration schemes become more attractive as an alternative to the widely used (usually first-order) implicit schemes. Therefore, future work should contrast and compare the accuracy and computational costs of explicit schemes using ACTI with implicit schemes, and related implementation dependencies of the two methods.

Thus far, we only considered 2D test cases with Cartesian grids, however, it is straightforward to extend the ACTI scheme to 3D and unstructured grids where ACTI might have even greater benefits, especially when using spatially adaptive grid refinement. ACTI is therefore a promising tool to efficiently calculate transport in various sub-surface applications such as geothermal or hydrocarbon reservoirs, carbon dioxide sequestration, wastewater injection and groundwater flow. Here, we considered idealised test cases targeting tracer transport in fractured porous media, but ACTI should also be applicable to multi-phase flow or sequentially coupled flow and transport problems.

4 Data Assimilation

4.1 Introduction

Accurate modelling of flow and transport is essential in understanding and predicting the behaviour of subsurface reservoirs. For this, precise knowledge of the state (e.g. pressure and concentration fields) and parameters (e.g. matrix permeability, porosity, and fracture properties) is required. However, the available data is usually sparse or incomplete, associated with uncertainty, and often consists only of statistical information or indirect measurements (as discussed in Section 2.3). Consequently, the estimates of the state and parameters of a subsurface reservoir are also associated with uncertainties.

Data assimilation (DA) or history matching is a standard tool for reducing uncertainties in state and parameters. DA combines the current (i.e. prior) knowledge of a system with whatever uncertain measurement data is available for an improved (i.e. posterior) prediction of the system performing some form of optimisation. The optimisation process can be classified into classical, statistical, and hybrid versions. In classical optimisation, we seek the minimum of a cost function describing the discrepancy between the model and measurements. On the other hand, statistical optimisation minimises the uncertainty of the model error based on statistical estimation theory (Asch et al., 2016). DA is closely related to inverse modelling and uncertainty quantification.

DA has its origins in numerical weather predictions (Lorenc, 1986; Houtekamer & Mitchell, 1998; Houtekamer & Zhang, 2016; Bannister, 2017) but has become increasingly popular in many other fields, ranging from subsurface applications (Lorentzen et al., 2001; Hendricks Franssen & Kinzelbach, 2008; Aanonsen et al., 2009; Vogt et al., 2012; Evensen & Eikrem, 2018), oceanography (Ghil & Malanotte-Rizzoli, 1991; Bertino et al., 2003; Béal et al., 2010), computational fluid dynamics and turbulence modelling (Kato et al., 2015; Li et al., 2017; Brenner et al., 2022; Piroozmand et al., 2023), to biology and medicine (Quaife et al., 2008; Epp et al., 2020; Evensen et al., 2021; Lim et al., 2023).

This chapter provides an overview of popular DA methods with a focus on statistical approaches and reviews the application of DA in fractured porous media. For a thorough discussion of the topic, see e.g. Asch et al. (2016), Bannister (2017), Carrassi et al. (2018) and Evensen et al. (2022).

4.2 Problem formulation

This section presents the formulation for describing the dynamics of a stochastic time-varying system and its inherent uncertainty. Further, it introduces statistical methods that form the foundation for estimating these uncertain model components.

4.2.1 Forward and observation model

A noisy, non-linear, discrete time-varying system can describe or approximate many physical processes. The evolution of such a system is given by

$$x_{k+1} = \mathcal{M}(x_k,\, u_k,\, \theta) + \upsilon_k \;, \tag{4.1}$$

where the non-linear function $\mathcal{M}(\,.\,)$ relates the state vector $x_k \in \mathcal{R}^n$ and control (or input) vector $u_k \in \mathcal{R}^l$ at time step k as well as the time-independent model parameters $\theta \in \mathcal{R}^p$ to the state at time step $k+1$. We thereby assume that $\mathcal{M}(\,.\,)$ is a deterministic function and that the model error $\upsilon_k \in \mathcal{R}^n$ is additive. We further assume here that the system can be modelled as a 1^{st}order Markov process where the future does not depend on the past if the present is known.

In some instances, we obtain the discrete system of Eq. (4.1) by discretising a noisy, non-linear, continuous time-varying system

$$\dot{x}(t) = \mathcal{Q}\,(x(t),\, u(t),\, \upsilon(t),\, \theta) \tag{4.2}$$

in time. Here, $\mathcal{Q}(\,.\,)$ is a continuous non-linear function describing the system, and $\upsilon(t)$ is a continuous random variable expressing the model noise.

A measurement of the system $y \in \mathcal{R}^m$ is obtained by

$$y_k = \mathcal{H}(x_k) + \omega_k \;, \tag{4.3}$$

where $\mathcal{H}(\,.\,)$ is the observation model, a potentially non-linear function that relates the state vector to the measurement. Again, we assume here that the measurement noise $\omega_k \in \mathcal{R}^m$ is additive. We thereby distinguish between actual measurements d observed in reality serving as reference measurements in the DA framework and predicted measurements from simulations. Note that we use the terms measurement and observation interchangeably.

In some cases, the model is linear, or we approximate it as such. By linearising Eqs. (4.1) and (4.3), we obtain

$$x_{k+1} = A_k x_k + B u_k + \upsilon_k \quad \text{and} \tag{4.4}$$

$$y_k = H_k x_k + \omega_k \;, \tag{4.5}$$

where $A \in \mathcal{R}^{n\times n}$ is the state matrix, $B \in \mathcal{R}^{n\times l}$ is a matrix describing the effect of the control vector, and $H_k \in \mathcal{R}^{m\times n}$ is the observation matrix. Those matrices generally depend on model parameters.

A popular example in control theory is a vehicle with position and velocity as state variables. The throttle acts as control input, relevant model parameters might include the wheel diameter, and slip between the wheels and the road can be responsible for model noise. For such a vehicle, we can obtain a noisy measurement of its location from a GPS signal.

4.2.2 Uncertain model variables

In the systems described above, all variables can generally be associated with uncertainty. Such random variables are described by a probability density function (PDF) and can be expressed with expected value $(\bar{.})$ and fluctuations $(.)'$, i.e.,

$$x_0 = \bar{x}_0 + x_0' \tag{4.6}$$
$$\theta = \bar{\theta} + \theta' \tag{4.7}$$
$$u_k = \bar{u}_k + u_k' \tag{4.8}$$
$$\upsilon_k = 0 + \upsilon_k' \tag{4.9}$$
$$\omega_k = 0 + \omega_k' \tag{4.10}$$
$$x_k = \bar{x}_k + x_k' \tag{4.11}$$
$$y_k = \bar{y}_k + y_k' \ . \tag{4.12}$$

The system's initial state x_0, the model parameters θ, control inputs u_k, model errors υ_k and measurement errors ω_k are generally considered mutually independent. On the other hand, the state and measurements of the system, x_k and y_k respectively, are dependent random variables. The PDFs describing the random variables in Eqs. (4.6) to (4.12) can generally have arbitrary shapes; however, many DA methods require them to be Gaussian.

The state vector z of the DA problem contains all the uncertain quantities we want to estimate. In its full form, the DA state vector reads

$$z = \left[x_0^T,\, \theta^T,\, u_1^T,\, ...,\, u_K^T,\, \upsilon_1^T,\, ...,\, \upsilon_K^T\right]^T \quad \text{or} \tag{4.13}$$
$$z = \left[x_0^T,\, x_1^T,\, ...,\, x_K^T,\, \theta^T,\, u_1^T,\, ...,\, u_K^T\right]^T \ , \tag{4.14}$$

depending on the formulation of the DA problem (Evensen et al., 2022). Thus, we can reformulate Eq. (4.3) as

$$y_k = \mathcal{H}\left(\mathcal{M}(z)\right) + \omega_k = \mathcal{G}(z) + \omega_k \ . \tag{4.15}$$

In some DA problems, we might consider one or several of the variables as known and model them as deterministic variables. This work assumes that the control input (e.g. boundary condition of flow and transport simulations) is known exactly. Consequently, the DA state vector reduces to

$$z = \left[x_0^T,\, x_1^T,\, ...,\, x_K^T,\, \theta^T\right]^T \ . \tag{4.16}$$

In Chapters 5 and 6, we consider pure parameter estimation, i.e., $z = \theta$, and assume that any model error can be included in the measurement errors, such that Eq. (4.15) reduces to $y_k = \mathcal{G}(\theta) + \omega_k$.

4.2.3 Inverse problem

The forward problem described in Section 4.2.1 predicts the behaviour of a system given its initial state, control inputs and model parameters. It is usually well-posed and relatively straightforward to solve, even though it might be computationally expensive for large and complex systems.

We are often interested in calculating a system's model parameters or state from a set of measurements. Calculating the cause from the effect is described by the corresponding inverse problem (Asch et al., 2016). Contrary to the forward problem, the inverse problem is often ill-posed and can either have many possible solutions or none, depending on whether it is under- or over-determined. Further, it can be highly non-linear with many local minima. This makes solving the inverse problem very challenging. The following sections present tools and methods useful for describing and solving inverse problems.

4.2.4 Bayes' theorem

Bayes' theorem, named after the English statistician Thomas Bayes, can be viewed as the basis of most DA methods (e.g. Evensen et al., 2022). The theorem provides a formula for the probability distribution of the quantity of interest, here the DA state vector z, given the noisy measurement of a related quantity d. The resulting conditional distribution

$$f_{Z|D}(z|d) = \frac{f_{D|Z}(d|z) f_Z(z)}{f_D(d)} = \frac{f_{D|Z}(d|z) f_Z(z)}{\int_{-\infty}^{\infty} f_{D|Z}(d|z) f_Z(z)\,\mathrm{d}z} \tag{4.17}$$

is called the posterior PDF of z. The prior $f_Z(z)$ is the probability distribution of z before any additional information (i.e. measurements of d) is available. The likelihood $f_{D|Z}(d|z)$ is the probability distribution of the observed quantity d given a particular value of z and can be obtained from Eq. (4.3). The denominator $f_D(d)$, sometimes called marginal or evidence, serves as a normalisation constant and can be calculated by integrating the product of likelihood and prior over z.

In subsequent sections, we drop the subscripts of f for convenience and brevity.

4.2.5 Estimators

Estimators are statistical methods used to make predictions or estimates about unknown quantities or parameters based on observed data or prior information. There is a wide variety of estimators available, each serving different purposes.

When dealing with DA problems, particularly in estimating the posterior distribution, we often encounter two fundamental objectives. One approach seeks to estimate the most probable value of an unknown parameter. The other approach aims to find an unbiased estimator that minimises variance or, in other words, is the most precise and accurate. This section provides a concise overview of these two fundamental concepts.

Maximum a posteriori estimate

Calculating the most probable posterior DA state corresponds to finding the maximum *a posteriori* (MAP) estimate

$$z_{\text{MAP}} = \arg\max_{z} f(z|d) \ . \tag{4.18}$$

When the posterior PDF is a smooth function, we can represent it in the form

$$f(z|d) \propto \exp\left(-\mathcal{J}(z)\right) \ , \tag{4.19}$$

as demonstrated, for instance, by Evensen et al. (2022). This form is derived based on the fact that a PDF is always non-negative. Maximising $f(z|d)$ in Eq. (4.18) is then equivalent to minimising the cost function $\mathcal{J}(z)$, leading to the MAP estimate

$$z_{\text{MAP}} = \arg\min_{z} \mathcal{J}(z) \ . \tag{4.20}$$

In scenarios where both the prior and the likelihood follow Gaussian distributions, characterised by the prior state covariance matrix P_0 and the measurement errors covariance matrix R, respectively, the cost function takes the form

$$\mathcal{J}(z) = \frac{1}{2}\left(z - z_0\right)^T P_0^{-1}\left(z - z_0\right) + \frac{1}{2}\left(\mathcal{G}(z) - d\right)^T R^{-1}\left(\mathcal{G}(z) - d\right) \ , \tag{4.21}$$

where z_0 denotes the prior state estimate.

While obtaining the most probable state can be highly valuable, it is important to note that the MAP estimate focuses solely on this point estimate and does not provide information about the full posterior distribution or the associated uncertainty.

Minimum mean squared error estimate

The second approach involves finding an estimator that is both unbiased and precise. *Unbiased* means that the expected value of an estimator $\hat{z}$ equals the true value z, expressed as

$$\mathrm{E}[\hat{z}] = z \ . \tag{4.22}$$

On the other hand, *Precision* is characterised by the estimator's variance. Finding the most precise estimator given some observation data d corresponds to obtaining the minimum variance estimate

$$z_{\mathrm{MV}} = \arg\min_{\hat{z}} \mathrm{Var}\left[\hat{z}|d\right] = \arg\min_{\hat{z}} \mathrm{E}\left[\left(\hat{z} - \mathrm{E}[\hat{z}]\right)^T \left(\hat{z} - \mathrm{E}[\hat{z}]\right)\middle| d\right] \ . \tag{4.23}$$

When an MV estimator is also unbiased, it results in the minimum mean squared error (MMSE) estimate

$$z_{\mathrm{MMSE}} = \arg\min_{\hat{z}} \mathrm{E}\left[(\hat{z} - z)^T (\hat{z} - z)|d\right] = \mathrm{E}\left[z|d\right] = \int z f(z|d)\,\mathrm{d}z \ , \tag{4.24}$$

corresponding to the mean of the true posterior distribution.

The best linear unbiased estimator (BLUE) is a specific type of estimator that is both linear and unbiased and achieves the minimum variance among all linear unbiased estimators. Therefore, BLUE represents a particular implementation of the MMSE estimate in the context of linear estimators.

While the MMSE estimate provides a precise and accurate estimate, it does not guarantee that the estimate is actually likely. In the case of a bimodal distribution, the MMSE estimate may return a value with a low probability of occurrence. However, all these estimators yield the same result for linear forward and observation models with Gaussian error statistics.

4.3 Variational data assimilation

Variational DA, also called classical DA, seeks the most probable posterior state for Gaussian distributions of the prior and the likelihood by minimising the cost function presented in Eq. (4.21). Minimising the cost function can be achieved by setting its gradient,

$$\nabla_z \mathcal{J}(z) = P_0^{-1}(z - z_0) + \nabla_z \mathcal{G}(z)\, R^{-1}\left(\mathcal{G}(z) - d\right) = 0 \ , \tag{4.25}$$

to zero, where the model sensitivity $\nabla_z \mathcal{G}(z)$ is the gradient of the predicted measurements to the state vector. This approach is however rarely used as it is costly in high-dimensional problems and $\mathcal{G}(z)$ is often a non-linear function.

Another approach is finding the minimum of the cost function iteratively, i.e.,

$$z^{i+1} = z^i - \gamma^i B^i \nabla_z \mathcal{J}(z^i) \ , \tag{4.26}$$

where the positive scalar γ is the step size, and B is a matrix (e.g. Evensen et al., 2022). Those two parameters distinguish different minimisation methods. We obtain a gradient descent method for $B^i = I$. Choosing $\gamma^i = 1$ and B as the inverse of the Hessian

$$\nabla_z \nabla_z \mathcal{J}(z) = P_o^{-1} + \nabla_z \mathcal{G}(z)\, R^{-1}\left(\nabla_z \mathcal{G}(z)\right)^T + \nabla_z \nabla_z \mathcal{G}(z)\, R^{-1}\left(\mathcal{G}(z) - d\right) \tag{4.27}$$

results in the Newton method. The Gauss-Newton method approximates the Hessian by omitting the last term in Eq. (4.27).

Even with gradient descent, the simplest method of solving Eq. (4.26), we still need to evaluate the gradient of the cost function. The adjoint method (e.g. Asch et al., 2016) provides an elegant and efficient solution, roughly at the cost of solving the forward problem once. Continuous and discrete adjoint-based data assimilation exist; the latter can be combined, e.g., with finite differences or automatic differentiation. Applying variational DA to stationary problems is called 3D-Var, while 4D-Var tackles time-dependent problems.

A thorough discussion of variational DA methods can be found, e.g. in Asch et al. (2016) and Evensen et al. (2022).

4.4 Statistical data assimilation

While variational DA methods often aim to find the MAP estimate, many statistical DA techniques rely on the MMSE estimate. In this section, we provide an overview of several prominent statistical DA techniques, with particular emphasis on ensemble-based methods.

4.4.1 Simple example

Let's demonstrate the principal functionality of statistical DA on a straightforward system described by a single time-independent state variable. Suppose we have prior knowledge of this model variable associated with uncertainty, expressed with a Gaussian distribution with mean x_b and variance σ_b^2. We obtain a measurement x_m of the model variable where the variance σ_m^2 describes the measurement error. Combining the prior knowledge and the measurement, we obtain an updated, posterior estimate of the model variable by applying Bayes' theorem (Eq. (4.17)). Essentially, we multiply the PDFs of prior and measurement, which results here in a posterior PDF $f(x|y)$ that is again Gaussian. The mean (here coinciding with the MAP estimate) and variance of the posterior distribution is

$$x_a = x_b + \frac{1}{1+\alpha}(x_m - x_b) \quad \text{and} \tag{4.28}$$

$$\sigma_a^2 = \left(\frac{1}{\sigma_m^2} + \frac{1}{\sigma_b^2}\right)^{-1} , \tag{4.29}$$

which is the best linear unbiased estimator (BLUE) for this problem. Depending on the variance of measurement and prior knowledge, described by the ratio $\alpha = \sigma_m^2/\sigma_b^2$, BLUE puts more weight on one or the other (Fig. 4.1).

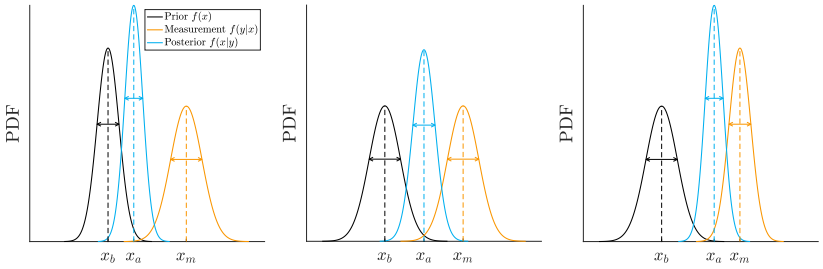

(a) $\sigma_b < \sigma_m$ (b) $\sigma_b = \sigma_m$ (c) $\sigma_b > \sigma_m$

Figure 4.1: Posterior PDF for different prior and measurement PDFs. The arrows indicate the standard deviations σ.

4.4.2 Kalman filter

We now extend the approach from the previous section to the noisy linear discrete-time dynamic system given in Eqs. (4.4) and (4.5), where we assume Gaussian error statistics. For such a system, several statistical methods can lead to the BLUE of the state given the previous state estimate and the measurement up to that point. One of them is the Kalman filter (KF) introduced by Kalman (1960), a recursive process that iteratively performs a prediction/forecast step and a correction/update/analysis step (e.g. Humpherys et al., 2012; Asch et al., 2016). For simplicity, we consider only pure-state estimation in this section and assume that all model parameters and control inputs are known exactly.

The KF is initialised as

$$x_{0|0} = \mathrm{E}[x_0] \tag{4.30}$$
$$P_{0|0} = \mathrm{Cov}[x_0] \tag{4.31}$$

where x and P describe the state estimate and its covariance, respectively. x_0 represents the initial prior knowledge of the model states. The subscript $[\,.\,]_{b|a}$ denotes the value of a quantity at time step b given information up to time step a. This section highlights prior quantities in purple and posterior quantities in green for better readability. Note that the initialised values of Eqs. (4.30) and (4.31) are treated as posterior quantities in the here presented algorithm.

In the prediction step, the state vector and its covariance are propagated forward in time until new measurements become available. While the states propagate according to the deterministic part of Eq. (4.4), the covariance is affected by the model error v. The resulting prior estimate at time step k (i.e. before any

measurement data from that time step is incorporated) is

$$x_{k|k-1} = A_{k-1}x_{k-1|k-1} + B_{k-1}u_{k-1} \tag{4.32}$$

$$P_{k|k-1} = A_{k-1}P_{k-1|k-1}A_{k-1}^T + Q_{k-1} \ , \tag{4.33}$$

where $Q_k = \mathrm{Cov}[\upsilon_k]$ is the covariance of the model error.

In the update step, we compare the reference measurements d_k to the predicted measurements $\bar{y}_k = H_k x_{k|k-1}$ and adjust the estimates for x and P accordingly. Note that the reference measurements observed in reality are affected by the measurement noise characterised by the covariance R_k, while the predicted measurements represent expected values. The resulting posterior estimate at time step k (i.e. after the measurement data from that time step is incorporated) is

$$x_{k|k} = x_{k|k-1} + K_k\left(d_k - H_k x_{k|k-1}\right) \tag{4.34}$$

$$P_{k|k} = \left(I_n - K_k H_k\right) P_{k|k-1} \ , \tag{4.35}$$

where

$$K_k = P_{k|k-1}H_k^T\left(H_k P_{k|k-1}H_k^T + R_k\right)^{-1} \tag{4.36}$$

is the Kalman gain $\in \mathcal{R}^{n\times m}$ and I_n is the $n \times n$ identity matrix.

The application of the KF is restricted to dynamic systems that can be described by linear model and measurement operators. For non-linear systems, such as Eqs. (4.1) and (4.3), one can apply the extended Kalman filter (EKF), which linearises the system about the current state estimate (e.g. Evensen, 1992; Asch et al., 2016). The EKF is however a sub-optimal scheme that provides only approximations of the true conditional mean and variance.

Both the KF and the EKF become computationally prohibitive for states containing a large number of variables. The limiting factor is propagating and storing the $n \times n$ covariance matrix P. In addition, linearising the system in EKF is costly as well. In the following, we present methods better suited for common DA problems in subsurface applications or numerical weather prediction.

4.4.3 Ensemble Kalman filter

The ensemble Kalman filter (EnKF), introduced by Evensen (1994), is an ensemble approximation of the original Kalman filter (Section 4.4.2) and does not require linearised or adjoint versions of the model or the observation operator. The EnKF is optimal only for linear models and Gaussian errors but works approximately also for (weakly) non-linear models. Again, we consider pure-state estimation with known model parameters and control inputs, but the EnKF can easily be extended to more general DA problems. There exists a wide variety of EnKF versions; for a review, see e.g. Houtekamer & Zhang (2016), Keller et al. (2018), or Evensen et al. (2022). This section presents one of them, the stochastic EnKF.

We initialise the EnKF by sampling an ensemble of N realisations

$$\mathcal{X}_{0|0} = \left[x_{0|0}^{(1)},\, x_{0|0}^{(2)},\, \ldots,\, x_{0|0}^{(N)}\right] \tag{4.37}$$

from the prior distribution. In the prediction step, every realisation is propagated independently according to the forward model described in Eq. (4.1), i.e.

$$x_{k|k-1}^{(i)} = \mathcal{M}\left(x_{k-1|k-1}^{(i)},\, u_{k-1},\, \theta\right) + \upsilon_{k-1}^{(i)}\,. \tag{4.38}$$

The corresponding predicted measurements for a particular ensemble realisation are given by the expected value of the observation model Eq. (4.3), i.e.,

$$\bar{y}_{k|k-1}^{(i)} = \mathrm{E}\left[y_{k|k-1}^{(i)}\right] = \mathcal{H}\left(x_{k|k-1}^{(i)}\right)\,. \tag{4.39}$$

Thus, the prediction step of EnKF can be parallelised efficiently and easily.

The update step, on the other hand, is less straightforward and differs from version to version. The stochastic EnKF perturbs the difference between the reference measurements d_k and the predicted measurements $\bar{y}_{k|k-1}^{(i)}$ with measurement noise $\omega_k^{(i)} \sim \mathcal{N}(0, R_k)$. These perturbations ensure that the variance of the posterior ensemble is correctly predicted. Following van Leeuwen (2020), we apply the perturbations ω_i to the predicted ensemble measurements, whereas other implementations (e.g. Asch et al., 2016; Evensen et al., 2022) apply them to the reference measurements. The posterior realisations are

$$x_{k|k}^{(i)} = x_{k|k-1}^{(i)} + K_k\left(d_k - \left(\bar{y}_{k|k-1}^{(i)} + \omega_k^{(i)}\right)\right)\,, \tag{4.40}$$

where the sets of all $x_{k|k-1}^{(i)}$ and $x_{k|k}^{(i)}$ are called prior and posterior ensembles, respectively. Following Asch et al. (2016), we approximate the Kalman gain

$$\begin{aligned} K_k &= P_{k|k-1} H_k^T \left(H_k P_{k|k-1} H_k^T + R_k\right)^{-1} \\ &\simeq X_{k|k-1} \left(Y_{k|k-1}\right)^T \left[Y_{k|k-1} \left(Y_{k|k-1}\right)^T\right]^{-1} \end{aligned} \tag{4.41}$$

with the normalised anomalies

$$\left[X_{k|k-1}\right]_i = \frac{1}{\sqrt{N-1}} \left(x_{k|k-1}^{(i)} - \frac{1}{N}\sum_{j=1}^{N} x_{k|k-1}^{(j)}\right) \quad \text{and} \tag{4.42}$$

$$\left[Y_{k|k-1}\right]_i = \frac{1}{\sqrt{N-1}} \left(\left(\bar{y}_{k|k-1}^{(i)} + \omega_k^{(i)}\right) - \frac{1}{N}\sum_{j=1}^{N} \left(\bar{y}_{k|k-1}^{(j)} + \omega_k^{(j)}\right)\right)\,. \tag{4.43}$$

Here, $P_{k|k-1} = X_{k|k-1}(X_{k|k-1})^T$ is the ensemble approximation of the forecast error covariance matrix of the DA state vector, and H_k is the linearised version

of the observation operator $\mathcal{H}(.)$. Note that $[\,.\,]_i$ denotes the i-th column of the corresponding matrix.

Algorithm 1 presents the pseudo-code of a stochastic EnKF update step. Note that various implementations of the update step exist that slightly differ from each other (e.g. Evensen et al., 2022). The EnKF routine, which consists of alternate prediction and update steps, is shown in Algorithm 2.

Algorithm 1 Stochastic EnKF update based on Evensen (1994), Asch et al. (2016) and van Leeuwen (2020).

Input variables
  $\mathcal{Z} \in \mathcal{R}^{n \times N}$ ▷ Ensemble of prior DA state vectors
  $\mathcal{Y} \in \mathcal{R}^{m \times N}$ ▷ Ensemble of predicted measurements
  $d \in \mathcal{R}^{m \times 1}$ ▷ Reference measurements
  $R \in \mathcal{R}^{m \times m}$ ▷ Measurement error covariance matrix
function EnKF_Update($\mathcal{Z}$, $\mathcal{Y}$, d, R)
  for $i = 1, ..., N$ **do**
    $[\Omega]_i \sim \mathcal{N}(0, R)$ ▷ Draw perturbations
  end for
  $\Pi = (I - \frac{1}{N} 1 1^T)/\sqrt{N-1}$ ▷ Identity matrix $I \in \mathcal{R}^{N \times N}$, vector of ones $1 \in \mathcal{R}^{N \times 1}$
  $X = \mathcal{Z}\Pi$ ▷ Eq. (4.42)
  $Y = (\mathcal{Y} + \Omega)\Pi$ ▷ Eq. (4.43)
  $K = XY^T(YY^T)^{-1}$ ▷ Kalman gain Eq. (4.41)
  $\mathcal{Z} = \mathcal{Z} + K(d1^T - \mathcal{Y} + \Omega)$ ▷ Update DA state vectors Eq. (4.40)
  return $\mathcal{Z}$
end function

4.4.4 Ensemble smoother

Filtering estimates the current state of a system given past and present measurements. The classical EnKF described in the previous section updates the system's state whenever new measurements are available. The system's current state thereby depends on past measurements through previous EnKF updates. Smoothing, on the other hand, considers past, present and possibly future measurements for estimating the system's current state, which is equivalent to updating past and present states with current measurements (Asch et al., 2016).

Various formulations of ensemble smoothers exist (Evensen, 2009; Evensen et al., 2022), some of which are described below. The original formulation of the ensemble smoother (ES) was introduced by van Leeuwen & Evensen (1996). The ES collects all measurements in space and time over a certain time period called the assimilation window. At the end of the assimilation window, it updates all model states within the current window before moving on to the next one. The ensemble Kalman smoother (EnKS) (Evensen & van Leeuwen, 2000) additionally also updates the model states within previous assimilation windows. The asynchronous

Algorithm 2 DA routine using the ensemble Kalman filter (EnKF) (Evensen, 1994). Here, we assume no error in the forward model and known controls.

Input variables
  $\mathcal{M}(\,.\,)$ ▷ Forward model
  $\mathcal{H}(\,.\,)$ ▷ Observation model
  $\mathcal{Z}_0 \in \mathcal{R}^{n \times N}$ ▷ Ensemble of initial DA state vectors
  $d_k \in \mathcal{R}^{m_k \times 1}$ ▷ Reference measurements at time steps k
  $R_k \in \mathcal{R}^{m_k \times m_k}$ ▷ Measurement error covariance matrix at time step k
for $k = 1, ..., K$ **do** ▷ Loop over time steps
  for $i = 1, ..., N$ **do** ▷ Loop over ensemble members
    $[\mathcal{Z}_k]_i = \mathcal{M}(\,[\mathcal{Z}_{k-1}]_i\,)$ ▷ Prediction step Eq. (4.38)
    $[\mathcal{Y}_k]_i = \mathcal{H}(\,[\mathcal{Z}_k]_i\,)$ ▷ Predicted measurements Eq. (4.39)
  end for
  $\mathcal{Z}_k = \text{ENKF\_Update}(\mathcal{Z}_k, \mathcal{Y}_k, d_k, R_k)$ ▷ Update step (Algorithm 1)
end for

EnKF (AEnKF) (Sakov et al., 2010) uses measurements that are distributed over the assimilation window in an EnKF update, and as such it is essentially a combination of EnKF and EnKS. Skjervheim et al. (2011) consider the whole simulation period as one assimilation window in their ES framework (see Algorithm 3). This greatly simplifies the implementation as the forward simulation (i.e. the reservoir simulator in subsurface applications) does not need to be interrupted. Note that the term *ensemble smoother* is used in literature for the original version of van Leeuwen & Evensen (1996) and the simplified ES of Skjervheim et al. (2011).

Algorithm 3 DA routine using the ensemble smoother (ES) with only one assimilation window (Skjervheim et al., 2011).

Input variables
  $\mathcal{M}(\,.\,)$ ▷ Forward model
  $\mathcal{H}(\,.\,)$ ▷ Observation model
  $\mathcal{Z}_0 \in \mathcal{R}^{n \times N}$ ▷ Ensemble of initial DA state vectors
  $d \in \mathcal{R}^{m \times 1}$ ▷ Reference measurements at all time steps
  $R \in \mathcal{R}^{m \times m}$ ▷ Measurement error covariance matrix including all time steps
for $i = 1, ..., N$ **do** ▷ Loop over ensemble members
  $z_0 = [\mathcal{Z}_0]_i$
  for $k = 1, ..., K$ **do** ▷ Loop over time steps
    $z_i = \mathcal{M}(z_{k-1})$ ▷ Prediction step Eq. (4.38)
    $\bar{y}_k = \mathcal{H}(\,z_k\,)$ ▷ Predicted measurements Eq. (4.39)
  end for
  $[\mathcal{Z}]_i = [\,z_0^T\,,\, z_1^T\,,\, \ldots\,,\, z_K^T]^T$
  $[\mathcal{Y}]_i = [\,\bar{y}_1^T\,,\, \bar{y}_2^T\,,\, \ldots\,,\, \bar{y}_K^T]^T$
end for
$\mathcal{Z} = \text{ENKF\_Update}(\mathcal{Z}, \mathcal{Y}, d, R)$ ▷ Update step (Algorithm 1)

Smoothers are generally more flexible regarding the incorporation of measurements compared to filters. This is particularly true for the ES of Skjervheim et al. (2011), which uses only one assimilation window. It can effortlessly incorporate completely asynchronous measurements whose time stamps differ from realisation to realisation, for example, measurements of the time when water breakthrough occurs at a well or when a tracer concentration reaches a certain threshold, and deal with correlations between measurements obtained at different times.

For linear forward and observation models and Gaussian error statistics, results from ensemble smoothers and EnKF are equivalent (Evensen, 2004). Skjervheim et al. (2011) also obtained very similar results with ES and EnKF for the two reservoir history-matching problems considered in their study. For non-linear models however, the single update with ES is insufficient and inferior to the sequential updates of the EnKF (van Leeuwen & Evensen, 1996; Evensen & van Leeuwen, 2000; Chen & Oliver, 2012). Iterative versions of the ES, such as the ensemble randomised maximum likelihood method (EnRML) (Chen & Oliver, 2012, 2013) or the ensemble smoother with multiple data assimilation (ESMDA) (Emerick & Reynolds, 2013), were developed for weakly to modestly non-linear systems and have gained popularity in recent years. The ESMDA is described in more detail in the next section.

4.4.5 Ensemble smoother with multiple data assimilation

The ensemble smoother with multiple data assimilation (ESMDA), proposed by Emerick & Reynolds (2013), is an iterative method widely used for non-linear DA problems. As an ensemble smoother, the ESMDA collects all measurements in time and space during the forward simulation and performs an update step at the end of the assimilation window. It then alternately reruns the forward simulation from the beginning of the assimilation window with the updated DA states and performs update steps with the same reference measurements.

A repeated assimilation of the same reference measurement puts however more and more weight on them compared to the prior knowledge of the DA state vector. In order to compensate for this effect and guarantee a correct posterior distribution in a linear model with Gaussian error statistics and infinite ensemble size, the ESMDA inflates the measurement error covariance matrix

$$\widetilde{R}_j = \alpha_j R \quad \text{such that} \quad \sum_{j=1}^{J} \frac{1}{\alpha_j} = 1 \,, \tag{4.44}$$

where J is the number of ESMDA iterations. While there is no proof of convergence in non-linear DA problems (Evensen & Eikrem, 2018), the ESMDA works fine in many (weakly) non-linear cases (e.g. Emerick, 2016; Evensen et al., 2021; Todaro et al., 2021).

Typically, a constant inflation factor $\alpha_j = J \; \forall j$ is used for simplicity. However, Rafiee & Reynolds (2017) showed that varying inflation factors can be beneficial.

The number of ESMDA iterations has to be defined beforehand, and a convergence study is often required to determine this number. To that end, Le et al. (2016) proposed automatic procedures to adaptively determine the number of iterations and inflation factors during runtime at additional costs.

Algorithm 4 presents the ESMDA routine. It is comparably easy to understand and implement and has therefore gained popularity. In this work, we consider an assimilation window that includes the whole reservoir simulation, thus avoiding interrupting the forward simulation. Further, we use the ESMDA for pure parameter optimisation, further simplifying the implementation.

Algorithm 4 DA routine using the ensemble smoother with multiple data assimilation (ESMDA) based on Emerick & Reynolds (2013) with only one assimilation window.

Input variables
  $\mathcal{M}(\,.\,)$ ▷ Forward model
  $\mathcal{H}(\,.\,)$ ▷ Observation model
  $\mathcal{Z}_0 \in \mathcal{R}^{n \times N}$ ▷ Ensemble of initial DA state vectors
  $d \in \mathcal{R}^{m \times 1}$ ▷ Reference measurements at all time steps
  $R \in \mathcal{R}^{m \times m}$ ▷ Measurement error covariance matrix including all time steps
  α_j ▷ Inflation factors
for $j = 1, ..., J$ **do** ▷ Loop over ESMDA iterations
  $\widetilde{R} = \alpha_j R$ ▷ Inflate measurement error covariance Eq. (4.44)
  for $i = 1, ..., N$ **do** ▷ Loop over ensemble members
    $z_0 = [\mathcal{Z}_0]_i$
    for $k = 1, ..., K$ **do** ▷ Loop over time steps
      $z_i = \mathcal{M}(z_{k-1})$ ▷ Prediction step Eq. (4.38)
      $\bar{y}_k = \mathcal{H}(\, z_k \,)$ ▷ Predicted measurements Eq. (4.39)
    end for
    $[\mathcal{Z}]_i = [\, z_0^T \,,\, z_1^T \,,\, \ldots \,,\, z_K^T]^T$
    $[\mathcal{Y}]_i = [\, \bar{y}_1^T \,,\, \bar{y}_2^T \,,\, \ldots \,,\, \bar{y}_K^T]^T$
  end for
  $\mathcal{Z} = \text{ENKF\_Update}(\mathcal{Z}, \mathcal{Y}, d, \widetilde{R})$ ▷ Update step (Algorithm 1)
end for

4.4.6 Particle filter

Similar to EnKFs, the particle filter (PF) represents the probability distribution of our knowledge about a system by an ensemble of realisations called particles. However, the PF is designed for fully non-linear data assimilation. Moreover, it does not make any assumptions on prior or likelihood and can therefore handle non-Gaussian distributions. They achieve this by adapting the weights of the particles instead of moving them like in the EnKF.

The standard or bootstrap PF was introduced by Gordon et al. (1993). The initial prior knowledge of the system (i.e. at time $k = 0$) is modelled with an

empirical distribution

$$f(x_0) \approx \sum_{n=1}^{N} \frac{1}{N} \delta(x_0 - x_0^n) \tag{4.45}$$

with N particles $\{x_0^n\}_{n=1:N}$, where δ are Dirac functions centred around the particles. In this section, we consider pure state estimation, and consequently, the particles represent the states of the system. However, the method can easily be extended to include model parameters, uncertainty and control inputs.

Generally, the prior knowledge at some time k, possibly depending on reference measurements from previous times $d_{k-1:1} = \{d_{k-1},\ d_{k-2},\ ...,\ d_1\}$, is given as

$$f(x_k|d_{k-1:1}) \approx \sum_{n=1}^{N} w_{k-1}^n \delta(x_k - x_k^n)\ . \tag{4.46}$$

The particle weights w^n are then updated in the analysis step. Suppose we have a reference measurement d_k available; the posterior knowledge of the system at time k following Bayes' theorem is

$$\begin{aligned} f(x_k|d_{k:1}) =& \frac{f(d_k|x_k)}{f(d_k)} f(x_k|d_{k-1:1}) \\ \approx& \sum_{n=1}^{N} w_{k-1}^n \frac{f(d_k|x_k^n)}{f(d_k)} \delta(x_k - x_k^n) = \sum_{n=1}^{N} w_k^n \delta(x_k - x_k^n)\ . \end{aligned} \tag{4.47}$$

As the definition of a PDF requires $\sum_{n=1}^{N} w_k^n = 1$, the weights can be calculated as

$$w_k^n = \frac{w_{k-1}^n f(d_k|x_k^n)}{\sum_j w_{k-1}^j f(d_k|x_k^j)}\ . \tag{4.48}$$

Simply spoken, more weight is put on those particles for which the measurement is likely. Note that by comparing Eq. (4.47) to Eq. (4.45), all particles have the same weight initially, i.e. $w_0^n = 1/N\ \forall n$. In the forward step, the particles are then propagated to the time $k+1$ when new measurement data is available

$$x_{k+1} = \mathcal{M}(x_k) + \upsilon_{k+1}\ , \tag{4.49}$$

where we assume here that $\mathcal{M}(\,.\,)$ is a deterministic function and the model noise υ_k is additive (Eq. (4.1)). We thereby obtain

$$f(x_{k+1}|d_{k:1}) \approx \sum_{n=1}^{N} w_k^n \delta(x_{k+1} - x_{k+1}^n)\ , \tag{4.50}$$

which is identical to Eq. (4.46), and we can continue the next iteration of the DA process from there.

While the standard particle filter can handle non-linear systems with non-Gaussian error statistics in theory, its application in practice is limited as it suffers degeneracy problems. With every DA step, the variation of the weights increases until eventually, one particle has a weight much bigger than the others. To avoid this, a prohibitively large number of particles is required in real-world applications. Several methods have been developed to mitigate the degeneracy problem, such as the sequential importance resampling (SIR) particle filter, localisation techniques and combinations of particle filters with EnKF or variational DA methods; for further information, see e.g. Carrassi et al. (2018) or van Leeuwen et al. (2019).

4.4.7 Localisation and inflation

Ensemble-based methods usually perform very well in small and moderately sized DA problems. However, real-world DA problems often involve estimating a huge number of uncertain states and parameters. Computational resources usually limit the ensemble size; therefore, the prior distribution is likely undersampled. A limited ensemble size restricts the solution space as the posterior ensemble is a linear combination of the prior ensemble (Evensen, 2003). Further, undersampling typically leads to spurious correlations between states and measurements, resulting in unphysical updates and underestimated posterior variance of states far from measurements. In addition, when the number of measurements is much larger than the ensemble size, some information in the measurements cannot be represented by the ensemble and is lost in the update step.

A common strategy is to apply localisation and inflation methods in the update step (for a review, see e.g. Sakov & Bertino, 2011; Chen & Oliver, 2017; Evensen et al., 2022). Localisation dampens the spurious correlations between the states and measurements by element-wise multiplication of a covariance matrix with a damping function (Hamill et al., 2001; Houtekamer & Mitchell, 2001; Chen & Oliver, 2010; Emerick & Reynolds, 2011). It can be applied in state, observation or ensemble space, and the damping function is typically distance-based. Simultaneously, localisation also enables posterior realisations outside the space spanned by the initial ensemble. Local analysis, a related method, divides the states into subsets and updates them independently (Haugen & Evensen, 2002; Evensen, 2003). For each subset, we can individually select which measurements to include in the update step. While covariance localisation and local analysis are typically distance-based, adaptive localisation can be used when long-ranging correlations exist naturally in a system (Luo & Bhakta, 2020). Inflation, on the other hand, restores the correct ensemble spread by multiplying the ensemble approximation of the state covariance with a scalar (Anderson & Anderson, 1999). It is often necessary to avoid filter divergence when only a small ensemble size can be used.

4.5 DA in fractured porous media

A vast number of studies exist that apply ensemble-based DA to porous media. Many studies consider pure parameter estimation where, most typically, the matrix permeability is estimated, while other studies also include flow and transport fields in the DA state vector (e.g. Nævdal et al., 2005; Chen & Zhang, 2006; Skjervheim et al., 2007; Hendricks Franssen & Kinzelbach, 2008; Li et al., 2012; Vogt et al., 2012). Some studies have developed specific methods for characterising channelised reservoirs (Jafarpour & McLaughlin, 2008; Chang et al., 2010; Zhou et al., 2011).

Several studies have applied various forms of ensemble-based DA to fractured porous media, targeting different objectives and aspects of fracture modelling. The following review, which is based on the introductions in Liem & Jenny (2020) and Liem et al. (2023b, Preprint), focuses thereby on studies that directly update fracture properties such as location, orientation, aperture, permeability or porosity as opposed to upscaled or averaged fields.

Fracture aperture and the related permeability are essential parameters for flow and transport and are usually associated with considerable uncertainty. Thus, estimating fracture aperture is an important objective. As apertures vary considerably among fractures (Barton et al., 1995; Baghbanan & Jing, 2008; Barton & Quadros, 2015; Zhang et al., 2021b), estimating an individual aperture value for each fracture is desirable. Some studies have used relatively simple, unconditional distributions to model the apertures (Zhe et al., 2016; Liem & Jenny, 2020; Liu et al., 2022). Others set the apertures proportional to the fracture length (Zhang et al., 2021a). However, these models may not accurately represent the complex relationship between aperture values and stress state, displacement history and fracture parameters such as orientation, length, and surface roughness (Section 2.2.3). Seabra et al. (2023) include those complex relations, albeit without considering shear displacement. They calculate fracture apertures as a function of effective normal stress obtained from a geomechanical simulation and subsequently reduce the uncertainty in the global model parameters with DA. In Wu et al. (2021), the authors follow an altogether different approach and model aperture variations within the fracture plane of a single fracture.

The studies above assume a known fracture geometry, significantly simplifying the DA problem. Considering uncertainty in the fracture geometry is challenging for several reasons. Obtaining physically meaningful prior realisations that include geomechanical knowledge, such as stress states or rock properties, is not trivial. Often, studies use prior ensembles based on relatively simple distributions that incorporate only little geomechanical knowledge, if any. Even if the prior geometry is physically meaningful, there is no guarantee that the updated posterior geometry is also. Generally, arbitrary small distances or angles between two fractures can arise in the update step. Further, the updated fracture geometry needs to be meshed automatically, where using a non-conforming mesh, such as

in EDFM, is beneficial. Additional challenges arise when the fracture number is also considered as an uncertain parameter.

Several studies treat fracture location as an uncertain parameter. Liu et al. (2018) directly update fracture coordinates with EnKF. When the number of fractures is unknown, the fractures can be parametrised with a representing node system where a level set function indicates whether a fracture is present at the corresponding node (Ping & Zhang, 2013; Ping et al., 2017; Chai et al., 2018). A similar approach parametrises the fractures with the Hough transform, where each local maximum in the Hough field corresponds to a fracture (Lu & Zhang, 2015; Yao et al., 2018, 2019). In addition to fracture length, these studies often consider fracture orientation and length as uncertain parameters.

In the majority of the studies referenced above, the analysis is limited to a relatively small number of fractures, typically involving ten or fewer, and conducted in 2D. Extending these findings to more complex fracture networks and the transition to comprehensive 3D models remains an area for further exploration. Except for Zhe et al. (2016), these studies consider scenarios where all fractures are present from the beginning of the reservoir simulation, and their properties do not change over time. Including dynamic fracture formation and changes in fracture properties with, for example, fluid pressure presents an interesting area of research.

In the following chapters, we focus on the fracture apertures as the only uncertain model parameter. Further, we assume that we know the initial state of the reservoir (i.e. pressure and concentration fields) exactly and that the forward simulation is error-free.

5 Influence of Measurement Strategies and Matrix Permeability on Fracture Estimation

Some parts of this chapter are loosely based on the conference proceedings "Two-Stage Ensemble Kalman Filter Approach for Data Assimilation Applied to Flow in Fractured Media" (Liem & Jenny, 2020). However, the results presented here include improved and extended scenarios and stem from an enhanced DA framework. All data, figures, and text in this chapter are newly created, and no content has been copied from Liem & Jenny (2020) unless stated otherwise.

5.1 Introduction

Reservoir stimulation aims to enhance reservoir permeability and heat exchange in enhanced geothermal systems (EGS) (Jia et al., 2022). Various stimulation techniques, including hydraulic, chemical and thermal approaches are available, with hydraulic stimulation being the most commonly employed. In this process, new fractures are created (hydraulic fracturing), and pre-existing natural ones are reactivated (hydro-shearing). Hydraulic reservoir stimulation continues for an extended period, as illustrated by Häring et al. (2008) for Basel 1.

In this conceptual study, we consider fractured porous media where the individual fractures appear one after the other. Based on flow and transport data, we estimate fracture aperture and length with ESMDA. In this work, we first study how intermediate measurements during the reservoir stimulation process affect the estimation of the fracture apertures. Secondly, we demonstrate that matrix permeability has a huge effect on these results, as the sensitivity of the apertures on the measurements decreases for high and low matrix permeability values. Lastly, we repeat those studies and estimate fracture length instead of aperture.

5.2 Method

5.2.1 Fracture geometry

In this study, we use the relatively simple synthetic two-dimensional fracture network presented in Section 3.3.2 and taken from Liem & Jenny (2020). The fracture network consists of two sets; the first set contains 9 fractures oriented in x-direction, and the second set contains 13 fractures oriented in y-direction. We

assume that the fractures appear one after the other, where Fig. 5.1 indicates the sequence of appearance.

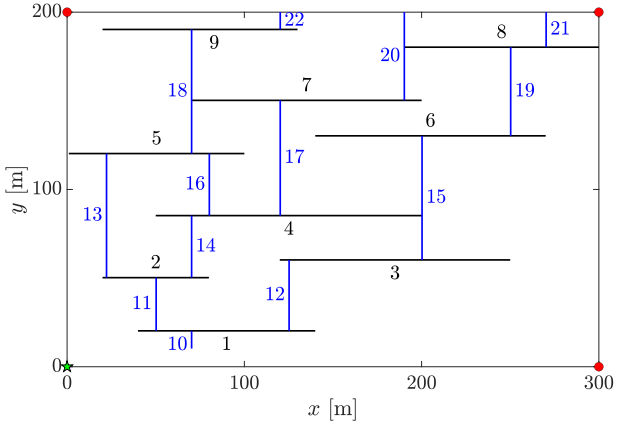

Figure 5.1: Fracture network with 22 fractures taken from Liem & Jenny (2020). The numbers indicate the sequence in which the fractures appear. The green star marks the position of the injector well, and the red circles mark the position of the producers.

This study consists of three parts. In the first two parts, we assume that the location, orientation, and length of each fracture are known *a priori*. The hydraulic fracture apertures, which are assumed to be constant over the length of each fracture, are the only uncertain parameters in those parts. In the third part, the fracture lengths, instead of the apertures, are considered uncertain. We thereby assume fixed and known midpoints of the fractures.

We sample the prior ensemble from a beta distribution that approximates a normal distribution with mean $\mu = 0.5$ and standard deviation $\sigma = 1/6$ (Fig. 5.2a). These two distributions share the same mean and standard deviation. However, the beta distribution is bounded and, as such, does not produce outliers that might reach unphysical levels. We scale the beta distribution and sample the logarithm of the apertures (Fig. 5.2b) and relative fracture length (Fig. 5.2c). We thereby sample each fracture parameter in each realisation independently. The resulting PDF for the fracture apertures is shown in Fig. 5.2d. For the synthetic reference realisation, we set the apertures of all fractures to 1×10^{-3} m and use the original length of the fractures as depicted in Fig. 5.1.

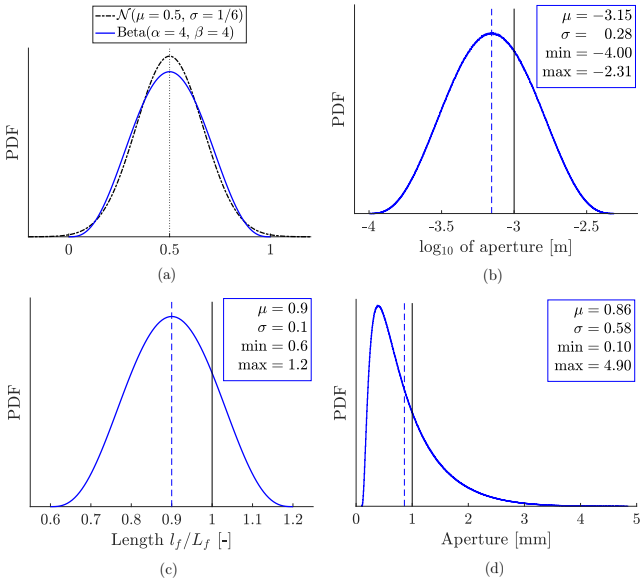

Figure 5.2: Probability density functions (PDFs) for sampling fracture parameters. We approximate a normal distribution with a beta distribution (a) and scale it to obtain PDFs for log-aperture (b) and relative fracture length (c). The resulting PDF of the apertures is shown in (d). The dashed blue lines in (b–d) indicate the ensemble mean, and the solid black line represents the reference value.

5.2.2 Forward simulation

We consider single-phase flow in a thin layer of fractured porous medium embedded between two impermeable layers, allowing for a two-dimensional analysis. We assume the fractured layer is horizontal, hence neglecting gravitational effects. The matrix possesses a uniform and isotropic permeability k_m and a uniform porosity ϕ_m, and we derive the fracture permeability assuming plane Poiseuille flow between two parallel plates, as expressed in Eq. (2.31). Table 5.1 lists the parameters of the forward simulation.

We discretise the domain with a Cartesian grid whose grid cells are much larger than the apertures, thus requiring upscaling of the fractures. We follow the upscaling process outlined in Section 2.4.3 and determine the anisotropic upscaled permeability tensor using the analytical equations derived by Kasap & Lake (1990). Additionally, we compute the upscaled porosity through volume averaging.

Physical parameters	
Matrix permeability	$k_m = 1 \times 10^{-14}\,\mathrm{m}^2$
Matrix porosity	$\phi_m = 0.15$
Fracture permeability	$k_f = a_f^2/12$
Fracture porosity	$\phi_f = 1.0$
Fluid viscosity	$\mu = 1 \times 10^{-3}\,\mathrm{Pa\,s}$
Boundary & initial conditions	
Pressure at producers	$p_{\mathrm{out}} = 1 \times 10^7\,\mathrm{Pa}$
Volume flow rate at injector	$\dot{Q}_{\mathrm{in}} = 5 \times 10^{-3}\,\mathrm{m}^3/\mathrm{s}$
Tracer concentration at injector	$c_{\mathrm{in}} = 1.0$ for $t > 0$
Initial tracer concentration	$c_{\mathrm{init}}(t = 0) = 0$ everywhere
Spatial discretisation	
Size of domain	$300 \times 200 \times 1\,\mathrm{m}^3$
Number of grid cells	$600 \times 400 \times 1 = 240000$
Size of grid cells	$0.5 \times 0.5 \times 1\,\mathrm{m}^3$
Temporal discretisation with ACTI (see Section 3.2.2)	
Maximal time step for ACTI	$\Delta t_{\max} = 3\,\mathrm{h}$
CFL criterion	$CFL_{\max} = 0.5$
Flux reconstruction scheme	MUSCL-AIR
Slope limiter	Koren

Table 5.1: Simulation parameters

Fluid is injected into the domain through the lower left corner and produced from all other corners. Whenever a new fracture appears, we calculate the steady-state pressure field using the elliptic pressure equation (Eq. (2.9)), which we discretise with a finite volume method (FVM) and solve directly. The injector and the producers are represented as point sources with a specified injection rate and outlet pressure, respectively, while no-flow conditions are enforced at the domain boundary. We monitor the pressure at the injector and the flow rates at the three producers.

In addition, we perform two tracer tests, one after the nine fractures from the first set have appeared and one at the very end with all 22 fractures. Initially, the tracer concentration is zero everywhere. At time t_0, we begin injecting a tracer with concentration $c_{\mathrm{in}} = 1$ into the inlet well. The tracer moves through the domain according to the scalar advection equation (Eq. (2.14)), thus neglecting diffusion. We solve this transport problem using ACTI with the MUSCL-AIR scheme introduced in Section 3.2.2. We monitor the tracer breakthrough curves at the producers and measure the time it takes for the tracer concentration to reach 0.1 and 0.9.

5.2.3 Measurement scenarios

As part of this study, we investigate how measurement data affect the outcome of a DA framework. We thereby compare five measurement scenarios (Table 5.2). In scenario 1, we use flow and transport measurements obtained once all 22 fractures have appeared. In scenario 2, we additionally use flow and transport measurements after all nine fractures of the first set have appeared. Scenario 3 uses only flow measurements but obtains them after each fracture appears. In contrast, Scenario 4 uses only transport measurements from the tracer tests after 9 and 22 fractures have appeared. Finally, scenario 5 uses all available measurements.

Scenario	F 1–8	F 9	T 9	F 10–21	F 22	T 22	Total
1					x	x	10
2		x	x		x	x	20
3	x	x		x	x		88
4			x			x	12
5	x	x	x	x	x	x	100

Table 5.2: Measurement scenarios: Flow (F) and transport (T) measurements with the accompanied number indicating after which fracture appearance the corresponding measurement is obtained. Flow measurements contain inlet pressure and flow rates at the three producers. Transport measurements include the times when the concentration reaches 0.1 and 0.9 at each producer. The last column summarises the total number of measurements used in each scenario.

5.2.4 Data assimilation

In this study, we estimate fracture parameters, namely their aperture and length, using the ensemble smoother with multiple data assimilation (ESMDA) as presented in Section 4.4.5. The DA state vector in the first two parts of this study contains the logarithm of all 22 fracture apertures

$$z_j = \left[\log_{10}(a_1^j)\,,\, \log_{10}(a_2^j)\,,\, \ldots\,,\, \log_{10}(a_{22}^j) \right]^T \,, \tag{5.1}$$

and in the third part the fracture length

$$z_j = \left[l_1^j\,,\, l_2^j\,,\, \ldots\,,\, l_{22}^j \right]^T \,. \tag{5.2}$$

Here, j denotes the j-th realisation of an ensemble or the reference realisation.

We run a separate simulation without any fractures and use it to scale the measurements as

$$\tilde{p} = \frac{p}{p_0} \quad , \quad \tilde{\dot{Q}}^{(i)} = \frac{\dot{Q}^{(i)}}{\dot{Q}_0^{(i)}} \quad \text{, and} \quad \tilde{t}^{(i)} = \frac{t^{(i)}}{t_0^{(i)}} \, . \tag{5.3}$$

Here, the subscript 0 denotes the measurement without any fractures and the superscript (i) the measurement location. We then collect the scaled measurements in the measurement vector y according to the scenarios listed in Table 5.2. Further, we assume uncorrelated measurement errors and use a diagonal measurement error covariance matrix. The entries corresponding to pressure and flow rate measurements are set to 1×10^{-6}, and the ones for the arrival time measurements to 1×10^{-4}.

In this work, we use an ensemble size of 500 realisations. The relatively large ensemble size compared to the low number of estimated parameters is required due to the number of measurements in scenario 5. A smaller ensemble size cannot represent the information of all 100 measurements (see also Section 4.4.7). Further, we found that 4 ESMDA iterations are sufficient for this study. We run our DA framework with several prior ensembles sampled with different seeds.

We evaluate the performance of the DA framework with the root-mean-square mean error (RMS-ME) and the mean of the root-mean-square errors (M-RMSE), i.e.,

$$\text{RMS-ME}_\xi = \frac{1}{N_\xi} \sum_{i=1}^{N_\xi} \sqrt{\left[\left(\frac{1}{N_E} \sum_{j=1}^{N_E} \xi_i^{(j)} \right) - \xi_i^{(\text{ref})} \right]^2} \text{, and} \tag{5.4}$$

$$\text{M-RMSE}_\xi = \frac{1}{N_\xi} \sum_{i=1}^{N_\xi} \sqrt{\frac{1}{N_E} \sum_{j=1}^{N_E} \left(\xi_i^{(j)} - \xi_i^{(\text{ref})} \right)^2} \, . \tag{5.5}$$

In these equations, ξ can represent either the DA state vector z, the measurement vector y, or a subset thereof. Here, $\xi_i^{(j)}$ denotes the i-th entry in the corresponding vector of the j-th realisation, and N_ξ refers to the length of that vector. Note that the RMS-ME is the root-mean-square error of the ensemble mean. While the RMS-ME purely assesses the accuracy of an ensemble prediction, the M-RMSE reflects a combination of both accuracy and precision.

5.3 Results

5.3.1 Reference realisation and prior ensemble

We first present the flow and transport behaviour of the synthetic reference realisation. Fig. 5.3 shows the steady-state pressure and flow fields of the reference realisation after the 9 fractures from set one and all 22 fractures have appeared. The pressure around the injector is extremely high due to the point source, and the fractures greatly influence the streamlines. Fig. 5.4 shows the evolution of the tracer concentration through these steady-state flow fields. The fractures advance the tracer much faster than the matrix due to the focused flow. This results in flatter breakthrough curves, as low concentrations of the tracer reach the producers earlier while high concentrations arrive later.

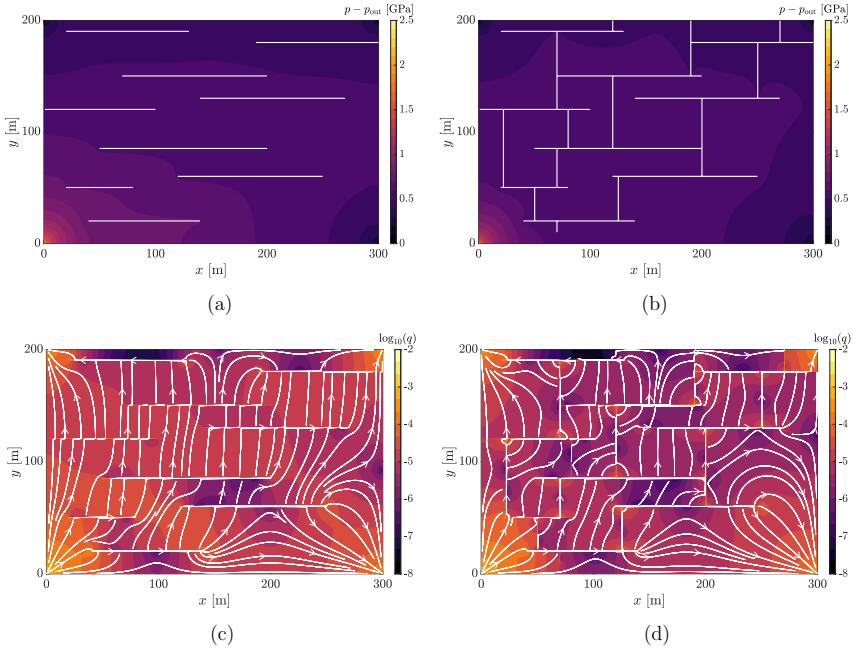

Figure 5.3: Pressure field and fractures (a, b) and logarithm of volumetric flux density with streamlines (c, d) after 9 fractures (left) and 22 fractures (right) for the reference realisation. The line thickness of the fractures in (a, b) indicates their apertures, exaggerated by a factor of 1×10^3.

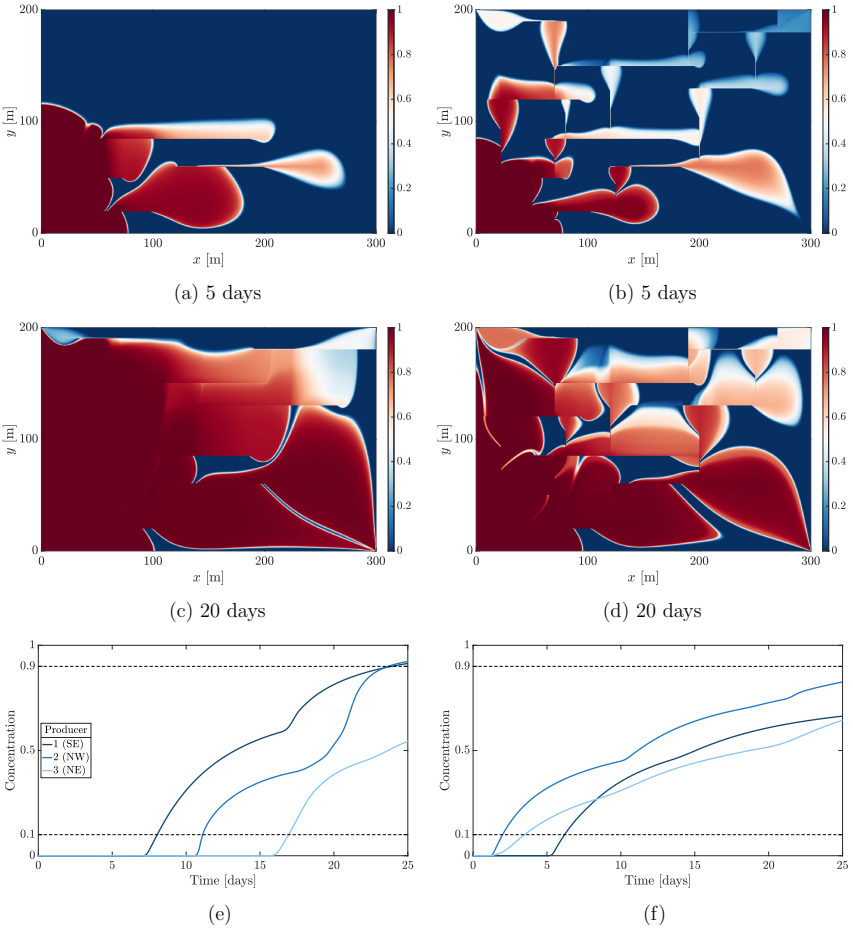

(a) 5 days (b) 5 days

(c) 20 days (d) 20 days

(e) (f)

Figure 5.4: Tracer concentration after 5 days (a, b) and 20 days (c, d) and breakthrough curves at the three producers (e, f) after 9 fractures (left) and 22 fractures (right) for the reference realisation.

We sample 500 realisations of the fracture apertures for the prior ensemble as described in Fig. 5.2. Fig. 5.5 presents the fracture apertures of the first three realisations and corresponding pressure and tracer concentration fields. While the variation in the fracture apertures is clearly visible, it is less apparent in the pressure and concentration fields.

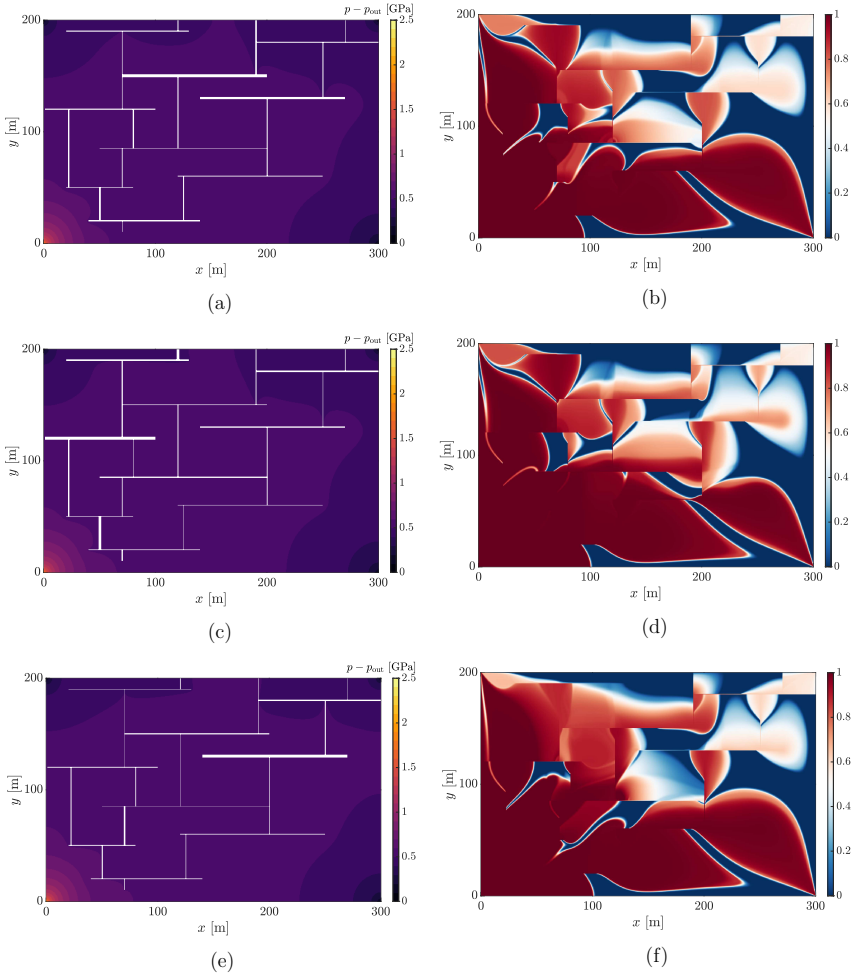

Figure 5.5: Pressure field and fractures (left) and tracer concentration after 20 days (right) after all 22 fractures have appeared for the first three realisations of the prior ensemble. The line thickness of the fractures indicates their apertures, exaggerated by a factor of 1×10^3.

5.3.2 Measurement scenarios

We now compare the posterior ensembles from the different measurement scenarios. Fig. 5.6 shows the RMS-ME and the M-RMSE for the DA state vector containing the logarithm of the fracture apertures. Overall, scenarios 3 and 5 achieve the biggest error reduction. Both of them incorporate flow data obtained after the creation of every fracture. The additional transport data in scenario 5 provides only a minor improvement in the M-RMSE and even a slightly worse ensemble mean. Comparing scenarios 1 to 3, we see that both errors are steadily reduced with an increasing number of flow measurements. Scenario 4, which relies only on transport data, has the largest errors.

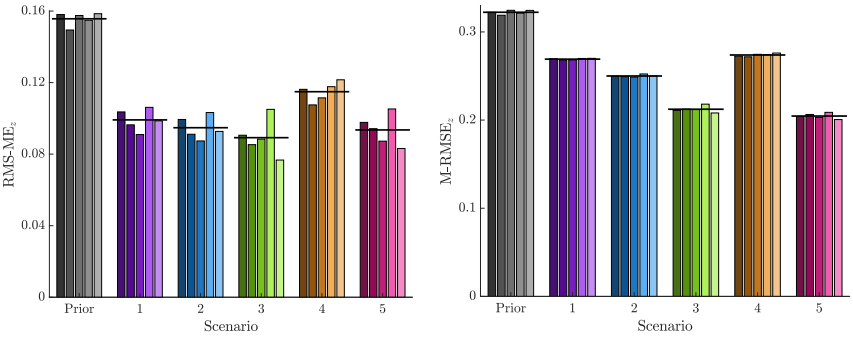

(a) Root-mean-square error of ensemble mean

(b) Mean root-mean-square error

Figure 5.6: RMS-ME (a) and M-RMSE (b) of the DA state vector consisting of log-apertures for the prior ensemble and different measurement scenarios. The horizontal black lines indicate the mean over 5 simulation runs with different prior ensembles.

The measurement scenarios incorporate different types and numbers of measurements, rendering direct comparison of the measurement vector errors impractical. Instead, we assess the M-RMSE of the individual quantities, i.e. the inlet pressure and outlet flow rates after each fracture appearance and the arrival time measurement for the two tracer tests, regardless of whether these quantities are included in the measurement vector for a given scenario (Fig. 5.7). Overall, the quantities show similar trends, mirroring the results observed for the DA state vector (Fig. 5.6). The figures for the RMS-ME are qualitatively the same and are thus omitted here. An interesting finding is that scenario 4 achieves better matching of arrival times compared to scenario 1, yet scenario 3 outperforms both despite not incorporating any arrival time measurements in the ESMDA updates.

Next, we analyse the results from measurement scenario 5 in more detail. Fig. 5.8 illustrates the fracture apertures of the first three posterior realisations

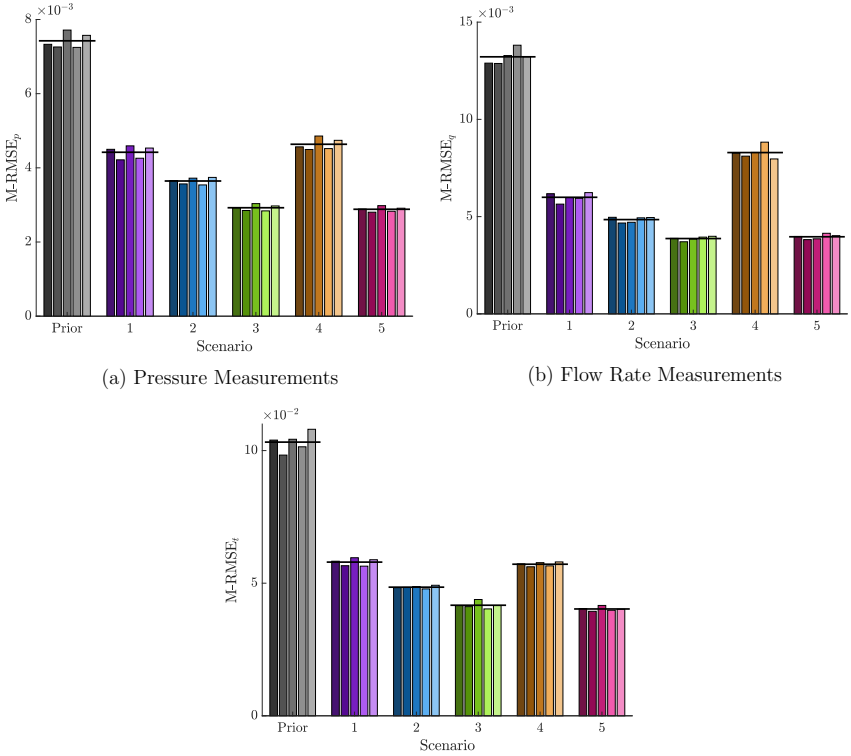

(a) Pressure Measurements

(b) Flow Rate Measurements

(c) Arrival Time Measurements

Figure 5.7: Mean root-mean-square error of the scaled measurements for the prior ensemble and different measurement scenarios. The horizontal black lines indicate the mean over 5 simulation runs with different prior ensembles.

alongside corresponding pressure and tracer concentration fields. A comparison with Figs. 5.3 to 5.5 reveals a clear improvement in the fracture apertures, particularly noticeable for longer fractures such as fracture 4, the longest one in the x-direction. However, some shorter fractures, like fracture 21 in the top right corner, show no improvement.

While the improvements in the apertures are readily visible, the ones in the pressure and concentration fields are less apparent. To investigate this further, we present the pressure at the injector during fracture creation and the tracer breakthrough curves from the upper left producer with all 22 fractures present

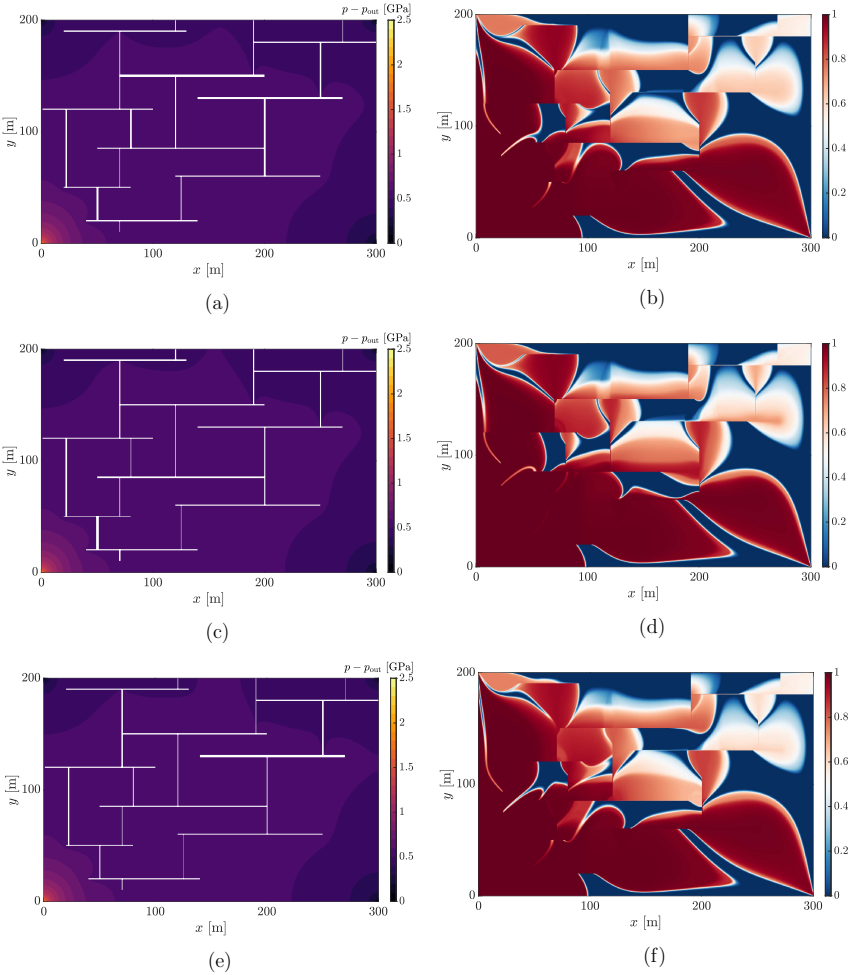

Figure 5.8: Pressure field and fractures (left) and tracer concentration after 20 days (right) after all 22 fractures have appeared for the first three realisations of the posterior ensemble with measurement scenario 5. The line thickness of the fractures indicates their apertures, exaggerated by a factor of 1×10^3.

for both the prior and posterior ensemble in Fig. 5.9. The prior ensemble overestimates the pressure at the injector due to the underestimation of the fracture

apertures (see Fig. 5.2). The posterior ensemble resembles the reference values much better, although it still shows a bias towards higher pressures. The posterior ensemble also shows good improvement in the breakthrough curves, especially for concentrations 0.1 and 0.9, which are used in the ESMDA updates. However, some distinct features of the reference breakthrough curve between those measurements are not fully captured.

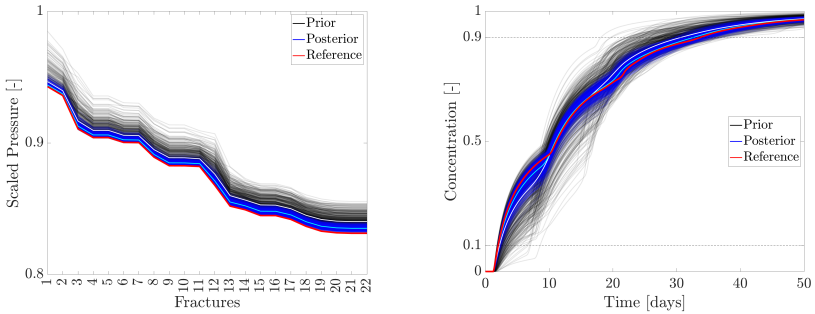

(a) (b)

Figure 5.9: Pressure at the injector over the fracture creation (a) and the tracer breakthrough curve from the upper left producer after all 22 fractures have appeared (b). The reference is shown in red, the prior ensemble in black, and the posterior ensemble with measurement scenario 5 in blue. The white and cyan lines mark prior and posterior ensemble means, respectively.

5.3.3 Matrix permeability

Further, we investigate the influence of matrix permeability on the DA results, focussing on measurement scenario 5 for this analysis. When matrix permeability is exceptionally low, the flow field is primarily dictated by the fracture connectivity and distances between fractures and wells. Conversely, when matrix permeability is very high, fractures have a minimal influence on the flow field as much of the flow occurs within the matrix. As a result, we expect the sensitivity of measurements on the fracture apertures to vary based on matrix permeability.

This expectation is verified in Fig. 5.10, which shows the inlet pressure and the flow rates at one producer for different aperture values of fracture 1, the only fracture present in this instance. For a matrix permeability of $1 \times 10^{-14}\,\mathrm{m}^2$ (as used in the previous section), pressure and flow data become stagnant for apertures exceeding 1 mm. On the other hand, with a matrix permeability of $1 \times 10^{-11}\,\mathrm{m}^2$,

apertures below 1 mm have only negligible influence. Extreme matrix permeability values show very low sensitivity across the entire aperture range considered here.

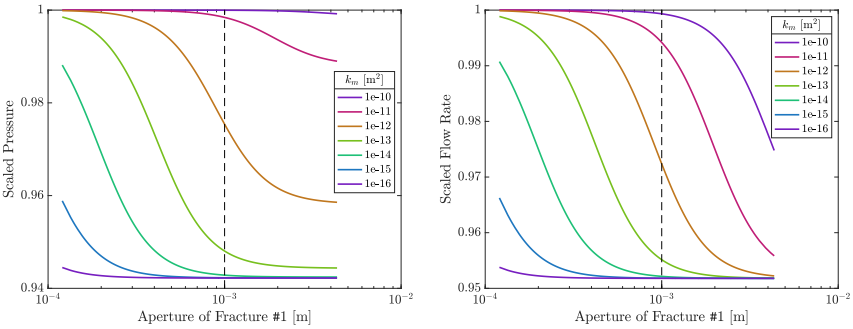

(a) (b)

Figure 5.10: Scaled inlet pressure (a) and flow rate at top left corner producer (b) after the first fracture has appeared as a function of its aperture.

As a result, the accuracy of the DA state vector and measurements is influenced by the matrix permeability (Fig. 5.11). We obtain the best aperture estimations with a matrix permeability of $1 \times 10^{-12}\,\mathrm{m}^2$. For extreme matrix permeabilities, the errors in the apertures are only slightly reduced compared to the prior and even increased for the RMS-ME in the case with $k_m = 1 \times 10^{-10}\,\mathrm{m}^2$. For intermediate matrix permeabilities, measurements are highly sensitive to aperture values, leading to substantial prior measurement errors. In the corresponding posterior ensembles, these errors are notably reduced. Conversely, cases with extreme matrix permeabilities have low measurement errors in the prior and posterior.

5.3.4 Estimating fracture length

We now repeat the study for uncertain fracture lengths. Overall, the performance of the five measurement scenarios is similar to that of the fracture aperture estimation presented above. The ensemble mean of scenarios 3 and 5 matches the reference very well, whereas the other three measurement scenarios show moderate error reductions (Fig. 5.12). Corresponding results for the measurements are depicted in Fig. 5.13. In the prior realisations, fractures are less interconnected due to the intentional underestimation of the fracture length, resulting in substantial errors in pressure measurements. The posterior ensemble effectively retrieves these connections, thus drastically reducing the errors. Notably, while the posterior of scenario 4 provides a good match of the arrival time measurements, it exhibits significant errors in flow rate measurements.

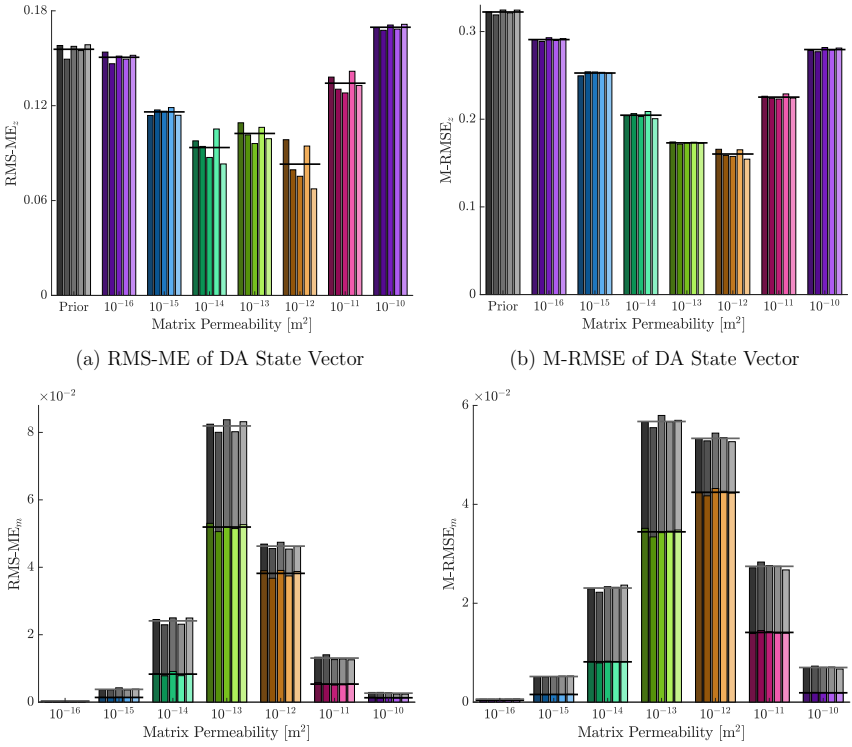

(a) RMS-ME of DA State Vector

(b) M-RMSE of DA State Vector

(c) RMS-ME of Measurement Vector

(d) M-RMSE of Measurement Vector

Figure 5.11: RMS-ME (left) and M-RMSE (right) of the DA state vector consisting of log-apertures (a, b) and measurement vector (c, d) for different matrix permeabilities. Note that the prior DA state vector is the same for all matrix permeabilities while the prior measurement vector differs. The horizontal black lines indicate the mean over 5 simulation runs with different prior ensembles. Results are presented for measurement scenario 5.

The effect of matrix permeability on length estimation differs from its impact on aperture estimation. For matrix permeabilities of $1 \times 10^{-13}\,\mathrm{m}^2$ and lower, we obtain a good estimation of fracture length and achieve a considerable reduction of the measurement errors (Fig. 5.14). The results show minimal improvements for high matrix permeabilities, both in state and measurement vector.

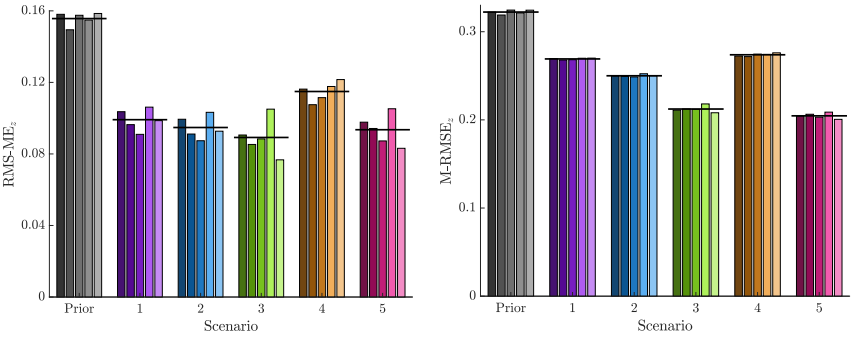

(a) Root-mean-square error of ensemble mean

(b) Mean root-mean-square error

Figure 5.12: Errors of the DA state vector consisting of fracture lengths for the prior ensemble and different measurement scenarios. The horizontal black lines indicate the mean over 5 simulation runs with different prior ensembles.

5.4 Discussion

In this work, we study the influence of measurement strategies and matrix permeabilities on the estimation of fracture properties, specifically fracture aperture and length. Incorporating intermediate measurements during fracture creation in reservoir stimulation proves beneficial for both of these properties, a result that aligns with the general principle that more data leads to better estimations.

It is noteworthy that arrival time measurements exhibit only a small impact compared to pressure and flow rate measurements. One possible explanation could be attributed to the chosen boundary conditions. By imposing a fixed injection rate, the influence of the apertures on the breakthrough curves is diminished. We anticipate that arrival time measurements may have a much higher impact when pressure boundary conditions are applied at both inlet and outlets. Additionally, mixing of the tracer within the fracture cells potentially leads to some loss of information about fractures. In Section 3.3.3, we avoid mixing by resolving the aperture of a single fracture with an extremely fine mesh. However, such a fine mesh is impractical in the presented network, let alone in larger networks, and some degree of mixing occurs *in situ* regardless. Moreover, the reference breakthrough curve in Fig. 5.9 shows distinct features not matched by the posterior ensemble, suggesting that the breakthrough curves contain additional information that could be harnessed by collecting more than two measurements per curve. Finally, we arbitrarily choose the values in this study's measurement error covariance matrix. We expect lower entries for the arrival time measurements to increase their relative importance compared to flow measurements.

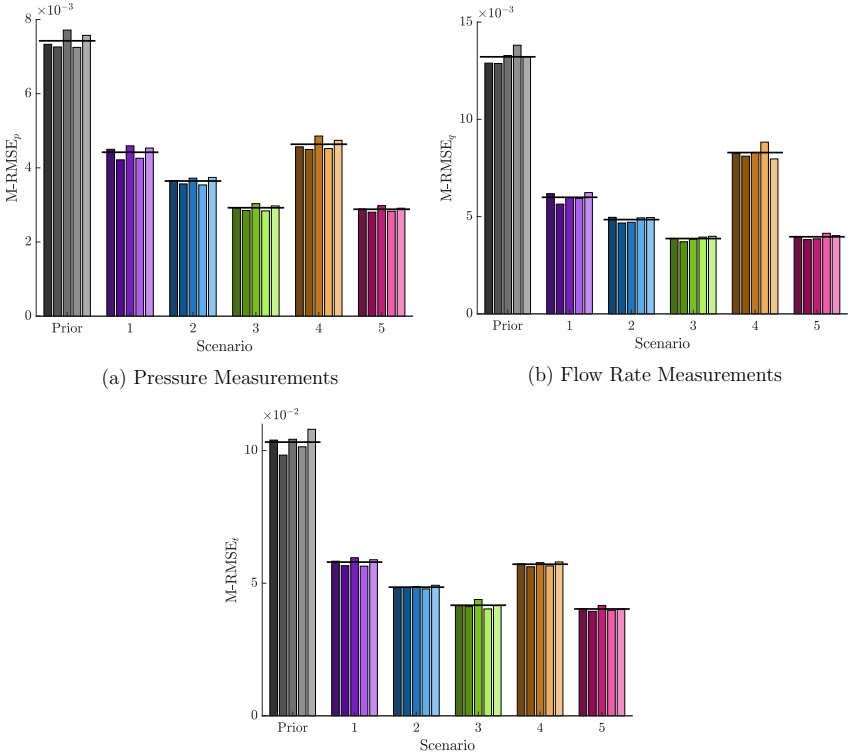

(a) Pressure Measurements

(b) Flow Rate Measurements

(c) Arrival Time Measurements

Figure 5.13: M-RMSE of the scaled measurements for the prior ensemble and different measurement scenarios when estimating fracture lengths. The horizontal black lines indicate the mean over 5 simulation runs with different prior ensembles.

The matrix permeability has a decisive influence on the estimation of fracture properties. In instances where the ratio of fracture to matrix permeability is low (i.e., for very high matrix permeabilities), most flow occurs within the matrix, and the fractures play a negligible role. Consequently, both aperture and length estimations perform poorly under such conditions. Conversely, high fracture-to-matrix permeability ratios (i.e., very low matrix permeabilities) lead to flow being dictated by fracture interconnectivity and their proximity to the wells. This condition resembles an infinite transmissivity fracture, where the flow through a fracture is no longer sensitive to aperture variations (Phillips, 1991). Therefore,

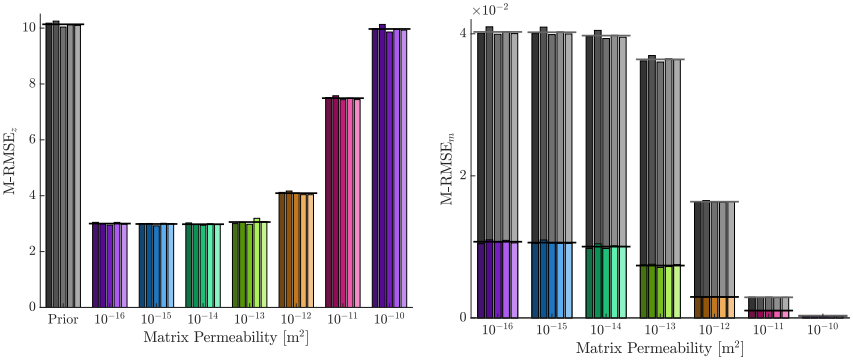

(a) DA State Vector

(b) Measurement Vector

Figure 5.14: M-RMSE of the DA state vector consisting of fracture length (a) and measurement vector (b) for different matrix permeabilities. Note that the prior DA state vector is the same for all matrix permeabilities while the prior measurement vector differs. The horizontal black lines indicate the mean over 5 simulation runs with different prior ensembles. Results are presented for measurement scenario 5. The results for the RMS-ME are qualitatively similar.

length estimation performs well for low matrix permeabilities, whereas aperture estimation struggles. In an intermediate matrix permeability range of 1×10^{-14} to $1 \times 10^{-13}\,\mathrm{m}^2$, the condition resembles that of finite conductivity fractures, resulting in satisfactory aperture and length estimates in our study.

We plan to expand our scope in future studies by incorporating additional aspects of fracture properties estimation. A natural progression from this work involves combining both aperture and length estimation. Moreover, our current analysis focuses on small uncertainties in fracture length, thereby simplifying the DA problem. Future investigations should consider larger uncertainties in fracture length within the prior ensemble. Additionally, we intend to explore uncertainties associated with midpoints and orientation of fractures, albeit this requires a more versatile reservoir simulator capable of handling inclined fractures.

Our current study uses a simple synthetic fracture geometry with a limited number of fractures. Future research should move towards realistic fracture geometries with a greater number of fractures. We expect the main findings about measurement strategies and matrix permeability to still hold true in more complex and realistic fracture patterns.

In this study, we model reservoir stimulation as a sequential process where fractures appear one after another, and once a fracture is created, they remain

unchanged throughout the stimulation period. However, in reality, reservoir stimulation is a dynamic process where fractures can grow over time. It is crucial to incorporate this dynamic aspect into the framework. In this work, we estimate the current state of the reservoir. Ultimately, the goal is to predict future reservoir behaviour using past and present data.

6 Prior with Far-Field Stress Approximation for Ensemble-Based Data Assimilation in Naturally Fractured Reservoirs

This chapter is adapted from the manuscript "Prior with far-field stress approximation for ensemble-based data assimilation in naturally fractured reservoirs" (Liem et al., 2023b, Preprint). Preliminary work of this study has been presented in the conference paper "Estimation of fracture aperture in naturally fractured reservoirs using an ensemble smoother with multiple data assimilation" (Liem et al., 2022b), some of which is recreated in Section 6.5.3.

6.1 Introduction

Many rocks involved in subsurface applications contain complex fracture geometries with large numbers of fractures. Therefore, it is essential that DA approaches capable of dealing with such scenarios are developed. As discussed in Section 4.5, many studies that estimate fracture aperture using ensemble-based DA, including the one presented in Chapter 5, use a small number of fractures. Additionally, aperture typically depends only on a few underlying uncertain parameters in studies considering a moderate number of fractures. Ensemble-based DA usually performs well under such conditions; however, it becomes more challenging when considering a large number of fractures, each with an individual aperture.

The performance of ensemble-based DA strongly depends on the quality of the prior ensemble. Computational resources usually limit the ensemble size, and therefore, the prior distribution is likely undersampled. This restricts the solution space as posterior realisations are weighted combinations of the prior realisations (Evensen, 2003), and undersampling can lead to spurious correlations. Those issues are by no means unique to DA applied to fractured reservoirs but arise in any other application where a huge number of parameters is represented by a limited ensemble size, such as in meteorology, oceanography, or groundwater flows. A common strategy is to apply localisation and inflation methods in the update step, as discussed in Section 4.4.7.

In this work, we pursue a different (and possibly complementary) approach to improving the prior ensemble by incorporating additional physical knowledge. This approach is rarely used in studies that estimate fracture aperture using ensemble-based DA as they typically ignore the complex relationship between

aperture values and stress state, displacement history and fracture parameters. A notable exception is the work of Seabra et al. (2023), which includes those complex relations, albeit without shear displacement.

We consider a situation where the fracture apertures are predominantly created by shearing driven by the tectonic far-field stresses. Toolkits with geomechanical capabilities such as ABAQUS (Smith, 2009; Agheshlui et al., 2018), COMSOL (Multiphysics, 2013), DARTS (Wang et al., 2020; Boersma et al., 2021), ICGT (Thomas et al., 2020; Paluszny et al., 2020), MRST (Ucar et al., 2018; Lie & Møyner, 2021), OpenCSMP (Pezzulli et al., 2022a,b), or XFVM (Deb & Jenny, 2017a,b) can been used to calculate shear displacement and fracture apertures for this scenario. However, it would be computationally expensive to generate a whole ensemble of geomechanical realisations that are needed as priors for a DA framework, especially when considering a statistically representative number of fractures. A purely stochastic approach on the other hand is unlikely to include all available physical knowledge and cannot represent the complex relationship between apertures and other modal parameters.

We therefore look for a method that produces physically meaningful prior realisations at a reduced computational cost. For this, we build upon existing proxy models (Milliotte et al., 2018; Agheshlui et al., 2019; Wang et al., 2023) and propose a method based on far-field stress approximation (FFSA). FFSA projects the tectonic far-field stresses onto the fracture planes and estimates the shear displacements based on linear elastic theory. Thus, we do not need to solve differential equations, which makes the method computationally attractive. We account for the errors introduced by those approximations by additional uncertainty in a model parameter. We combine the FFSA with the constitutive relations of Barton and Bandis (Barton & Choubey, 1977; Barton, 1982; Bandis et al., 1983; Barton et al., 1985; Lei & Barton, 2022) and integrate it into our ESMDA framework. We use flow and transport data to improve the estimation of the fracture apertures.

Compared to a preliminary version of this approach (Liem et al., 2022b), this work refines and extends the method and presents more extensive and practically relevant results. In particular, we obtain the synthetic reference flow and transport data from a realisation generated with a geomechanical reservoir simulator, and we compare the performance of our DA framework when using prior ensembles generated with the FFSA to two stochastically generated prior ensembles.

This chapter of the thesis is organised as follows: Section 6.2 introduces our data assimilation framework including the FFSA for generating prior ensembles. In Section 6.3, we discuss the fracture geometry, and in Section 6.4, the model parameters, some of which are assumed to be uncertain. The results of this study, which are presented in Section 6.5 and discussed in depth in Section 6.6, show that reasonable prior ensemble realisations can be obtained with FFSA. Ensembles generated with FFSA outperform the ones from two naïve stochastic approaches in our DA framework.

6.2 Method

In this work, we consider a geological scenario that consists of two stages. In Stage 1, the fracture apertures are generated. We study a thin layer of fractured rock embedded between two impermeable and rigid layers. All fractures are present from the beginning, and we do not consider any fracture propagation. The fractures are initially closed and there is no history of tectonic faulting, uplift, or cooling. We apply a tectonic far-field stress and steadily increase the fluid pressure within the fractures. As the effective fracture normal stress decreases, some fractures begin to slip and consequently dilate due to asperity-sliding on the fracture surface. As a result, the apertures vary considerably from fracture to fracture. Due to numerous sources of uncertainty, e.g. in the stress state, rock properties or fracture roughness, the fracture apertures cannot be calculated deterministically but are also associated with some uncertainty. In Stage 2, we perform a tracer test to characterise the reservoir, while we assume that the fluid injection does not affect fracture aperture. We use an iterative ensemble-based data assimilation (DA) framework (Fig. 6.1) to history match fracture aperture and obtain a posterior aperture estimate with reduced uncertainty. In the following, the individual building blocks of the DA framework are explained in detail.

6.2.1 Prior ensemble of apertures with far-field stress approximation (FFSA)

Here, we present a simple and fast method for estimating fracture apertures that can be used to generate a reasonable prior ensemble with little computational cost. We approximate the stress state of each fracture from the far-field stress using Cauchy's equations (Eqs. (2.19) and (2.20)). In 2D, the equations read

$$\sigma_n = \sigma_H \cos^2\theta + \sigma_h \sin^2\theta \quad \text{and} \tag{6.1}$$

$$\sigma_s = (\sigma_h - \sigma_H)\sin\theta\cos\theta \quad , \tag{6.2}$$

where σ_H and σ_h are the maximum and minimum principal horizontal stresses and θ is the angle between σ_H and the fracture normal (Fig. 6.2). Those equations are only valid for a virtual plane in an intact material, as is the case when all fractures are closed and shear stress is fully transmitted by the fractures. This ignores any mechanical fracture interactions and hence only provides an approximate solution if shear displacement or tensile opening occurs in other fractures.

A fracture begins to slip when the shear stress acting on it exceeds frictional sliding strength, i.e. when $|\sigma_s| > \tau_{\max}$. We model the frictional sliding strength with Coulomb's friction law (Eq. (2.24)), which considers the effective normal stress and the friction angle. As the fracture slips, the shear stress relaxes until the arrest criterium $|\sigma_s| \leq \tau_{\max}$ presented in Eq. (2.25) is satisfied. We approximate the decrease $\Delta\sigma_s$ in shear stress for an increment $\Delta\delta_s$ of shear displacement with

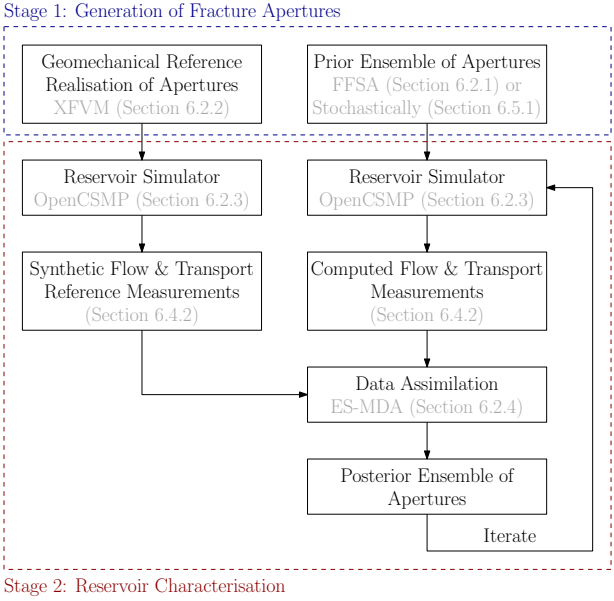

Figure 6.1: Iterative data assimilation framework used in this work

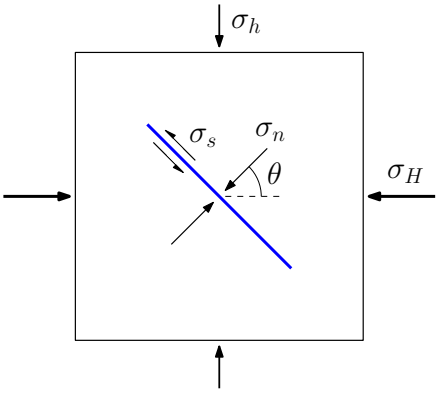

Figure 6.2: Projection of principal horizontal far-field stresses, σ_H and σ_h, onto a fracture

linear elastic theory (Eshelby & Peierls, 1957; Chinnery, 1969; Willis-Richards et al., 1996; Rahman et al., 2002), i.e., we assume

$$\frac{\Delta\sigma_s}{G} = C_g \frac{\Delta\delta_s}{L} \,, \tag{6.3}$$

where G is the shear modulus of the surrounding material, L the fracture length and C_g a proportionality factor. This then allows us to calculate the total shear displacement δ_s of a fracture. The amount of shear dilation δ_d is then obtained by integrating the tangent of the dilation angle ϕ_d over the shear displacement, i.e.,

$$\mathrm{d}\delta_d = \mathrm{d}\delta_s \tan(\phi_d) \quad \rightarrow \quad \delta_d = \int_0^{\delta_s} \tan(\phi_d)\, \mathrm{d}\delta_s \,. \tag{6.4}$$

In this work, we use the constitutive model of Barton and Bandis (Barton & Choubey, 1977; Barton, 1982; Bandis et al., 1983; Barton et al., 1985; Lei & Barton, 2022) to calculate friction and dilation angles (Appendix A). In this empirical model, these angles are algebraic functions of the shear displacement. They reach a peak value for a certain shear displacement and then decrease for larger displacements. Thus, Eqs. (2.24), (2.25) and (6.3) form a non-linear system of equations. The fracture aperture

$$a = a_0 - \delta_n + \delta_d \tag{6.5}$$

is a combination of an initial fracture aperture a_0, closure due to normal stress δ_n and shear dilation δ_d. We do not consider tensile opening and set the hydraulic aperture equal to the mechanical aperture.

6.2.2 Geomechanical reference realisation of apertures with XFVM

To generate an accurate reference of the aperture field, we need a proper geomechanical simulator. To this end, we employ an implementation of the extended finite volume method (XFVM), an embedded discrete fracture method that includes lower-dimensional fracture manifolds into Cartesian grids (Deb & Jenny, 2017a,b). In 2D, each fracture is divided into line segments, where each segment has one degree of freedom for shear slip, resulting in piecewise constant displacements along the fractures. Linear elasticity of the rock is assumed, the force balance is solved in an integral manner, and we use Coulomb's friction law (Eq. (2.24)) as a slip criterion. The displacement field is approximated by continuous basis functions at the grid points and discontinuous basis functions to represent fracture manifolds. These special discontinuous basis functions ensure that the displacement gradient is continuous across fracture manifolds, allowing the calculation of shear stress on fractures without additional constraints. We then solve the system of linear equations for the displacement at each grid point and the shear slip of the segments. As in our FFSA modelling, we calculate

shear dilation with the constitutive model of Barton and Bandis described in Appendix A. To this end, we adjust the dilation angle ϕ_d at each time step to account for changes in roughness while the shear dilation is coupled to the stresses and hence accounted for in the force balance, as is described in Conti et al. (2023). The fracture aperture of each segment is obtained from Eq. (6.5), where the initial aperture and normal closure are added in a post-processing step.

6.2.3 Flow and transport computation based on OpenCSMP

As a reservoir simulator, we use the Complex Systems Modelling Platform (OpenCSMP) (Matthäi et al., 2001; Geiger et al., 2004; Matthäi et al., 2007), a finite element – finite volume framework. It offers a wide range of functionality to calculate flow and transport processes with a focus on fractured porous media. In this work, we consider tracer transport by a steady-state velocity field (see Sections 2.1.1 and 2.1.2). We calculate the flow field of a single-phase fluid through a porous medium with Darcy's law (Eq. (2.7)) and the elliptic pressure equation (Eq. (2.9)). At time t_0, we start injecting a passive tracer which follows the flow field perfectly. The tracer does not alter the flow field and we neglect diffusion. We calculate the evolution of this tracer with the hyperbolic scalar transport equation (Eq. (2.13)). We solve tracer transport with a first-order version of discrete event simulation (DES) (Shao et al., 2019), a totally asynchronous local time stepping scheme.

6.2.4 Data assimilation with ESMDA

In this work, we use the ensemble smoother with multiple data assimilation (ESMDA) proposed by Emerick & Reynolds (2013) and presented in Section 4.4.5. As an ensemble smoother, the ESMDA collects all measurements in time and space in one vector and performs a Kalman update once the reservoir simulation is completed. The ESMDA alternately performs update steps with the same reference measurements and reruns the reservoir simulator with the updated parameters (Fig. 6.1). Those iterations are necessary due to the non-linear nature of the reservoir simulator.

We create a prior ensemble $z_{1:N_E}^{\text{prior}}$ of N_E realisations and one reference realisation z^{ref}. In this work, the parameter vector of a certain realisation i,

$$z_i = \left[\log_{10}(a_1^i)\,,\, \log_{10}(a_2^i)\,,\, \ldots\,,\, \log_{10}(a_{N_{\text{frac}}}^i) \right]^T\,, \tag{6.6}$$

contains the logarithms of the aperture values of all N_{frac} fractures. The reservoir simulator developed on the basis of OpenCSMP is applied to each realisation to obtain the corresponding measurement vector y_i, which consists of pressure values, volume flow rates and tracer arrival times.

In this work, we generate the synthetic reference realisation from XFVM and the prior ensemble from FFSA. Ideally, we would compare the FFSA prior to a prior ensemble generated from XFVM. However, generating such a prior with XFVM is computationally too expensive. We therefore compare it to prior ensembles from two naïve stochastic approaches which both sample from the unconditional probability density function (PDF) of the FFSA prior. In addition, we explore the implications of using a realisation from FFSA as the reference.

6.3 Fracture geometry

This study uses a realistic fracture geometry with $N_{\text{frac}} = 4051$ individual fractures (Fig. 6.3a) identical to the one in Liem et al. (2022b), except for minor changes in the classification of segments into individual fractures. The geometry was mapped by Odling (1997) from aerial photography of the Hornelen basin in western Norway. The mapped region extends over an area of 720×720 m, with aerial photos taken from a height of 370 m. The smallest observable features were 30 cm wide depressions filled with soil, grass or water. More fractures became visible at smaller observation heights; thus, the geometry shown in Fig. 6.3a represents merely a subset of the total fractures present.

The fracture pattern exhibits an approximately a log-normal distribution of fracture length (Fig. 6.3b) and a bi-modal distribution of fracture orientation with the most prominent peak at around 40° (Fig. 6.3c). The Hornelen basin is filled with Devonian-age Old Red Sandstone (e.g. Torsvik et al., 1988) with a very low permeability. The fracture apertures observed at the surface are not necessarily representative of the ones at reservoir depth, as stress conditions are markedly different. Therefore, we rely on the geomechanical simulator to calculate the reference apertures.

6.4 Simulation setup

The thin horizontal layer of fractured rock is embedded between two rigid and impermeable layers with fractures perpendicular to bedding. These assumptions enable us to approximate the model as 2D. We approximate the fractures by straight lines for the mechanical simulations (i.e. XFVM and FFSA). For the XFVM reference, we use a grid spacing of 2 m, resulting in roughly 46 000 fracture segments.

6.4.1 Uncertain model parameters

While we assume that we know the fracture geometry exactly, other geomechanical model parameters of Stage 1 are associated with some uncertainty (Table 6.1). We distinguish parameters that are equal for all fractures within one realisation

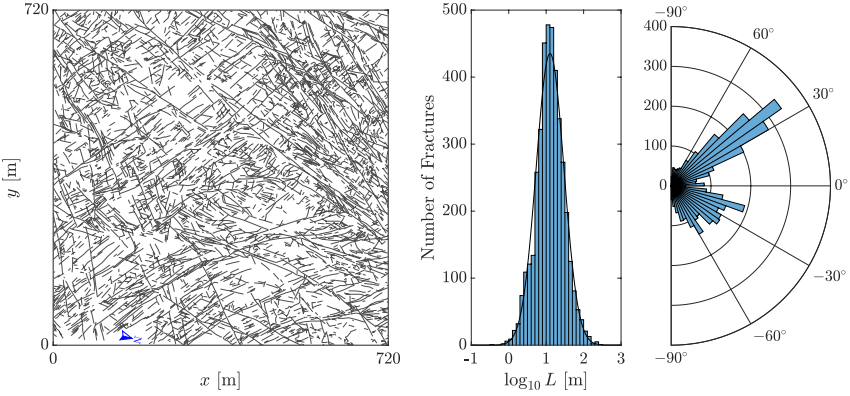

Figure 6.3: Fracture trace map of Hornelen basin outcrop (a) and histogram of logarithm of fracture length (b) and fracture orientation (c). The line in (b) shows a log-normal distribution with same mean and standard deviation. The fracture geometry was mapped by Odling (1997) and digitalised and discretised by Azizmohammadi & Matthäi (2017). Figure adapted from Liem et al. (2022b).

and sampled therefore only once per realisation (indicated with target 'R') and parameters that are different for each fracture within each realisation (target 'F'). Consequently, the total number of sampled model parameters per realisation is $8 + 5N_{\text{frac}} = 20\,263$. In the following, we discuss the parameters and their uncertainty in more detail.

We model a burial depth of the fractured reservoir of 1500 m, corresponding to an overburden stress σ_v of approximately 32 MPa based on an average rock density of around $2.2\,\text{g/cm}^3$. We assume a normal faulting regime (i.e. $\sigma_v > \sigma_H > \sigma_h$) and set the minimal principal horizontal stress to $\sigma_h \approx 0.7\sigma_v$. The orientation β of the maximum principal horizontal stress σ_H is described in Heidbach et al. (2018); here, we roughly align it to the x-axis of our coordinate system. We assume a constant fluid pressure p_f across the entire field. We choose a fluid pressure close to σ_h to get a reasonable amount of shearing but ensure that it remains smaller than σ_h to prevent tensile opening. Although the material properties of the rock (here Young's modulus E, Poisson's ratio ν, shear modulus $G = \frac{E}{2(1+\nu)}$, unconfined compressive strength σ_c, and residual friction angle ϕ_r) are rarely uniform in a reservoir, we approximate them as such. The chosen values are loosely inspired by Ojo & Brook (1990) and Hawkins & McConnell (1991).

Table 6.1: Uncertain geomechanical model parameters. We use scaled beta distributions defined by mean μ, standard deviation σ and [upper bound, lower bound]. For generating the prior ensemble with FFSA, we sample parameters with target 'R' only once per realisation and those with target 'F' for every fracture individually. The last column lists the input parameters for the reference simulation with XFVM.

Symbol	Unit	μ	σ	Bounds	Target	Ref
β	degree	0	5	[-15, 15]	R	0
σ_H	MPa	30	0.6	[28, 32]	R	29.7
σ_h	MPa	23	0.3	[22, 24]	R	23.3
p_f	MPa	21.5	0.15	[21, 22]	R	21.8
ϕ_r	degree	25	1	[22, 28]	R	25
σ_c	MPa	70	3	[61, 79]	R	70
E	MPa	5000	500	[3500, 6500]	R	5000
ν	–	0.25	0.0075	[0.2275, 0.2725]	R	0.25
JRC_{small}	–	6	1	[2, 10]	F	sampled
JRC_{large}	–	2	0.6	[0, 4]	F	sampled
K_{ni}	$\frac{\text{MPa}}{\text{mm}}$	20	5	[10, 30]	F	sampled
v_m^{rel}	–	0.5	0.125	[0.25, 0.75]	F	sampled
C_g	–	1	0.1	[0.7, 1.3]	F	–

The friction of the fracture planes plays a crucial role and represents a significant source of uncertainty. Two parameters describe friction in our constitutive model (Appendix A). The residual friction angle ϕ_r is a material property and describes friction of a planar rock surface. The joint roughness coefficient JRC, on the other hand, describes the increase of friction due to surface roughness which differs from fracture to fracture. In this work, we consider surface roughness at two different length scales: small-scale roughness at the level of the asperities (e.g. Pollard & Aydin, 1988) as described by the original Barton and Bandis model and modelled here with JRC_{small}, and an additional roughness compensating for idealising fractures as straight lines in our model. We calculate the combined joint

roughness coefficient as

$$JRC = JRC_{\text{small}} + JRC_{\text{large}} \cdot \log_{10}(L) \,, \tag{6.7}$$

where the fracture length L is in meters.

Additional fracture parameters in the Barton and Bandis model (Appendix A) include the initial normal stiffness K_{ni} and the maximum possible closure $v_m = v_m^{rel} a_0$. While the FFSA provides accurate results for a single fracture, it does not account for interactions between fractures (Appendix D). To address this limitation, we introduce additional uncertainty through the proportionality coefficient C_g that relates shear stress to shear displacement.

The amount of shear displacement and consequently also fracture aperture obtained from FFSA corresponds to the maximum value along the fracture length. In the frictionless case, shear displacement follows an elliptic profile (Eshelby & Peierls, 1957). Due to the non-linear constitutive model of Barton and Bandis, the profiles of shear displacement and aperture are only approximately elliptic. Those profiles can have in general arbitrary shapes in the XFVM. For simplicity, however, we assume a constant aperture over the length of a fracture and assign it to the maximum aperture value.

6.4.2 Parameters for flow and transport simulation and ESMDA updates

In Stage 2 of the geological scenario, we alternately perform tracer tests and update the fracture apertures with ESMDA. For the tracer test, we inject fluid through a single fracture named 'well fracture', which is located at the centre of the domain, and apply a constant pressure at all four boundaries (Fig. 6.4a). Starting at time $t_0 = 0$, a scalar tracer with concentration $c = 1$ is introduced into the injected fluid. We compute the steady-state velocity field and tracer transport using OpenCSMP (Section 6.2.3). The matrix domain is discretised with an unstructured triangular mesh, and the fractures are represented as lower-dimensional line elements (e.g., Azizmohammadi & Matthäi, 2017). In this work, we decouple flow and transport from the fracture mechanics, assuming that fluid injection does not affect fracture aperture. While this assumption can be invalid in real-world scenarios, it is necessary in our framework due to computational limitations. The relevant parameters for the flow and transport simulations are provided in Table 6.2. Note that we calculate fracture permeability from the aperture assuming plane Poiseuille flow between two parallel plates.

In this work, we assume that measurements along the domain boundary and in the well fracture are available (Fig. 6.4b). Concretely, we measure the maximum value of the steady-state pressure p_{in} along the well fracture and the volume flow rate $\dot{Q}_{\text{out}}$ through 20 model-boundray segments. Further, we monitor the evolution of the tracer concentration at certain locations on the boundary and either use the concentration value after 320 days, c_{320}, or the time it takes to

Table 6.2: Parameters for flow and transport simulation with OpenCSMP (adopted from Liem et al., 2022b)

Fluid viscosity	μ	$1 \times 10^{-3}\,\mathrm{Pa\,s}$
Matrix permeability	k_m	$3 \times 10^{-13}\,\mathrm{m}^2$
Matrix porosity	ϕ_m	0.15
Fracture permeability	k_f	$a_f^2/12$
Fracture porosity	ϕ_f	1.0
Pressure at all 4 boundaries	p_{out}	9 MPa
Inlet volume flow	$\dot{Q}_{\mathrm{in}}/l_w$	$2 \times 10^{-3}\,\mathrm{m}^2/\mathrm{s}$
Length of well fracture	l_w	56.48 m
CFL multiplier for DES		0.4

reach a concentration of 0.5, $t_{0.5}$, as measurements. The number of measurements and their locations are arbitrary choices. To evaluate the performance of the DA framework, we set 12 measurements (indicated in yellow in Fig. 6.4b) aside and use the remaining 60 measurements for the ESMDA updates. We call them test and training measurements, respectively. We scale the measurements as

$$\tilde{p}_{\mathrm{in}} = \frac{p_{\mathrm{in}} - p_{\mathrm{out}}}{p_{\mathrm{out}}} \quad , \quad \tilde{\dot{Q}}_{\mathrm{out}}^{(i)} = \frac{\dot{Q}_{\mathrm{out}}^{(i)}}{\dot{Q}_{\mathrm{in}}/20} \quad , \quad \tilde{t}_{0.5}^{(i)} = \frac{t_{0.5}^{(i)}}{640\,\mathrm{days}} \quad , \quad \tilde{c}_{320}^{(i)} = c_{320}^{(i)} \tag{6.8}$$

and collect them in the training and test measurement vectors

$$y = \left[\tilde{p}_{\mathrm{in}}\,,\, \tilde{\dot{Q}}_{\mathrm{out}}^{(1)}\,,\, \ldots\,,\, \tilde{\dot{Q}}_{\mathrm{out}}^{(16)}\,,\, \tilde{t}_{0.5}^{(1)}\,,\, \ldots\,,\, \tilde{t}_{0.5}^{(19)}\,,\, \tilde{c}_{320}^{(1)}\,,\, \ldots\,,\, \tilde{c}_{320}^{(24)}\right]^T \text{ and} \tag{6.9}$$

$$\breve{y} = \left[\tilde{\dot{Q}}_{\mathrm{out}}^{(17)}\,,\, \ldots\,,\, \tilde{\dot{Q}}_{\mathrm{out}}^{(20)}\,,\, \tilde{t}_{0.5}^{(20)}\,,\, \ldots\,,\, \tilde{t}_{0.5}^{(25)}\,,\, \tilde{c}_{320}^{(25)}\,,\, \ldots\,,\, \tilde{c}_{320}^{(26)}\right]^T\,, \tag{6.10}$$

respectively. Here, the superscript (i) denotes individual measurements of a certain quantity.

After obtaining those measurements for every realisation, we update the parameter vectors containing the logarithm of all 4051 fracture aperture values using ESMDA. For the scaled dimensionless measurements we assume a diagonal error covariance matrix R with each element of the diagonal set to 1×10^{-5}. In this work, we do not apply any covariance localisation or inflation. We study the influence of ensemble size N_E and the number of ESMDA iterations N_{iter} on the results of the DA framework. For a quantitative evaluation, we utilise the mean root-mean-square error defined as

$$\text{M-RMSE}_\xi = \frac{1}{N_\xi} \sum_{i=1}^{N_\xi} \sqrt{\frac{1}{N_E} \sum_{j=1}^{N_E} \left(\xi_i^{(j)} - \xi_i^{(\mathrm{ref})}\right)^2}\,, \tag{6.11}$$

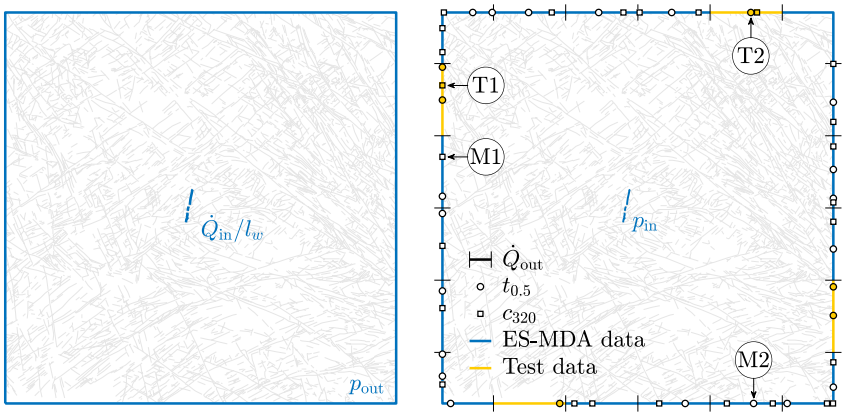

(a) (b)

Figure 6.4: Boundary conditions for the flow and transport simulations (a) and location of measurements for ESMDA updates (b). The boundary is divided into 20 segments, through which the flow rate is measured. Circles denote measurements of the time until the tracer concentration reaches 0.5, and squares denote tracer concentration measurements after 320 days. Measurements in blue are used in the ESMDA updates, while measurements marked in are test data used to evaluate the framework's performance. The labels M1-2 and T1-2 mark specific training and test locations, respectively.

where ξ can represent either the log-apertures x, training measurements y, or test measurement $\breve{y}$. Here, $\xi_i^{(j)}$ denotes the i-th entry in the corresponding vector of the j-th realisation, and N_ξ refers to the length of that vector.

6.5 Results

In this section, we first analyse the prior ensemble obtained from FFSA by comparing it to the reference realisation from XFVM as well as to two prior ensembles from the naïve stochastic approaches. Subsequently, we show that the prior ensemble from FFSA outperforms the stochastic approaches in our DA framework. Finally, we present results using the FFSA reference realisation.

6.5.1 Prior ensemble

We first compare the maximum aperture value of each fracture. The reference realisation obtained with XFVM is shown in Fig. 6.5 and realisations 1 to 6 of the

prior ensemble generated with FFSA are depicted in Figs. 6.6a–f, each obtained from a different set of sampled model parameter values. The realisations of the FFSA prior have a notable variability which reflects the uncertainty in the model parameters as defined in Table 6.1. Although none of the 6 prior realisations are particularly close to the reference, they nevertheless capture trends and features of it.

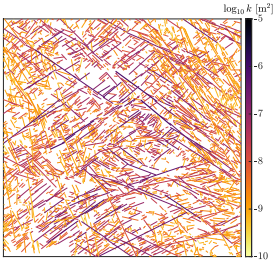

Figure 6.5: Reference realisation with XFVM. Line thickness corresponds to aperture width and line colour to $\log_{10}$ of the fracture permeability.

From the prior ensemble with FFSA, we extract the unconditional PDF of the apertures and related quantities from all fractures in all realisations (black curves in Fig. 6.7). The corresponding PDF from the reference simulation is shown in blue. Overall the two curves in Fig. 6.7 agree very well, although there are distinct differences. Firstly and most notably, the FFSA prior underestimates the number of fractures with moderate fracture permeability in the range of $10^{-8}\,\mathrm{m}^2$ to $10^{-7}\,\mathrm{m}^2$ (Fig. 6.7f). We attribute this to the slightly smaller mean shear displacement (Fig. 6.7c) which we believe is a consequence of neglecting fracture interactions. Secondly, the maximum values of shear displacement and subsequently also aperture are significantly higher in the FFSA prior than in the XFVM reference (Fig. 6.7c). This occurs when very small friction and C_g values are sampled for long and favourably oriented fractures in the FFSA prior. Such extreme values are not present in the parameter set of the reference. Lastly, fracture interaction can modify the local stress field, resulting in situations where the effective normal stress can become small or even negative. Therefore, some fractures in the XFVM reference experience little to no normal closure (Fig. 6.7b). In contrast, all fractures in the FFSA prior have positive effective normal stress and consequently some amount of normal closure, as fracture interaction is neglected there. Even with these differences, we expect the ensemble generated with FFSA to be a suitable prior for our DA framework.

We aim to compare the FFSA prior to two prior ensembles from naïve stochastic approaches. For the first approach, named here Stochastic Single Value prior, we sample one value per realisation from the unconditional PDF of the FFSA

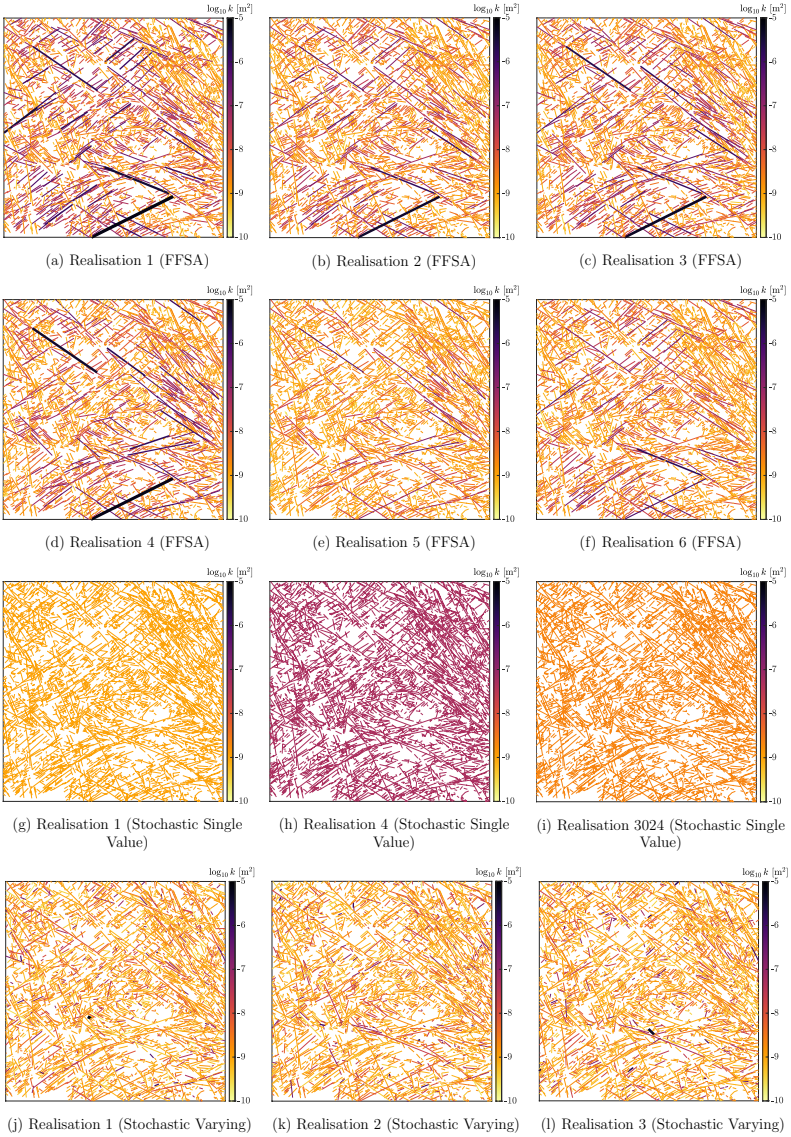

(a) Realisation 1 (FFSA) (b) Realisation 2 (FFSA) (c) Realisation 3 (FFSA)

(d) Realisation 4 (FFSA) (e) Realisation 5 (FFSA) (f) Realisation 6 (FFSA)

(g) Realisation 1 (Stochastic Single Value) (h) Realisation 4 (Stochastic Single Value) (i) Realisation 3024 (Stochastic Single Value)

(j) Realisation 1 (Stochastic Varying) (k) Realisation 2 (Stochastic Varying) (l) Realisation 3 (Stochastic Varying)

Figure 6.6: Realisations of the prior ensemble with FFSA (a–f), Stochastic Single Value (g–i) and Stochastic Varying (j–l). Line thickness corresponds to aperture width and line colour to $\log_{10}$ of the fracture permeability.

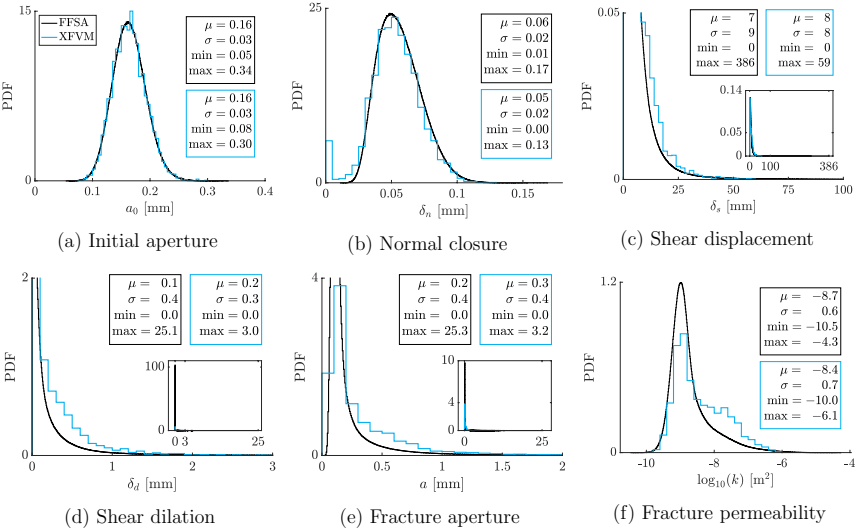

(a) Initial aperture (b) Normal closure (c) Shear displacement

(d) Shear dilation (e) Fracture aperture (f) Fracture permeability

Figure 6.7: Combined histogram of the values of all 4051 fractures in 5000 realisations with FFSA (black) and the reference simulation with XFVM (blue)

prior (i.e. black curve in Fig. 6.7e) and set all apertures in that realisation to this value. For the second approach, named Stochastic Varying prior, we independently sample aperture values for every fracture in every realisation from the same PDF. Figs. 6.6g–l show realisations of those two prior ensembles. Visually, the FFSA prior is much closer to the reference than the stochastic ones, even though all three prior ensembles follow the same unconditional PDF.

6.5.2 Posterior ensemble

Now we want to investigate how the three different prior ensembles perform in our DA framework. We first analyse the measurements and then the apertures of the posterior ensembles.

We monitor the evolution of the tracer concentration over time at specific locations on the boundary of the domain (Fig. 6.4b). Fig. 6.8 shows the resulting breakthrough curves at two training and two test locations for three prior ensembles of different sizes generated with FFSA and corresponding posterior ensembles. At the training locations, either a concentration or arrival time measurement is taken for the ESMDA update, whereas at test locations, the breakthrough curve measurement is solely used for evaluating the performance of ESMDA but not in

the update itself. The largest ensemble contains 5000 realisations, of which the smaller ensembles are subsets that consist of the first 500 and 2000 realisations, respectively.

The breakthrough curves of the prior ensembles have a considerable spread at all four locations as a result of the uncertain fracture apertures. At training locations, the posterior ensembles closely match the reference realisation from XFVM. We obtain a good match of the entire breakthrough curves even though only a single concentration or arrival time measurement per location is used. In test locations, the level of uncertainty is only slightly reduced, and a considerable spread remains in the posterior ensembles. With the FFSA prior we get essentially converged results already for an ensemble size of 500, as the results remain consistent for larger ensemble sizes.

The same breakthrough curves for the Stochastic Varying prior are shown in Fig. 6.9. Here, the posterior of the smallest ensemble size (i.e., with $N_E = 500$) collapsed and converged to a wrong solution. Results with larger ensemble sizes are generally fine; however, test location T1 indicates that $N_E = 2000$ is not large enough for full convergence regarding ensemble size. Compared to the FFSA prior, the ensemble spread is larger for the Stochastic Varying prior, both in the prior ensembles and consequently also in the posterior ensembles.

We quantify the performance of the FFSA and Stochastic Varying priors with the mean root-mean-square error of the training and test measurements, as defined in Eq. (6.11), for different ensemble sizes and numbers of ESMDA iterations (Fig. 6.10). Comparing the FFSA posterior to its prior, we see that the error in the training measurements is drastically reduced, while the error in the test measurements is only slightly smaller. An ensemble size of 500 and 4 ESMDA iterations is sufficient to achieve satisfactory results for the FFSA prior. For the Stochastic Varying prior however, a combination of ensemble size and number of ESMDA iterations beyond our computational capabilities is required for converged results. Compared to FFSA, the training and test errors of the Stochastic Varying prior are 1.8 and 3.0 times larger, respectively. For the combination with the smallest errors (i.e., with $N_E = 5000$ and $N_{\text{iter}} = 4$), the corresponding ratios in the posterior are 3.9 and 2.1. In short, the results from the FFSA prior match the measurements better than the ones from the Stochastic Varying prior, but the latter also produces a posterior with substantially reduced measurement errors, given a sufficiently large ensemble size.

A significant difference exists between the updated fracture apertures obtained with the two methods. Fig. 6.11 shows some realisations of the posterior ensembles obtained from the FFSA and Stochastic Varying priors for $N_E = 5000$ and $N_{\text{iter}} = 4$. Generally, the posterior realisations of FFSA (Fig. 6.11a–f) are more similar to the reference than the corresponding realisations from the prior ensemble (Fig. 6.6a–f), and the variability of the realisations in the ensemble is reduced. For example, realisations 5 and 6 show overall increased apertures, and the apertures of the prominent long fractures are slightly reduced in realisation 1.

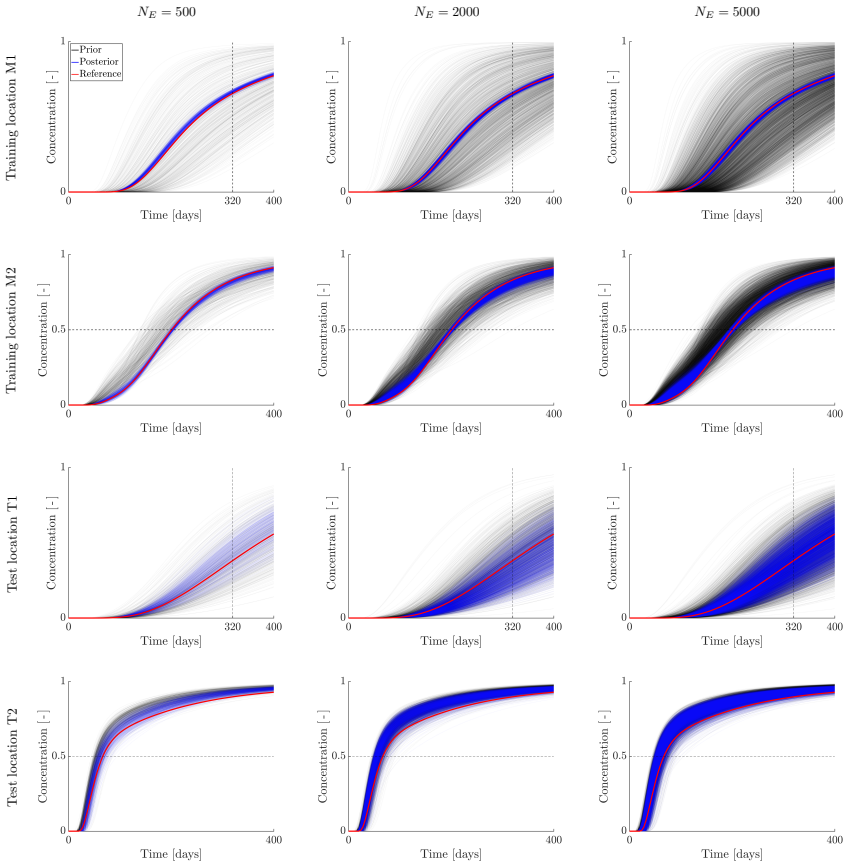

Figure 6.8: Breakthrough curves of the FFSA prior. The prior ensemble is in black, the posterior ensemble in blue and the XFVM reference in red. The locations of two training and two test locations are indicated in Fig. 6.4. The columns correspond to different ensemble sizes and the dashed lines indicate the measurements.

However, the posterior realisations are not an exact match to the reference, as the apertures of long and optimally oriented fractures are still overestimated, while the ones of many short fractures are underestimated. These qualitative observations are supported by Fig. 6.12a, which shows a slight improvement in the unconditional PDF of the FFSA posterior compared to the prior. Conversely, the posterior

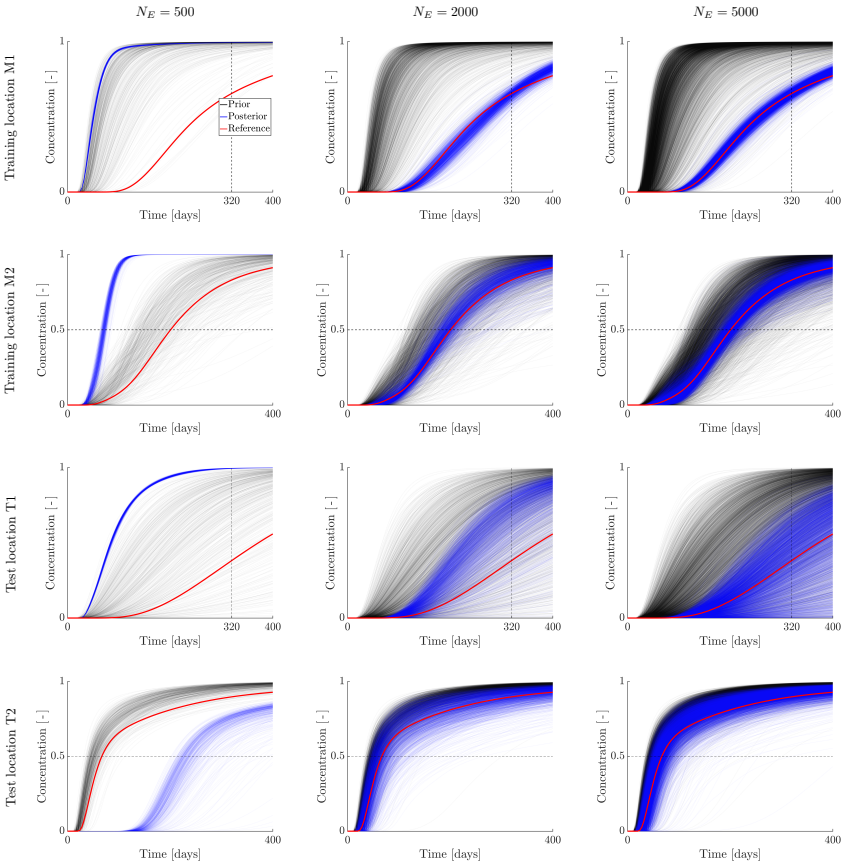

Figure 6.9: Breakthrough curves of the Stochastic Varying prior. The prior ensemble is in black, the posterior ensemble in blue and the XFVM reference in red. The locations of two training and two test locations are indicated in Fig. 6.4. The columns correspond to different ensemble sizes and the dashed lines indicate the measurements.

realisations of the Stochastic Varying priors (Fig. 6.11g–i) appear to be almost identical to the corresponding prior realisations (Fig. 6.6j–l), and only fractures near measurement locations are visibly improved. The corresponding unconditional PDF shows extreme minimum and maximum permeability values which reach unphysical levels. The mean root-mean-square errors of the log-apertures

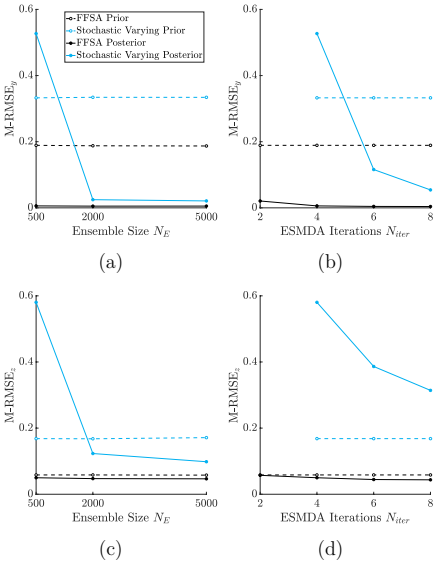

Figure 6.10: Mean root-mean-square error (M-RMSE) of training (a, b) and test (c, d) measurements calculated with Eq. (6.11). Figures (a, c) show results for $N_{\text{iter}} = 4$ and (b, d) for $N_E = 500$.

(Fig. 6.12b–c) show a marginal improvement for FFSA but no improvement for the Stochastic Varying prior. The drastic increase in the posterior errors for the Stochastic Varying prior arises from an ensemble collapse to a wrong solution.

The Stochastic Single Value prior fails to produce satisfactory results in the DA framework, leading to ensemble collapse regardless of the ensemble size and number of ESMDA iterations. In light of this, we calculate the root-mean-square error of the training measurements for each prior realisation as

$$\text{RMSE}_y^{(j)} = \sqrt{\frac{1}{N_y}\sum_{i=1}^{N_y}\left(y_i^{(j)} - y_i^{(ref)}\right)^2} \tag{6.12}$$

and find the one with the smallest error (Fig. 6.13a). The best realisation has an aperture of 0.16 mm and is shown in Fig. 6.6i. Although some breakthrough curves obtained from this realisation show somewhat acceptable agreement with the reference (Fig. 6.13c), others display substantial errors (Fig. 6.13b). As expected, it is therefore not possible to match the complex flow and transport behaviour of the reference when using only a single value for all fracture apertures.

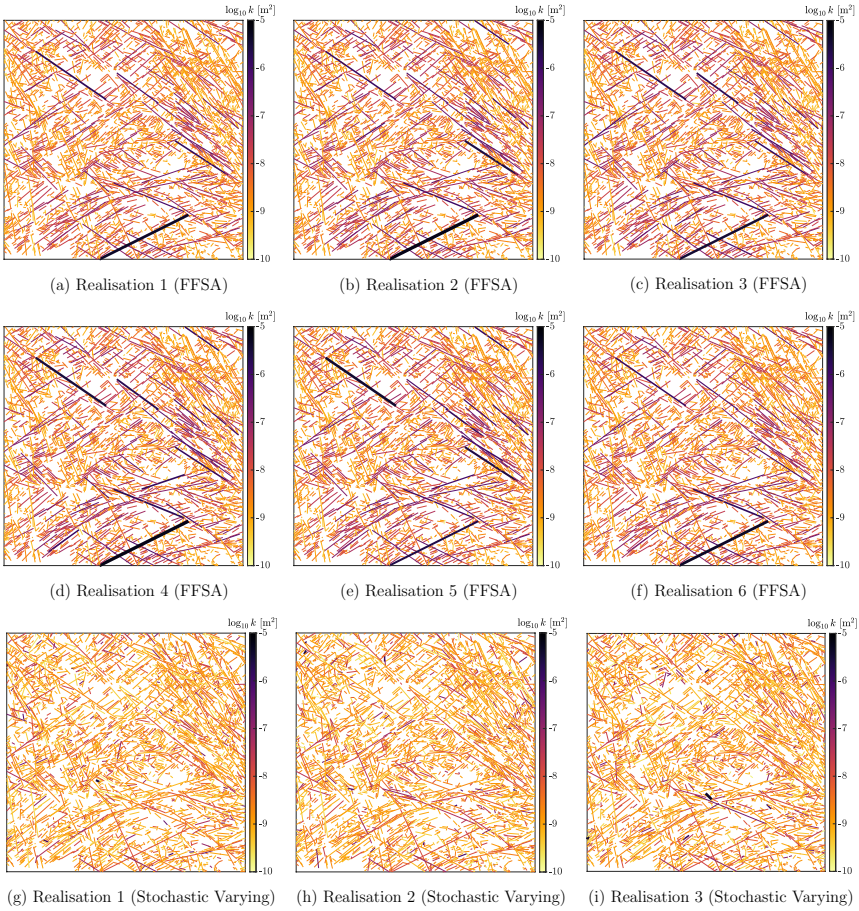

(a) Realisation 1 (FFSA) (b) Realisation 2 (FFSA) (c) Realisation 3 (FFSA)

(d) Realisation 4 (FFSA) (e) Realisation 5 (FFSA) (f) Realisation 6 (FFSA)

(g) Realisation 1 (Stochastic Varying) (h) Realisation 2 (Stochastic Varying) (i) Realisation 3 (Stochastic Varying)

Figure 6.11: Realisations of the posterior ensemble obtained from the FFSA prior (a–f) and the Stochastic Varying prior (g–i) for $N_E = 5000$ and $N_{\text{iter}} = 4$. Line thickness corresponds to aperture width and line colour to $\log_{10}$ of the fracture permeability.

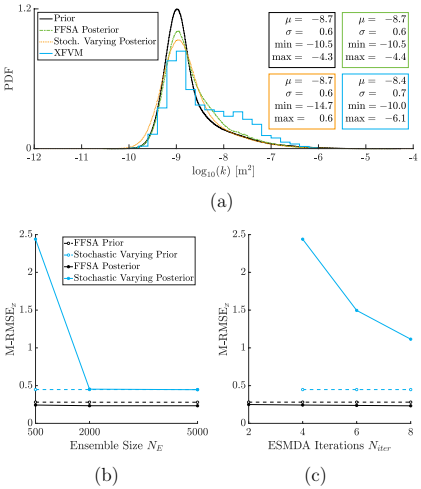

Figure 6.12: Combined histogram of fracture permeability values of all 4051 fractures for $N_E = 5000$ and $N_{\text{iter}} = 4$ (a) and mean root-mean-square error (M-RMSE) of log-apertures calculated with Eq. (6.11) for $N_{\text{iter}} = 4$ (b) and $N_E = 500$ (c)

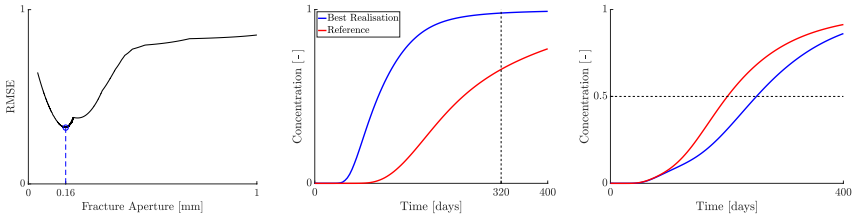

(a) RMSE of training data (b) Training location M1 (c) Training location M2

Figure 6.13: Root-mean-square error (RMSE) of the training data for the Stochastic Single Value prior shows that the realisation with a fracture aperture of 0.16 mm has the smallest error (a). Breakthrough curves at two locations as indicated in Fig. 6.4 for this best realisation in blue and the XFVM reference in red (b, c).

6.5.3 Reference realisation with FFSA

The results presented in the previous section are obtained using the reference realisation generated with XFVM. In this section, we repeat this study using a reference realisation from FFSA (Fig. 6.14). We obtain this FFSA reference by sampling the underlying model parameters from the distributions presented in Table 6.1, the same way as for realisations of the prior ensemble, just with a different random seed.

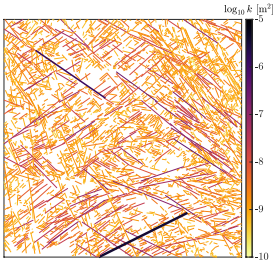

Figure 6.14: Reference realisation with FFSA. Line thickness corresponds to aperture width and line colour to $\log_{10}$ of the fracture permeability.

We use the same prior ensemble generated with FFSA as in the previous section; Figs. 6.6a–f depict the first few prior realisations. Here, we use prior ensembles of 100, 500 and 2000 realisations. Fig. 6.15 shows the breakthrough curves of the FFSA reference realisation, the FFSA prior ensemble and the corresponding posterior ensemble. For the larger two ensemble sizes, the posterior ensembles match the reference well in the two locations where training measurements are available while the spread is only slightly reduced in the two test locations. Overall, these results look similar to the corresponding ones obtained with the XFVM reference realisation (Fig. 6.8). For the DA problem at hand, an ensemble of only 100 realisations is not large enough and leads to a collapse of the posterior ensemble.

These findings are confirmed in Fig. 6.16, which compares mean root-mean-square errors of the prior and posterior ensembles when using the FFSA or XFVM reference realisation for different ensemble sizes and numbers of ESMDA iterations. The posterior ensembles drastically reduce the errors of the training measurements, while there is only a moderate reduction in the errors of the test measurements. Those results are pretty similar to the ones obtained with the XFVM reference. Note also that the measurement errors of the prior ensembles are almost identical for the two references. The results for the FFSA reference are essentially converged for an ensemble size of 500 and 2 ESMDA iterations, although minor improvements in the apertures can be obtained with more ESMDA iterations.

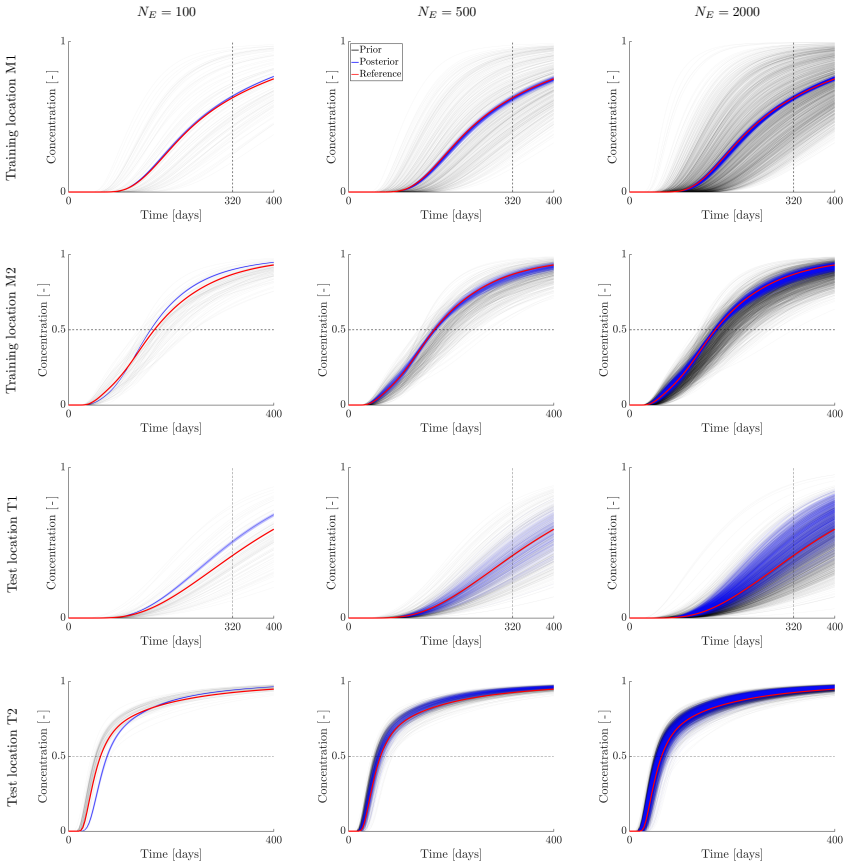

Figure 6.15: Breakthrough curves of the FFSA prior using the FFSA reference. The prior ensemble is in black, the posterior ensemble in blue and the FFSA reference in red. The locations of two training and two test locations are indicated in Fig. 6.4. The columns correspond to different ensemble sizes and the dashed lines indicate the measurements.

While the measurement errors for the two references are nearly identical, the errors in the logarithm of the apertures differ significantly (Figs. 6.16e–f). The prior ensemble is much closer to the FFSA reference than the XFVM reference, evident in a 30% lower mean RMSE. Moreover, the DA framework almost halves the mean RMSE for the FFSA reference, while the posterior error for the XFVM

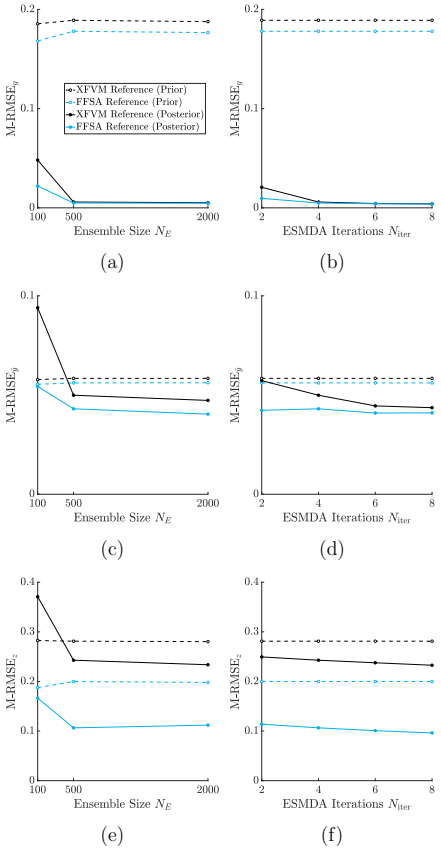

Figure 6.16: Mean root-mean-square error (M-RMSE) of training (a, b) and test (c, d) measurements and log-apertures (e, f) calculated with Eq. (6.11). The blue lines show results using the FFSA reference whereas the black lines are obtained with the XFVM reference, both using the same FFSA prior ensemble. Figures (a, c, e) show results for $N_{\text{iter}} = 4$ and (b, d, f) for $N_E = 500$.

reference is only around 20% smaller than its prior error. Consequently, the posterior ensemble for the FFSA reference has a much smaller error than the posterior ensemble for the XFVM reference. Accordingly, the posterior realisations closely resemble the FFSA reference. Fig. 6.17 shows the fracture apertures of six realisations of the posterior ensemble for $N_E = 2000$ and $N_{\text{iter}} = 4$. They

demonstrate a much closer alignment with their reference realisation compared to the case with the XFVM reference depicted in Figs. 6.11a–f.

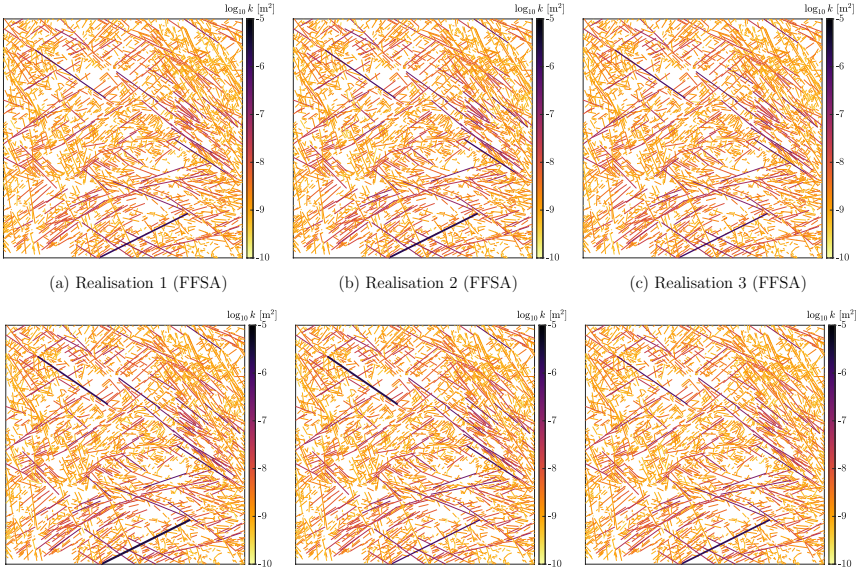

(a) Realisation 1 (FFSA) (b) Realisation 2 (FFSA) (c) Realisation 3 (FFSA)

(d) Realisation 4 (FFSA) (e) Realisation 5 (FFSA) (f) Realisation 6 (FFSA)

Figure 6.17: Realisations of the posterior ensemble obtained from the FFSA prior using the FFSA reference for $N_E = 2000$ and $N_{\text{iter}} = 4$. Line thickness corresponds to aperture width and line colour to $\log_{10}$ of the fracture permeability.

6.6 Discussion

The FFSA provides reasonable approximations of the fracture apertures in a scenario dominated by shear dilation. With negligible computational effort, it is thereby substantially faster than a geomechanical simulator like XFVM. The FFSA takes less than a minute for the presented fracture model, while the XFVM runs for several days. However, neither code is fully optimised for speed, and there is potential to significantly improve the computational efficiency of XFVM. The speed of FFSA makes it an attractive option for generating prior ensembles for DA purposes, as typically a large number of realisations is required. In contrast, using geomechanical simulators for this task might become computationally prohibitive.

The FFSA is only exact for a single isolated fracture with constant friction angle, and it neglects fracture interactions. This leads to modelling errors (see Appendix D for a direct comparison to XFVM), particularly as shearing of a fracture will change the local stress field considerably. To compensate for those errors, we introduce additional uncertainty through the parameter C_g, a proportionality factor between shear stress and shear displacement. While this approach gives overall satisfactory results, moderate fracture permeabilities are under-represented in the PDF of the FFSA prior ensemble compared to the one of the reference realisation obtained with XFVM (Fig. 6.7f), indicating that the chosen approach is not yet optimal. With the current approach, the fracture length has a much larger influence on the shear displacement than the parameter C_g because the chosen uncertainty in C_g is much smaller than the variation of the fracture length in our model (Eq. (6.3)). Increasing the uncertainty in C_g would however lead to more extreme values for long fractures. Therefore, an improved approach should increase the probability of moderate apertures for short fractures without generating extremely high apertures for long fractures. For example, we could model the uncertainty of C_g as a function of fracture length or introduce an additive uncertainty directly to the fracture aperture in Eq. (6.5). Another approach is adding additional uncertainty to the stress state, thereby modelling the change in the local stress state at one fracture due to the shearing of other fractures. Further, we could improve the FFSA itself by incorporating knowledge of the surrounding fracture geometry or using a hierarchical approach, i.e., first estimating shear displacement and apertures of the large fractures, and then deriving the local stress field at the smaller ones.

Even without these improvements, the FFSA produces prior realisations that are much closer to the reference than the two naïve stochastic approaches. Subsequently, the FFSA prior also leads to a better posterior ensemble than the stochastic approaches. At least for the chosen setting, a better prior leads to a better posterior and it is therefore crucial to model the prior in a physically realistic way.

In this work, we confirm that it is not possible to retrieve the complex flow and transport behaviour of the reference when using only a single value for all fracture apertures. Even when the optimal single aperture is used, the resulting realisation still has a considerable error in the measurements, leading to completely wrong estimates of some breakthrough curves (Fig. 6.13). The Stochastic Single Value prior led to an ensemble collapse in our DA framework irrespective of the ensemble size. We believe this collapse results from a combination of factors. Firstly, the relations between the single aperture value and certain measurements become constant above or below specific thresholds, resulting in a loss of ensemble variation for those measurements and, in extreme cases, an identical measurement value for all realisations. Secondly, some of those relations exhibit non-monotonic behaviour such that realisations can be attracted by non-optimal local minima. Thirdly, the Stochastic Single Value prior generates realisations confined to a lim-

ited subset with highly correlated measurements, leading to numerical issues when calculating the Kalman gain (Eq. (4.41) in Section 4.4.3). Lastly, one reference measurement lies entirely outside of the range of the prior ensemble. Due to the resulting ensemble collapse, we were unable to obtain any DA results for this prior.

While the Stochastic Single Value prior is too restrictive, the Stochastic Varying prior bears too much uncertainty. It does not incorporate all available knowledge, such as correlations of fracture aperture with length and orientation. As a consequence, a large ensemble size is required to avoid undersampling. In this study, undersized ensembles collapsed and converged to wrong solutions. Results suggest that a smaller ensemble size might be possible with more ESMDA iterations, but the required combination of ensemble size and number of ESMDA iterations is beyond our current computational capabilities, and thus, our results with this prior are not fully converged. Nevertheless, we expect that results with a much larger ensemble size are similar to the ones from our best combination ($N_E = 5000$, $N_{\text{iter}} = 4$). With this combination, we obtain a posterior ensemble that matches the training measurements, i.e., measurements that are used for the ESMDA update, quite well. The improvement in the test measurements, which are solely used for evaluating the outcome of the DA framework, is smaller and a considerable amount of uncertainty remains. The apertures of the posterior realisations differ however significantly from the reference realisation, with updates predominantly occurring near measurement locations. This emphasises the importance of considering more than just the (training) measurements when evaluating the effectiveness of a DA framework.

With the FFSA prior, we obtain posterior realisations with an improved estimation of the apertures compared to the ones from the prior ensemble, even though a considerable difference to the reference realisation remains. The posterior ensemble matches the training measurements of the reference realisation very well, while the test measurements are only marginally improved, indicating that the improvements in flow and transport are mostly limited to the vicinity of training measurements. More measurements, especially also from the interior of the domain, are needed to further improve the estimation of aperture as well as the flow and transport. However, the number of measurement locations already exceeds what one can expect in field studies and a complete observation of flow and transport is only possible in lab experiments such as in Flemisch et al. (2024). While there is room for improvement, the posterior from the FFSA prior gives good estimates of the fracture aperture suitable for performance estimation and risk assessment in subsurface applications. Concrete examples involve optimal placement of boreholes for injection or extraction, expected heat extraction in a geothermal reservoir, or preventing potential contamination of nearby aquifers.

Further, we compare results for two reference realisations: one obtained from XFVM and the other from FFSA. As anticipated, generating the reference realisation and the prior ensemble with the same method gives a better match, both in the prior and posterior, than using two different methods. This part of

our study yields two key conclusions. First, it emphasises the importance of accurately modelling the prior ensemble. Second, it demonstrates the significance of employing a reference realisation from a different method when evaluating a DA framework with a synthetic reference, as otherwise, the DA problem becomes artificially simplified.

Our results, especially the ones with the Stochastic Varying prior, suggest that most apertures only have a negligible influence on the measurements at the boundaries. While this is expected to some degree, we also identify three constraints in our study setup that artificially limit the influence of the fractures. Firstly, we use a first-order transport scheme which leads to a considerable amount of numerical diffusion. If smears out the concentration front and thus dampens the effects of the fractures. We could avoid this by using a higher-order scheme and only include a controlled amount of physical diffusion. Secondly, the sensitivity of the fracture apertures on the flow and transport measurements is highly dependent on the ratio of matrix to fracture permeability (Phillips, 1991; Matthäi & Belayneh, 2004, see also Chapter 5). In cases with very low matrix permeability, the flow is therefore governed by the fracture geometry, favouring flow paths with minimal matrix distances. In this regime, fracture aperture influences flow only when equivalent flow paths exist. Conversely, in cases with very high matrix permeability, flow predominantly occurs within the matrix, largely independent of fracture parameters. Only in an intermediate range of matrix permeabilities do the fracture apertures significantly influence flow and transport. Note that the fracture permeability is always greater than the matrix permeability for open fractures. We have not optimised the matrix permeability for maximum sensitivity to aperture, as it is not a tuning parameter in practical scenarios. Lastly, boundary conditions might contribute to these limitations as well. By imposing a fixed pressure on the domain's boundary, we disregard that the fractured rock typically extends beyond the region of interest. Flow and transport near the boundary are strongly influenced by the boundary condition. Alternative approaches, such as implementing infinite boundary conditions or using measurements only in the interior of the domain, might decrease the influence of the boundary conditions on the measurements and represent real-world conditions more accurately.

Nevertheless, the posterior from the FFSA prior also shows slightly improved apertures in the interior of the domain. In such priors, apertures of fractures with similar length and orientation are correlated. Hence, fractures in the interior of the domain are correlated to measurements through similar fractures near the measurement locations and therefore also updated by ESMDA. In reality, apertures are correlated with length and orientation (Barton et al., 1995; Baghbanan & Jing, 2008; Barton & Quadros, 2015; Zhang et al., 2021b), and such indirect updates are desired to some extent. However, the current implementation of the FFSA prior overestimates these correlations, leading to a posterior with deficient variability. We expect that these issues can be resolved by the above-mentioned improvements of FFSA.

In this study, we used a geological scenario in which the generation of the fracture apertures occurs before the reservoir characterisation with the tracer test. However, injecting fluid into the reservoir during the tracer test may significantly alter the effective normal stresses acting on the fractures and consequently change the fracture apertures, which in turn may affect the flow field. In future works, it is therefore desirable to couple flow and mechanics and consider poroelasticity. A further step towards a more realistic setting is the extension to 3D, which is straightforward for FFSA (Milliotte et al., 2018). The far-field stresses can be projected onto the fracture planes with a 3D version of Eqs. (6.1) and (6.2), and the process of approximating the maximum shear displacement is similar to that in 2D. For that purpose, Chinnery (1969) lists values of the proportionality factor C_g for various fracture shapes. Special attention must be given to the definition of fracture length, however. In future work, we could also consider additional model parameters as uncertain, such as matrix permeability and porosity, and allow for uncertainties in the boundary conditions of the tracer test. Here, we consider rock properties as spatially homogeneous, but we could also model them with e.g. Gaussian random fields as in Liem et al. (2022b).

Arguably the biggest assumption in this work is that we know the fracture geometry (i.e., location, orientation and length of each fracture) *a priori* and exactly. In reality, the fracture geometry is usually associated with substantial uncertainty, as only sparse borehole data and statistical information are available. Nevertheless, valuable insight is obtained from the current study, as discussed above. We therefore see it as a necessary intermediate step towards a more realistic setup that eventually also includes uncertain fracture geometry. Several existing tools can be used or built upon to generate physically meaningful realisations of a fracture geometry, as demonstrated by Hyman et al. (2015), Lei et al. (2017), Gläser et al. (2020), and Paluszny et al. (2020). It should then be straightforward to update input parameters of the fracture generator (such as statistics of e.g. fracture length or density). It is however very challenging to update the actual fracture geometry itself. Parametrising the generated fracture geometry efficiently and effectively for this purpose is complex as the number of fractures can vary between realisations, and a fracture from one realisation generally does not have a bijectively related fracture in other realisations. Existing approaches based on level set function or Hough transform (Ping et al., 2017; Chai et al., 2018; Yao et al., 2018), to our knowledge, have not been applied to complex large fracture geometries yet. The task becomes even more challenging if the parameterisation should also reflect relations between fractures, including fractures terminating against other fractures and formation history. Additionally, automatic remeshing of the updated fracture geometry might be challenging as arbitrary small distances or angles may occur.

6.7 Conclusion

In this work, we suggest using the far-field stress approximation (FFSA), a proxy model designed to estimate fracture apertures in shear-dominated scenarios, to generate prior ensembles for data assimilation (DA). The FFSA captures the general trends effectively, albeit with some inherent errors due to neglecting fracture interactions. We use FFSA to generate realistic and computationally efficient prior ensembles for ensemble-based data assimilation. To compensate for modelling errors, we introduce supplementary uncertainty in one model parameter. Comparing FFSA priors to those from two naïve stochastic approaches reveals notable differences. While all methods share the same underlying unconditional PDF, FFSA-derived realisations are much closer to the reference realisation from a geomechanical simulator.

Employing ESMDA, we update fracture apertures with flow and transport data. The posterior ensemble obtained from the FFSA prior matches the flow and transport behaviour as well as the apertures, although some differences remain. In contrast, a posterior ensemble obtained by unconditional sampling of aperture (i.e., a Stochastic Varying prior) yields apertures that substantially deviate from the reference despite matching training measurements. In addition, a significantly larger ensemble size is required than for the FFSA prior, increasing overall computational cost. The third prior, which uses a single value for all fracture apertures in a realisation, cannot match the complex flow and transport behaviour of our synthetic reference. Our results show a correlation between the prior and posterior uncertainties, highlighting the importance of a good estimate of the prior ensemble. We expect that those results also apply to other ensemble-based DA methods, such as particle filters.

While the current form of FFSA already produces reasonable results, opportunities for improvement, particularly in addressing modelling errors through additional uncertainties, remain. To achieve this, we plan to conduct a more detailed study with the FFSA in a separate work. Further potential improvements for the ESMDA framework include constructing a prior ensemble that combines realisations from different methods and the use of adaptive localisation. Moreover, we aim to make the framework more realistic by coupling flow and transport with mechanics, incorporating additional physics like heat transport, and eventually accounting for uncertainty in fracture geometry.

Open research section

MATLAB scripts of the far-field stress approximation (FFSA), the ANSYS mesh of the fracture geometry, input and output files of the reference simulation with extended finite volume method (XFVM), and prior and posterior ensembles of the data assimilation framework based on the ensemble smoother with multiple data assimilation (ESMDA) are available at ETH Zurich via https://doi.org/10.3929/ethz-b-000632502 (Liem et al., 2023a).

7 Conclusion and Outlook

7.1 Conclusion

This thesis addresses two key challenges in modelling fractured porous media: enhancing the efficiency of transport simulations and refining the characterisation of uncertain fracture properties.

In the first part of the thesis, we extend the adaptive conservative time integration (ACTI) scheme – an adaptive time stepping technique – to fractured porous media (Chapter 3). Initially introduced by Jenny (2020), ACTI can drastically reduce the computational costs in simulations with highly heterogeneous porous media compared to conventional global time stepping. However, it poses more restrictive stability requirements for higher-order flux schemes, given that nearly all grid cells have CFL numbers exceeding half the maximal allowed CFL number. We study different versions of the monotonic upstream-centred scheme for conservation laws (MUSCL) and empirically demonstrate that MUSCL with advection of inclined reconstruction (MUSCL-AIR) fulfils these stability requirements.

ACTI proves particularly efficient when only a few cells demand very small time steps, while the majority can be integrated using much larger time steps. This phenomenon is present in transport within fractured porous media, where highly permeable fractures can form preferential flow paths characterised by substantial velocity contrasts. Moreover, adaptive grid refinement can amplify this effect. We apply ACTI in combination with MUSCL-AIR to model tracer transport in fractured porous media and obtain accurate and sharp concentration fronts. Notably, we achieve impressive speed-up factors up to approximately 80 compared to conventional global time stepping. These speed-up factors stem from a comparable reduction in the number of flux calculations and cell updates. We anticipate that these gains will increase in more complex models. In practice, the reduced computational cost of ACTI relative to conventional global time stepping enables more accurate solutions within given computational constraints.

In the second part of this thesis, we study how measurement strategy and matrix permeability affect the estimation of fracture parameters using ensemble-based data assimilation (DA) (Chapter 5). Our findings confirm that incorporating more measurement data generally improves posterior estimation. In our fracture model, we observe that pressure and flow rates at wells have a more significant impact on the accuracy of the posterior than arrival time measurements. However, this observation may be biased by factors such as the tracer mixing in fracture

cells, boundary conditions, and measurement error covariance matrix. Further investigation is required to explore this effect thoroughly.

Moreover, our study demonstrates a pronounced influence of the matrix permeability on the fracture aperture and length estimates. When the ratio of fracture to matrix permeability is low (i.e., for high matrix permeabilities), fractures have minimal impact on the flow field, making their estimation challenging based on flow and transport data alone. Flow in fractured porous media is sensitive to aperture variation only within an intermediate range of matrix permeability. In this study, this range is found to be around 1×10^{-14} to $1 \times 10^{-12}\,\mathrm{m}^2$. Conversely, fracture length influences flow even under high fracture-to-matrix permeability ratios (i.e., very low matrix permeabilities), resulting in accurate estimates for matrix permeabilities of approximately $1 \times 10^{-13}\,\mathrm{m}^2$ and lower in our study. We anticipate that these ranges are specific to each problem and may vary depending on the particular fracture geometry involved.

In the third part of this work, we demonstrate the importance of accurate prior modelling in ensemble-based DA (Chapter 6). Typically, studies – including the one presented in Chapter 5 – use simplistic distributions to sample prior fracture properties. Such simple distributions fail to incorporate all available knowledge, especially that derived from geomechanical processes. However, creating an entire ensemble of prior realisations of fractures with a geomechanical reservoir simulator might become computationally prohibitive, especially for large ensemble sizes. Hence, we introduce a proxy model, the far-field stress approximation (FFSA), designed to efficiently calculate fracture apertures in shear-dominated environments. The FFSA projects the tectonic far-field stresses onto fracture planes and approximates shear displacement using linear elastic theory. Thus, the FFSA achieves efficiency by neglecting local variations in the stress field caused by factors such as fracture interactions.

We employ the FFSA to generate prior aperture realisations for a two-dimensional fracture pattern mapped from the air, comprising approximately 4000 individual fractures. The FFSA effectively captures the general trends of the apertures in this realistic fracture geometry. The resulting posterior ensemble obtained from our ensemble-based DA framework matches the flow and transport behaviour of the synthetic reference at measurement locations. It improves the estimation of fracture aperture, although some differences remain. In contrast, an unconditional sampling of the apertures from a simple distribution yields posterior aperture realisations that substantially deviate from the reference despite matching training measurements. Moreover, a significantly larger ensemble size is required than for the FFSA prior, thereby increasing their overall computational cost.

In conclusion, this thesis provides tools for a more efficient and accurate simulation of fractured porous media. Those tools can contribute to improved reservoir management and decision-making in various subsurface applications, which are crucial for solving today's energy and climate challenges.

7.2 Outlook

This thesis focuses on two-dimensional fracture networks and, except for Chapter 6, a low number of fractures. While small and understandable models are valuable for developing new methods and obtaining basic knowledge, their ultimate goal is their application in real-world scenarios. Subsurface reservoirs are inherently three-dimensional, extend over large distances, and possess countless fractures of varying shapes and sizes. Therefore, future research should address adapting the methods presented here to such complex scenarios. While the techniques presented in this thesis, in particular ACTI with MUSCL-AIR and FFSA, can theoretically be extended to three dimensions, their practical implementation in 3D requires careful consideration.

Further, subsurface reservoirs are subject to dynamic changes. Processes such as reservoir stimulation, heat extraction, and CO_2 or tracer injection alter the local stress field. Such stress alterations potentially lead to the creation of new fractures or the modification of existing ones through fracture growth, shearing, or tensile opening. A natural progression is extending the ACTI scheme, which has previously been applied to compressible flows (Kulka & Jenny, 2022), to multiphase flow and integrate it with a geomechanical simulator. Furthermore, our DA framework must account for those dynamic processes by employing appropriate forward models and accommodating time-dependent fractures. Moving forward, applying these enhanced tools to real-world reservoirs using field data is crucial.

This work primarily focuses on estimating fracture apertures under the assumption of a known fracture geometry. While this approach has produced valuable insights, real-world scenarios involve uncertain fracture geometries with an unknown number of fractures, presenting severe challenges for data assimilation methods. Effectively addressing these challenges requires the development of efficient parametrisation methods for fracture geometry, ensuring that the resulting posterior geometry remains physically meaningful. Additionally, the DA framework must be capable of accommodating a variable number of fractures. To the best of our knowledge, no existing method fulfils these requirements.

APPENDICES

A Fracture Aperture Model of Barton and Bandis

This chapter introduces the constitutive model for fracture aperture of Barton and Bandis (Barton & Choubey, 1977; Barton, 1982; Bandis et al., 1983; Barton et al., 1985) and largely follows the corresponding section in the appendix of Liem et al. (2023b, Preprint).

In the model of Barton and Bandis, the (void) aperture of a fracture,

$$a = a_0 - \delta_n + \delta_d \ , \tag{A.1}$$

is a combination of the initial aperture a_0, closure due to normal stress δ_n and dilation due to shearing δ_d.

A.1 Initial fracture aperture

The initial aperture

$$a_0 = \frac{JRC}{5}\left(0.2\frac{\sigma_c}{JCS} - 0.1\right) \tag{A.2}$$

corresponds to the fracture aperture under stress-free conditions. It is a function of the (peak) joint roughness coefficient JRC and the amount of joint alteration described by the ratio of unconfined compressive strength of the rock σ_c and joint wall compression strength JCS.

A.2 Normal closure

Assuming a positive effective normal stress $\sigma_{\text{eff}} > 0$, the amount of closure is

$$\delta_n = \frac{\sigma_{\text{eff}} v_m}{K_{ni} v_m + \sigma_{\text{eff}}} \ , \tag{A.3}$$

where v_m and K_{ni} are the maximum possible closure and the initial normal stiffness, respectively. Under increasing normal stress, more and more asperities are in contact and consequently, the normal stiffness of the fracture increases.

The model of Barton and Bandis is not applicable if fluid pressure exceeds normal stress (i.e. for negative σ_{eff}) and tensile opening occurs. In those situations, the amount of tensile opening can be directly obtained from the geomechanical simulation or analytical models (e.g. Pollard & Segall, 1987).

A.3 Friction and dilation angle

The amount of shear displacement δ_s of a fracture is determined by the stress state at the fracture and the friction angle (Eqs. (2.24) and (2.25)). The friction angle depends thereby on the roughness of the fracture surface and on the rock material. The model of Barton and Bandis represents the influence of latter with the residual friction angle ϕ_r which can be obtained from the basic friction angle ϕ_b using the Schmidt hammer test (Barton & Choubey, 1977). The basic friction angle describes the friction of a smooth unweathered rock surface, while the residual friction angle $\phi_r \leq \phi_b$ is used for weathered surfaces. A key feature of the model of Barton and Bandis is that the friction angle

$$\phi' = JRC_{mob} \log_{10}\left(\frac{JCS}{\sigma_{\text{eff}}}\right) + \phi_r \tag{A.4}$$

and dilation angle

$$\phi_d = \frac{1}{M}(\phi' - \phi_r) = \frac{1}{M} JRC_{mob} \log_{10}\left(\frac{JCS}{\sigma_{\text{eff}}}\right) \tag{A.5}$$

are not constant but vary with the amount of shear displacement. This dependency is modelled with the mobilised joint roughness coefficient JRC_{mob} (Fig. A.1). The peak shear displacement δ_{peak} corresponds to the amount of shearing when peak shear strength is reached. Several models for peak shear strength exist, in this work we use

$$\delta_{\text{peak}} = 0.0077 L^{0.45} \left(\frac{\sigma_{\text{eff}}}{JCS}\right)^{0.34} \cos\left(JRC \cdot \log_{10}\left(\frac{JCS}{\sigma_{\text{eff}}}\right)\right) , \tag{A.6}$$

as proposed by Asadollahi & Tonon (2010), where L is the fracture length in metre. For pre-peak shearing ($\delta_s < \delta_{\text{peak}}$), the degradation of the few asperities that are in contact increases the interlocking between the two fracture surfaces and consequently increases the friction. For post-peak shearing ($\delta_s > \delta_]\text{peak}$) on the other hand, roughness is getting destroyed and smoothed out. Subsequently, shear strength and dilation angle are steadily reduced. For an infinite amount of shearing, the friction angle is equal to the residual friction angle and the dilation angle approaches zero.

For the damage coefficient M in Eq. (A.5) we use the formula proposed by Barton & Choubey (1977)

$$M = 0.7 + JRC \Big/ \left[12 \log_{10}\left(\frac{JCS}{\sigma_{\text{eff}}}\right)\right] . \tag{A.7}$$

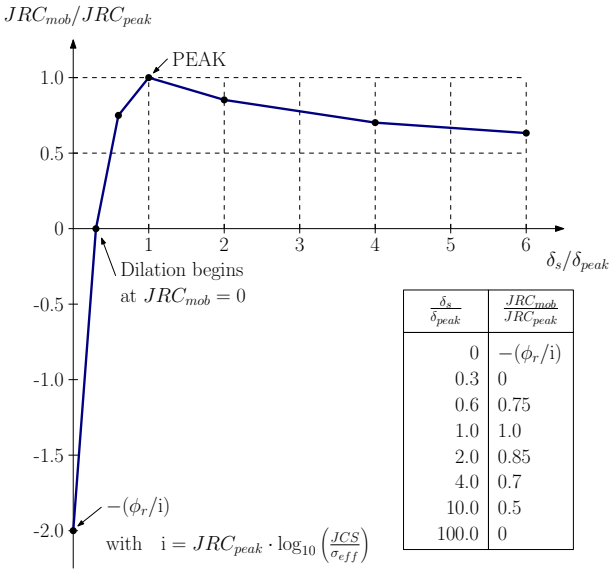

$\frac{\delta_s}{\delta_{peak}}$	$\frac{JRC_{mob}}{JRC_{peak}}$
0	$-(\phi_r/\mathrm{i})$
0.3	0
0.6	0.75
1.0	1.0
2.0	0.85
4.0	0.7
10.0	0.5
100.0	0

Figure A.1: Mobilised joint roughness coefficient JRC_{mob} as a function of shear displacement δ_s. Figure reproduced from Liem et al. (2022b), original figure from Barton (1982) and Barton et al. (1985).

A.4 Simplifications applied in Chapter 6

In Chapter 6, we assume that the fractures are unaltered and unweathered, i.e. $JCS = \sigma_c$. Therefore, the initial aperture simplifies to $a_0 = JRC/50$ and depends on the surface roughness only, and the residual friction angle is equal to the basic friction angle, i.e. $\phi_r = \phi_b$.

Further, we neglect the decrease in aperture for small shear displacements, and therefore, integrate only over positive dilation angles in Eq. (6.4). The model of Barton and Bandis has been developed for fractures with a constant fluid pressure and thus, a relatively constant effective normal stress. In our simulation, however, the fluid pressure steadily increases, and the effective normal stress might become very small in some fractures or even locally negative for some segments in the reference simulation with XFVM. We therefore approximate σ_{eff} in Eqs. (A.4) to (A.7) as

$$\sigma_{\text{eff}} \approx \sigma_n - \frac{1}{2}\left(\frac{|\sigma_s|}{\tan\phi_r} + p_f^{\text{end}}\right) , \tag{A.8}$$

where we calculate σ_n and σ_s with Cauchy's equations (Eqs. (6.1) to (6.2)) and p_f^{end} is the target fluid pressure.

B ACTI Algorithm

This chapter is part of the appendix published in Liem et al. (2022a).

Algorithm 5 delineates the adaptive conservative time integration (ACTI) scheme as introduced by Jenny (2020) and described in Chapter 3. In this work, we consider transport only in steady-state velocity fields; hence, we need to calculate the local time steps only once at the beginning.

Algorithm 5 ACTI scheme for scalar tracer transport Jenny (2020)

define grid with N cells Ω_I; $\forall I \in \{1, ..., N\}$
define $\mathcal{A}(I)$ as the set of neighbours of cell I
$t \leftarrow 0$
choose $\Delta t_{\max}$ such that $\text{mod}(t^{\text{end}}, \Delta t_{\max}) = 0$
for $I = 1, ..., N$ **do**
  $c_I \leftarrow$ initialize
  $t_I \leftarrow 0$
  $\forall J \in \mathcal{A}(I) : F_{J \to I} \leftarrow 0$
end for

while $(t < t^{\text{end}})$ **do**
  $t \leftarrow t + \Delta t_{\max}$
  for $I = 1, ..., N$ **do**
    compute Δt_I^{CFL}
    $L_I \leftarrow \max(\, \text{ceil}[\ln(\Delta t_I^{CFL} / \Delta t_{\max}) / \ln(1/2)] \,,\, 0\,)$
    $\Delta t_I \leftarrow \Delta t_{\max} / 2^{L_I}$
  end for
  while $(\min(t_I) < t)$ **do**
    $t_{next,min} \leftarrow \min_{I \in \{1,...,N\}}(t_I + \Delta t_I)$
    $S \leftarrow (I \in 1, ..., N \,|\, t_I + \Delta t_I = t_{next,min} \ \wedge \ \forall i < j \leq \text{size}(S) \Rightarrow L_{S_i} \geq L_{S_j})$
    for $I \in S$ **do**
      $t_I \leftarrow t_I + \Delta t_I$
      for $J \in \mathcal{A}(I)$ **do**
        if $(t_J < t_I)$ **then**
          $F_{J \to I} \leftarrow$ inflow from Ω_J into Ω_I during time $t' \in [t_I - \Delta t_I, t_I]$
          $F_{I \to J} \leftarrow F_{I \to J} - F_{J \to I}$
        end if
      end for
    end for
    for $I \in S$ **do**
      $c_I \leftarrow c_I + |\Omega_I|^{-1} \sum_{J \in \mathcal{A}(I)} F_{J \to I}$
      $\forall J \in \mathcal{A}(I) : F_{J \to I} \leftarrow 0$
    end for
  end while
end while

C Influence of Slope Limiter

This chapter is part of the appendix published in Liem et al. (2022a).

Chapter 3 studies different versions of the monotonic upstream-centered scheme for conservation laws (MUSCL) (Eq. (3.4)). We demonstrate that MUSCL without slope advection ($\beta_1 = 1$, $\beta_2 = \beta_3 = 0$) and MUSCL with slope advection ($\beta_1 = \beta_2 = 1$, $\beta_3 = 0$) show spurious oscillations in the tracer concentration when combined with ACTI. However, stability of these flux schemes can be attained by choosing a more diffusive limiter. Fig. C.1 shows concentration fields obtained with the minmod limiter. Compared to the fields obtained with the Koren limiter and the same $CFL_{\max}$ values (Fig. 3.4), the spurious oscillations are substantially reduced albeit at the cost of slightly more diffusive concentration fronts.

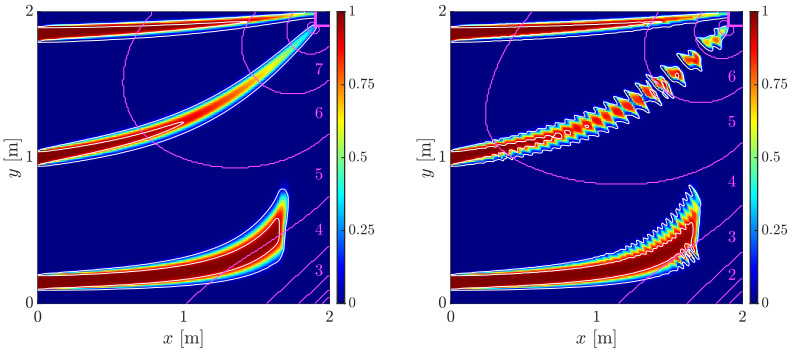

(a) MUSCL without slope advection ($CFL_{\max} = 0.5$)

(b) MUSCL without slope advection ($CFL_{\max} = 0.9$)

(c) MUSCL with slope advection ($CFL_{\max} = 0.5$)

(d) MUSCL with slope advection ($CFL_{\max} = 0.9$)

Figure C.1: Concentration field after 22 h for adaptive time stepping with ACTI using the minmod limiter. The white contour lines mark concentration values of 0.1 and 0.9. The pink contour lines depict the levels L_I of ACTI.

D Comparison of XFVM and FFSA

This chapter is part of the appendix published in Liem et al. (2023b, Preprint).

Here, we compare the fracture apertures obtained with the extended finite volume method (XFVM) and the far-field stress approximation (FFSA), both methods are discussed in Chapter 6. Fig. D.1 shows the results of XFVM and FFSA for the exact same underlying model parameters (i.e. the values from the last column of Table 6.1) and $C_g = 1$. The FFSA captures the general trends and some apertures agree quite well. However, there are also quite large differences for many fractures. Most notably, the apertures of long, optimally oriented fractures are overestimated while the apertures of some short fractures are underestimated. We intend to compare those two methods thoroughly in a separate publication.

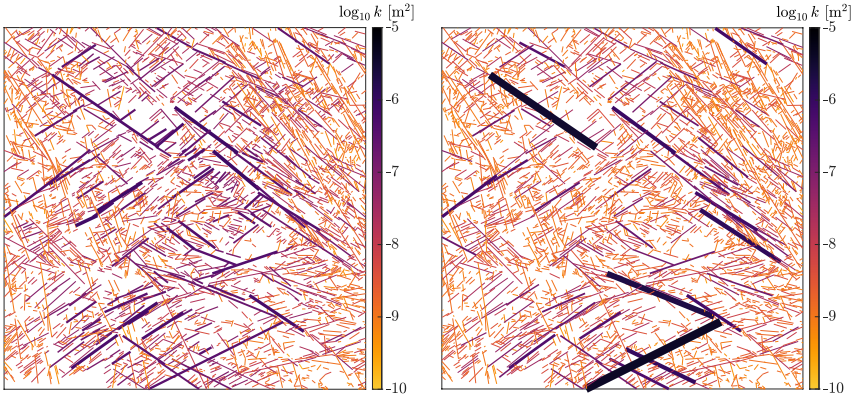

(a) (b)

Figure D.1: Results with XFVM (a) and FFSA (b) for the same underlying model parameters. Line thickness corresponds to aperture width and line colour to $\log_{10}$ of the fracture permeability.

Bibliography

Aanonsen, S. I., Nœvdal, G., Oliver, D. S., Reynolds, A. C., & Vallès, B. (2009). The ensemble kalman filter in reservoir engineering—a review. *SPE Journal*, *14*, 393–412. doi:10.2118/117274-PA.

Adler, P. M., Thovert, J.-F., & Mourzenko, V. V. (2012). *Fractured porous media*. Oxford: Oxford university press. doi:10.1093/acprof:oso/9780199666515.001.0001.

Agheshlui, H., Sedaghat, M. H., & Azizmohammadi, S. (2019). A comparative study of stress influence on fracture apertures in fragmented rocks. *Journal of Rock Mechanics and Geotechnical Engineering*, *11*, 38–45. doi:10.1016/j.jrmge.2018.05.003.

Agheshlui, H., Sedaghat, M. H., & Matthai, S. (2018). Stress influence on fracture aperture and permeability of fragmented rocks. *Journal of Geophysical Research: Solid Earth*, *123*, 3578–3592. doi:10.1029/2017JB015365.

Al-Dhafeeri, A. M., & Nasr-El-Din, H. A. (2007). Characteristics of high-permeability zones using core analysis, and production logging data. *Journal of Petroleum Science and Engineering*, *55*, 18–36. doi:10.1016/j.petrol.2006.04.019.

Ali, M. Y., Bouchaala, F., Bouzidi, Y., Takam Takougang, E. M., Mohamed, A. A. I., & Sultan, A. (2021). Integrated fracture characterization of thamama reservoirs in abu dhabi oil field, united arab emirates. *SPE Reservoir Evaluation & Engineering*, *24*, 708–720. doi:10.2118/206737-PA.

Amann, F., Gischig, V., Evans, K., Doetsch, J., Jalali, R., Valley, B., Krietsch, H., Dutler, N., Villiger, L., Brixel, B., Klepikova, M., Kittilä, A., Madonna, C., Wiemer, S., Saar, M. O., Loew, S., Driesner, T., Maurer, H., & Giardini, D. (2018). The seismo-hydromechanical behavior during deep geothermal reservoir stimulations: open questions tackled in a decameter-scale in situ stimulation experiment. *Solid Earth*, *9*, 115–137. doi:10.5194/se-9-115-2018.

Anderson, E. M. (1905). The dynamics of faulting. *Transactions of the Edinburgh Geological Society*, *8*, 387–402.

Anderson, E. M. (1951). *The dynamics of faulting and dyke formation with applications to Britain*. ([2nd, rev. ed.] ed.). Edinburgh: Oliver and Boyd.

Anderson, J. L., & Anderson, S. L. (1999). A monte carlo implementation of the nonlinear filtering problem to produce ensemble assimilations and forecasts. *Monthly Weather Review*, *127*, 2741–2758. doi:10.1175/1520-0493(1999)127<2741:AMCIOT>2.0.CO;2.

Asadi, M. S., Rasouli, V., & Barla, G. (2012). A bonded particle model simulation of shear strength and asperity degradation for rough rock fractures. *Rock Mechanics and Rock Engineering*, *45*, 649–675. doi:10.1007/s00603-012-0231-4.

Asadollahi, P., & Tonon, F. (2010). Constitutive model for rock fractures: Revisiting barton's empirical model. *Engineering Geology*, *113*, 11–32. doi:10.1016/j.enggeo.2010.01.007.

Asch, M., Bocquet, M., & Nodet, M. (2016). *Data Assimilation: Methods, Algorithms, and Applications*. Fundamentals of Algorithms. Philadelphia: Society for Industrial and Applied Mathematics. doi:10.1137/1.9781611974546.

Azizmohammadi, S., & Matthäi, S. K. (2017). Is the permeability of naturally fractured rocks scale dependent? *Water Resources Research*, *53*, 8041–8063. doi:10.1002/2016WR019764.

Baghbanan, A., & Jing, L. (2008). Stress effects on permeability in a fractured rock mass with correlated fracture length and aperture. *International Journal of Rock Mechanics and Mining Sciences*, *45*, 1320–1334. doi:10.1016/j.ijrmms.2008.01.015.

Bandis, S. C., Lumsden, A. C., & Barton, N. R. (1983). Fundamentals of rock joint deformation. *International Journal of Rock Mechanics and Mining Sciences & Geomechanics Abstracts*, *20*, 249–268. doi:10.1016/0148-9062(83)90595-8.

Bannister, R. N. (2017). A review of operational methods of variational and ensemble-variational data assimilation. *Quarterly Journal of the Royal Meteorological Society*, *143*, 607–633. doi:10.1002/qj.2982.

Barenblatt, G. I., Zheltov, I. P., & Kochina, I. N. (1960). Basic concepts in the theory of seepage of homogeneous liquids in fissured rocks [strata]. *Journal of applied mathematics and mechanics*, *24*, 1286–1303.

Barton, C. A., Zoback, M. D., & Moos, D. (1995). Fluid flow along potentially active faults in crystalline rock. *Geology*, *23*, 683–686. doi:10.1130/0091-7613(1995)023<0683:FFAPAF>2.3.CO;2.

Barton, N. (1982). *Modelling rock joint behavior from in situ block tests: implications for nuclear waste repository design* volume 308. Columbus: Office of Nuclear Waste Isolation, Battelle Project Management Division.

Barton, N., Bandis, S., & Bakhtar, K. (1985). Strength, deformation and conductivity coupling of rock joints. *International Journal of Rock Mechanics and Mining Sciences & Geomechanics Abstracts*, *22*, 121–140. doi:10.1016/0148-9062(85)93227-9.

Barton, N., & Choubey, V. (1977). The shear strength of rock joints in theory and practice. *Rock mechanics*, *10*, 1–54. doi:10.1007/BF01261801.

Barton, N., & Quadros, E. (2015). Anisotropy is everywhere, to see, to measure, and to model. *Rock Mechanics and Rock Engineering*, *48*, 1323–1339. doi:10.1007/s00603-014-0632-7.

Baud, P., Reuschlé, T., & Charlez, P. (1996). An improved wing crack model for the deformation and failure of rock in compression. *International Journal of Rock Mechanics and Mining Sciences & Geomechanics Abstracts*, *33*, 539–542. doi:10.1016/0148-9062(96)00004-6.

Bear, J. (1988). *Dynamics of fluids in porous media*. Dover Books on Physics and Chemistry. New York, N.Y: Dover Publications.

Berger, M. J., & Oliger, J. (1984). Adaptive mesh refinement for hyperbolic partial differential equations. *Journal of Computational Physics*, *53*, 484–512. doi:10.1016/0021-9991(84)90073-1.

Berre, I., Doster, F., & Keilegavlen, E. (2018). Flow in fractured porous media: A review of conceptual models and discretization approaches. *Transport in Porous Media*, *130*, 215–236. doi:10.1007/s11242-018-1171-6.

Bertino, L., Evensen, G., & Wackernagel, H. (2003). Sequential data assimilation techniques in oceanography. *International Statistical Review*, *71*, 223–241. doi:10.1111/j.1751-5823.2003.tb00194.x.

Blaskovich, F. T., Cain, G. M., Sonier, F., Waldren, D., & Webb, S. J. (1983). A multicomponent isothermal system for efficient reservoir simulation. In *Middle East Oil Technical Conference and Exhibition* (pp. SPE–11480–MS). doi:10.2118/11480-MS.

Boersma, Q. D., Bruna, P. O., de Hoop, S., Vinci, F., Moradi Tehrani, A., & Bertotti, G. (2021). The impact of natural fractures on heat extraction from tight triassic sandstones in the west netherlands basin: a case study combining well, seismic and numerical data. *Netherlands Journal of Geosciences*, *100*, e6. doi:10.1017/njg.2020.21.

Bossart, P., Bernier, F., Birkholzer, J., Bruggeman, C., Connolly, P., Dewonck, S., Fukaya, M., Herfort, M., Jensen, M., Matray, J.-M., Mayor, J. C., Moeri, A., Oyama, T., Schuster, K., Shigeta, N., Vietor, T., & Wieczorek, K. (2018). Mont terri rock laboratory, 20 years of research: introduction, site characteristics and overview of experiments. In P. Bossart, & A. G. Milnes (Eds.), *Mont Terri Rock Laboratory, 20 Years: Two Decades of Research and Experimentation on Claystones for Geological Disposal of Radioactive Waste* (pp. 3–22). Cham: Springer International Publishing. doi:10.1007/978-3-319-70458-6_1.

Brenner, O., Piroozmand, P., & Jenny, P. (2022). Efficient assimilation of sparse data into rans-based turbulent flow simulations using a discrete adjoint method. *Journal of Computational Physics*, *471*, 111667. doi:10.1016/j.jcp.2022.111667.

Brown, G. O. (2002). Henry darcy and the making of a law. *Water Resources Research*, *38*, 11–1–11–12. doi:10.1029/2001WR000727.

Bui, M., Adjiman, C. S., Bardow, A., Anthony, E. J., Boston, A., Brown, S., Fennell, P. S., Fuss, S., Galindo, A., Hackett, L. A., Hallett, J. P., Herzog, H. J., Jackson, G., Kemper, J., Krevor, S., Maitland, G. C., Matuszewski, M., Metcalfe, I. S., Petit, C., Puxty, G.,

Reimer, J., Reiner, D. M., Rubin, E. S., Scott, S. A., Shah, N., Smit, B., Trusler, J. P. M., Webley, P., Wilcox, J., & Mac Dowell, N. (2018). Carbon capture and storage (ccs): the way forward. *Energy & Environmental Science*, *11*, 1062–1176. doi:10.1039/C7EE02342A.

Béal, D., Brasseur, P., Brankart, J. M., Ourmières, Y., & Verron, J. (2010). Characterization of mixing errors in a coupled physical biogeochemical model of the north atlantic: implications for nonlinear estimation using gaussian anamorphosis. *Ocean Science*, *6*, 247–262. doi:10.5194/os-6-247-2010.

Carrassi, A., Bocquet, M., Bertino, L., & Evensen, G. (2018). Data assimilation in the geosciences: An overview of methods, issues, and perspectives. *WIREs Climate Change*, *9*, e535. doi:doi.org/10.1002/wcc.535.

Casini, G., Hunt, D. W., Monsen, E., & Bounaim, A. (2016). Fracture characterization and modeling from virtual outcrops. *AAPG Bulletin*, *100*, 41–61. doi:10.1306/09141514228.

Chai, Z., Tang, H., He, Y., Killough, J., & Wang, Y. (2018). Uncertainty quantification of the fracture network with a novel fractured reservoir forward model. In *SPE Annual Technical Conference and Exhibition* (p. 19). SPE: Society of Petroleum Engineers. doi:10.2118/191395-MS.

Chang, H., Zhang, D., & Lu, Z. (2010). History matching of facies distribution with the enkf and level set parameterization. *Journal of Computational Physics*, *229*, 8011–8030. doi:10.1016/j.jcp.2010.07.005.

Chen, Y., & Oliver, D. S. (2010). Cross-covariances and localization for enkf in multiphase flow data assimilation. *Computational Geosciences*, *14*, 579–601. doi:10.1007/s10596-009-9174-6.

Chen, Y., & Oliver, D. S. (2012). Ensemble randomized maximum likelihood method as an iterative ensemble smoother. *Mathematical Geosciences*, *44*, 1–26. doi:10.1007/s11004-011-9376-z.

Chen, Y., & Oliver, D. S. (2013). Levenberg–marquardt forms of the iterative ensemble smoother for efficient history matching and uncertainty quantification. *Computational Geosciences*, *17*, 689–703. doi:10.1007/s10596-013-9351-5.

Chen, Y., & Oliver, D. S. (2017). Localization and regularization for iterative ensemble smoothers. *Computational Geosciences*, *21*, 13–30. doi:10.1007/s10596-016-9599-7.

Chen, Y., & Zhang, D. (2006). Data assimilation for transient flow in geologic formations via ensemble kalman filter. *Advances in Water Resources*, *29*, 1107–1122. doi:10.1016/j.advwatres.2005.09.007.

Chilès, J.-P., & Delfiner, P. (2012). *Geostatistics : modeling spatial uncertainty*. Wiley series in probability and statistics (2nd ed.). Hoboken, N.J: Wiley.

Chinnery, M. A. (1969). Theoretical fault models. In K. Kasahara, & A. Stevens (Eds.), *A symposium on Processes in the Focal Region* (pp. 211–223). Ottawa: Publ. Dominion Obs. volume 37. doi:doi.org/10.4095/315467.

Churakov, S. V., Hummel, W., & Fernandes, M. M. (2020). Fundamental research on radiochemistry of geological nuclear waste disposal. *CHIMIA*, *74*, 1000. doi:10.2533/chimia.2020.1000.

Constantinescu, E. M., & Sandu, A. (2007). Multirate timestepping methods for hyperbolic conservation laws. *Journal of Scientific Computing*, *33*, 239–278. doi:10.1007/s10915-007-9151-y.

Conti, G., Deb, R., Matthäi, S. K., & Jenny, P. (2024). Consistent treatment of shear failure in embedded discrete fracture models using xfvm. *International Journal for Numerical and Analytical Methods in Geomechanics*, *48*, 951–973. doi:10.1002/nag.3671.

Conti, G., Matthäi, S., & Jenny, P. (2023). XFVM modelling of fracture aperture induced by shear and tensile opening. *Computational Geosciences*, . doi:10.1007/s10596-023-10214-5.

Courant, R., Friedrichs, K., & Lewy, H. (1928). Über die partiellen differenzengleichungen der mathematischen physik. *Mathematische Annalen*, *100*, 32–74. doi:10.1007/BF01448839.

Darcy, H. (1856). *Les fontaines publiques de la ville de Dijon: exposition et application des principes à suivre et des formules à employer dans les questions de distribution d'eau* volume 1. Victor dalmont.

Dawson, C. (1995). High resolution upwind-mixed finite element methods for advection-diffusion equations with variable time-stepping. *Numerical Methods for Partial Differential Equations*, *11*, 525–538. doi:10.1002/num.1690110508.

Dawson, C., & Kirby, R. (2001). High resolution schemes for conservation laws with locally varying time steps. *SIAM Journal on Scientific Computing*, *22*, 2256–2281. doi:10.1137/S1064827500367737.

Deb, R., & Jenny, P. (2017a). Finite volume–based modeling of flow-induced shear failure along fracture manifolds. *International Journal for Numerical and Analytical Methods in Geomechanics*, *41*, 1922–1942. doi:doi.org/10.1002/nag.2707.

Deb, R., & Jenny, P. (2017b). Modeling of shear failure in fractured reservoirs with a porous matrix. *Computational Geosciences*, *21*, 1119–1134. doi:10.1007/s10596-017-9680-x.

Deichmann, N., & Giardini, D. (2009). Earthquakes induced by the stimulation of an enhanced geothermal system below basel (switzerland). *Seismological Research Letters*, *80*, 784–798. doi:10.1785/gssrl.80.5.784.

Delpopolo Carciopolo, L., Bonaventura, L., Scotti, A., & Formaggia, L. (2019). A conservative implicit multirate method for hyperbolic problems. *Computational Geosciences*, *23*, 647–664. doi:10.1007/s10596-018-9764-2.

Delpopolo Carciopolo, L., Formaggia, L., Scotti, A., & Hajibeygi, H. (2020). Conservative multirate multiscale simulation of multiphase flow in heterogeneous porous media. *Journal of Computational Physics*, *404*, 109134. doi:10.1016/j.jcp.2019.109134.

Dietrich, P., Helmig, R., Sauter, M., Hötzl, H., & Köngeter, J. (2005). *Flow and Transport in Fractured Porous Media*. Berlin, Heidelberg : Springer.

Driesner, T., Gischig, V., Hertrich, M., Loew, S., Maurer, H., Mazzotti, M., Saar, M. O., Wiemer, S., Zappone, A. S., Moscariello, A., Guglielmetti, L., Valley, B., Holliger, K., Laloui, L., Lecampion, B., Krause, R., Amann, F., Meier, P., Spada, M., & Lateltin, O. (2021). *Swiss Potential for Geothermal Energy and CO2 Storage. Synthesis Report*. Zurich: ETH Zurich. doi:10.3929/ethz-b-000518184.

D'Angelo, C., & Scotti, A. (2012). A mixed finite element method for darcy flow in fractured porous media with non-matching grids. *ESAIM: Mathematical Modelling and Numerical Analysis*, *46*, 465–489. doi:10.1051/m2an/2011148.

Edery, Y., Geiger, S., & Berkowitz, B. (2016). Structural controls on anomalous transport in fractured porous rock. *Water Resources Research*, *52*, 5634–5643. doi:10.1002/2016WR018942.

Edwards, B., Kraft, T., Cauzzi, C., Kästli, P., & Wiemer, S. (2015). Seismic monitoring and analysis of deep geothermal projects in st gallen and basel, switzerland. *Geophysical Journal International*, *201*, 1022–1039. doi:10.1093/gji/ggv059.

Elsworth, D., & Yasuhara, H. (2010). Mechanical and transport constitutive models for fractures subject to dissolution and precipitation. *International Journal for Numerical and Analytical Methods in Geomechanics*, *34*, 533–549. doi:doi.org/10.1002/nag.831.

Emerick, A., & Reynolds, A. (2011). Combining sensitivities and prior information for covariance localization in the ensemble kalman filter for petroleum reservoir applications. *Computational Geosciences*, *15*, 251–269. doi:10.1007/s10596-010-9198-y.

Emerick, A. A. (2016). Analysis of the performance of ensemble-based assimilation of production and seismic data. *Journal of Petroleum Science and Engineering*, *139*, 219–239. doi:10.1016/j.petrol.2016.01.029.

Emerick, A. A., & Reynolds, A. C. (2013). Ensemble smoother with multiple data assimilation. *Computers & Geosciences*, *55*, 3–15. doi:10.1016/j.cageo.2012.03.011.

Energy Institute (2023). *Statistical Review of World Energy*. Report. URL: https://www.energyinst.org/statistical-review.

Epp, R., Schmid, F., Weber, B., & Jenny, P. (2020). Predicting vessel diameter changes to upregulate biphasic blood flow during activation in realistic microvascular networks. *Frontiers in Physiology*, *11*. doi:10.3389/fphys.2020.566303.

Eshelby, J. D., & Peierls, R. E. (1957). The determination of the elastic field of an ellipsoidal inclusion, and related problems. *Proceedings of the Royal Society of London. Series A. Mathematical and Physical Sciences*, *241*, 376–396. doi:10.1098/rspa.1957.0133.

Evensen, G. (1992). Using the extended kalman filter with a multilayer quasi-geostrophic ocean model. *Journal of Geophysical Research: Oceans*, *97*, 17905–17924. doi:10.1029/92JC01972.

Evensen, G. (1994). Sequential data assimilation with a nonlinear quasi-geostrophic model using monte carlo methods to forecast error statistics. *Journal of Geophysical Research: Oceans*, *99*, 10143–10162. doi:10.1029/94JC00572.

Evensen, G. (2003). The ensemble kalman filter: theoretical formulation and practical implementation. *Ocean Dynamics*, *53*, 343–367. doi:10.1007/s10236-003-0036-9.

Evensen, G. (2004). Sampling strategies and square root analysis schemes for the enkf. *Ocean Dynamics*, *54*, 539–560. doi:10.1007/s10236-004-0099-2.

Evensen, G. (2009). *Data Assimilation : The Ensemble Kalman Filter*. Berlin, Heidelberg: Springer. doi:10.1007/978-3-642-03711-5.

Evensen, G., Amezcua, J., Bocquet, M., Carrassi, A., Farchi, A., Fowler, A., Houtekamer, P. L., Jones, C. K., de Moraes, R. J., Pulido, M., Sampson, C., & Vossepoel, F. C. (2021). An international initiative of predicting the sars-cov-2 pandemic using ensemble data assimilation. *Foundations of Data Science*, *3*, 413–477. doi:10.3934/fods.2021001.

Evensen, G., & Eikrem, K. S. (2018). Conditioning reservoir models on rate data using ensemble smoothers. *Computational Geosciences*, *22*, 1251–1270. doi:10.1007/s10596-018-9750-8.

Evensen, G., & van Leeuwen, P. J. (2000). An ensemble kalman smoother for nonlinear dynamics. *Monthly Weather Review*, *128*, 1852–1867. doi:10.1175/1520-0493(2000)128<1852:AEKSFN>2.0.CO;2.

Evensen, G., Vossepoel, F. C., & van Leeuwen, P. J. (2022). *Data Assimilation Fundamentals: A Unified Formulation of the State and Parameter Estimation Problem*. Cham: Springer Nature.

Flemisch, B., Berre, I., Boon, W., Fumagalli, A., Schwenck, N., Scotti, A., Stefansson, I., & Tatomir, A. (2018). Benchmarks for single-phase flow in fractured porous media. *Advances in Water Resources*, *111*, 239–258. doi:10.1016/j.advwatres.2017.10.036.

Flemisch, B., Nordbotten, J. M., Fernø, M., Juanes, R., Both, J. W., Class, H., Delshad, M., Doster, F., Ennis-King, J., Franc, J., Geiger, S., Gläser, D., Green, C., Gunning, J., Hajibeygi, H., Jackson, S. J., Jammoul, M., Karra, S., Li, J., Matthäi, S. K., Miller, T., Shao, Q., Spurin, C., Stauffer, P., Tchelepi, H., Tian, X., Viswanathan, H., Voskov, D., Wang, Y., Wapperom, M., Wheeler, M. F., Wilkins, A., Youssef, A. A., & Zhang, Z. (2024). The fluidflower validation benchmark study for the storage of CO2. *Transport in Porous Media*, *151*, 865–912. doi:10.1007/s11242-023-01977-7.

Geiger, S., Cortis, A., & Birkholzer, J. T. (2010). Upscaling solute transport in naturally fractured porous media with the continuous time random walk method. *Water Resources Research*, *46*. doi:10.1029/2010WR009133.

Geiger, S., Roberts, S., Matthäi, S. K., Zoppou, C., & Burri, A. (2004). Combining finite element and finite volume methods for efficient multiphase flow simulations in highly heterogeneous and structurally complex geologic media. *Geofluids*, *4*, 284–299. doi:10.1111/j.1468-8123.2004.00093.x.

Genter, A., Castaing, C., Dezayes, C., Tenzer, H., Traineau, H., & Villemin, T. (1997). Comparative analysis of direct (core) and indirect (borehole imaging tools) collection of fracture data in the hot dry rock soultz reservoir (france). *Journal of Geophysical Research: Solid Earth*, *102*, 15419–15431. doi:10.1029/97JB00626.

Ghil, M., & Malanotte-Rizzoli, P. (1991). Data assimilation in meteorology and oceanography. In R. Dmowska, & B. Saltzman (Eds.), *Advances in Geophysics* (pp. 141–266). Elsevier volume 33. doi:10.1016/S0065-2687(08)60442-2.

Gischig, V. S., Giardini, D., Amann, F., Hertrich, M., Krietsch, H., Loew, S., Maurer, H., Villiger, L., Wiemer, S., Bethmann, F., Brixel, B., Doetsch, J., Doonechaly, N. G., Driesner, T., Dutler, N., Evans, K. F., Jalali, M., Jordan, D., Kittilä, A., Ma, X., Meier, P., Nejati, M., Obermann, A., Plenkers, K., Saar, M. O., Shakas, A., & Valley, B. (2020). Hydraulic stimulation and fluid circulation experiments in underground laboratories: Stepping up the scale towards engineered geothermal systems. *Geomechanics for Energy and the Environment*, *24*, 100175. doi:10.1016/j.gete.2019.100175.

Gläser, D., Flemisch, B., Class, H., & Helmig, R. (2020). Frackit: a framework for stochastic fracture network generation and analysis. *Journal of Open Source Software*, *5*, 2291. doi:10.21105/joss.02291.

Gordon, N., Salmond, D., & Smith, A. (1993). Novel approach to nonlinear/non-gaussian bayesian state estimation. In *IEE Proceedings F (Radar and Signal Processing)* (pp. 107–113). volume 140. doi:10.1049/ip-f-2.1993.0015.

Griffith, A. A. (1921). VI. The phenomena of rupture and flow in solids. *Philosophical Transactions of the Royal Society of London. Series A, Containing Papers of a Mathematical or Physical Character*, *221*, 163–198. doi:10.1098/rsta.1921.0006.

Gunnarsson, I., Aradóttir, E. S., Oelkers, E. H., Clark, D. E., Arnarson, M. Þ., Sigfússon, B., Snæbjörnsdóttir, S. Ó., Matter, J. M., Stute, M., Júlíusson, B. M., & Gíslason, S. R. (2018). The rapid and cost-effective capture and subsurface mineral storage of carbon and sulfur at the carbfix2 site. *International Journal of Greenhouse Gas Control*, *79*, 117–126. doi:10.1016/j.ijggc.2018.08.014.

Gutmanis, J., Ardèvol i Oró, L., Díez-Canseco, D., Chebbihi, L., Awdal, A., & Cook, A. (2018). Fracture analysis of outcrop analogues to support modelling of the subseismic domain in carbonate reservoirs, south-central pyrenees. *Geological Society, London, Special Publications*, *459*, 139–156. doi:10.1144/SP459.2.

Hajibeygi, H., Karvounis, D., & Jenny, P. (2011). A hierarchical fracture model for the iterative multiscale finite volume method. *Journal of Computational Physics*, *230*, 8729–8743. doi:10.1016/j.jcp.2011.08.021.

Hamill, T. M., Whitaker, J. S., & Snyder, C. (2001). Distance-dependent filtering of background error covariance estimates in an ensemble kalman filter. *Monthly Weather Review*, *129*, 2776–2790. doi:10.1175/1520-0493(2001)129<2776:DDFOBE>2.0.CO;2.

Hargitai, H., Byrne, P. K., & Korteniemi, J. (2021). Fracture. In H. Hargitai, & Á. Kereszturi (Eds.), *Encyclopedia of Planetary Landforms* (pp. 1–11). New York, NY: Springer New York. doi:10.1007/978-1-4614-9213-9_158-1.

Haugen, V. E. J., & Evensen, G. (2002). Assimilation of sla and sst data into an ogcm for the indian ocean. *Ocean Dynamics*, *52*, 133–151. doi:10.1007/s10236-002-0014-7.

Hawkins, A., & McConnell, B. J. (1991). Influence of geology on geomechanical properties of sandstones. In *7th ISRM Congress* (pp. ISRM–7CONGRESS–1991–051). Aachen, Germany: OnePetro.

Heidbach, O., Rajabi, M., Cui, X., Fuchs, K., Müller, B., Reinecker, J., Reiter, K., Tingay, M., Wenzel, F., Xie, F., Ziegler, M. O., Zoback, M.-L., & Zoback, M. (2018). The world stress map database release 2016: Crustal stress pattern across scales. *Tectonophysics*, *744*, 484–498. doi:doi.org/10.1016/j.tecto.2018.07.007.

Hendricks Franssen, H. J., & Kinzelbach, W. (2008). Real-time groundwater flow modeling with the ensemble kalman filter: Joint estimation of states and parameters and the filter inbreeding problem. *Water Resources Research*, *44*. doi:10.1029/2007WR006505.

Hill, A. C., & Thomas, G. W. (1985). A new approach for simulating complex fractured reservoirs. In *Middle East Oil Technical Conference and Exhibition* (pp. SPE–13537–MS). doi:10.2118/13537-MS.

Horii, H., & Nemat-Nasser, S. (1986). Brittle failure in compression: Splitting, faulting and brittle-ductile transition. *Philosophical transactions of the Royal Society of London. Series A: Mathematical and physical sciences*, *319*, 337–374. doi:10.1098/rsta.1986.0101.

Houtekamer, P. L., & Mitchell, H. L. (1998). Data assimilation using an ensemble kalman filter technique. *Monthly Weather Review*, *126*, 796–811. doi:10.1175/1520-0493(1998)126<0796:DAUAEK>2.0.CO;2.

Houtekamer, P. L., & Mitchell, H. L. (2001). A sequential ensemble kalman filter for atmospheric data assimilation. *Monthly Weather Review*, *129*, 123–137. doi:10.1175/1520-0493(2001)129<0123:ASEKFF>2.0.CO;2.

Houtekamer, P. L., & Zhang, F. (2016). Review of the ensemble kalman filter for atmospheric data assimilation. *Monthly Weather Review*, *144*, 4489–4532. doi:10.1175/MWR-D-15-0440.1.

Huang, H., Long, T. A., Wan, J., & Brown, W. P. (2011). On the use of enriched finite element method to model subsurface features in porous media flow problems. *Computational Geosciences*, *15*, 721–736. doi:10.1007/s10596-011-9239-1.

Humpherys, J., Redd, P., & West, J. (2012). A fresh look at the kalman filter. *SIAM Review*, *54*, 801–823. doi:10.1137/100799666.

Hyman, J. D., Karra, S., Makedonska, N., Gable, C. W., Painter, S. L., & Viswanathan, H. S. (2015). dfnworks: A discrete fracture network framework for modeling subsurface flow and transport. *Computers & Geosciences*, *84*, 10–19. doi:10.1016/j.cageo.2015.08.001.

Häring, M. O., Schanz, U., Ladner, F., & Dyer, B. C. (2008). Characterisation of the basel 1 enhanced geothermal system. *Geothermics*, *37*, 469–495. doi:10.1016/j.geothermics.2008.06.002.

Hægland, H., Assteerawatt, A., Dahle, H. K., Eigestad, G. T., & Helmig, R. (2009). Comparison of cell- and vertex-centered discretization methods for flow in a two-dimensional discrete-fracture–matrix system. *Advances in Water Resources*, *32*, 1740–1755. doi:10.1016/j.advwatres.2009.09.006.

Irwin, G. R. (1957). Analysis of stresses and strains near the end of a crack traversing a plate. *Journal of Applied Mechanics*, *24*, 361–364. doi:10.1115/1.4011547.

Jaeger, J. C., Cook, N. G. W., & Zimmerman, R. W. (2007). *Fundamentals of rock mechanics*. (4th ed.). Malden: Blackwell Publishing.

Jafarpour, B., & McLaughlin, D. B. (2008). History matching with an ensemble kalman filter and discrete cosine parameterization. *Computational Geosciences*, *12*, 227–244. doi:10.1007/s10596-008-9080-3.

Jenny, P. (2020). Time adaptive conservative finite volume method. *Journal of Computational Physics*, *403*, 109067. doi:10.1016/j.jcp.2019.109067.

Jenny, P., Tchelepi, H. A., & Lee, S. H. (2009). Unconditionally convergent nonlinear solver for hyperbolic conservation laws with s-shaped flux functions. *Journal of Computational Physics*, *228*, 7497–7512. doi:10.1016/j.jcp.2009.06.032.

Jia, Y., Tsang, C.-F., Hammar, A., & Niemi, A. (2022). Hydraulic stimulation strategies in enhanced geothermal systems (egs): a review. *Geomechanics and Geophysics for Geo-Energy and Geo-Resources*, *8*, 211. doi:10.1007/s40948-022-00516-w.

Jing, L., & Stephansson, O. (2007). 10 - discrete fracture network (dfn) method. In L. Jing, & O. Stephansson (Eds.), *Developments in Geotechnical Engineering* (pp. 365–398). Elsevier volume 85. doi:10.1016/S0165-1250(07)85010-3.

Johnston, P. B., Atkinson, T. C., Odling, N. E., & Barker, J. A. (2005). Models of tracer breakthrough and permeability in simple fractured porous media. *Geological Society, London, Special Publications*, *249*, 91–102. doi:10.1144/GSL.SP.2005.249.01.08.

Kalman, R. E. (1960). A new approach to linear filtering and prediction problems. *Journal of Basic Engineering*, *82*, 35–45. doi:10.1115/1.3662552.

Karami, A., & Stead, D. (2008). Asperity degradation and damage in the direct shear test: A hybrid fem/dem approach. *Rock Mechanics and Rock Engineering*, *41*, 229–266. doi:10.1007/s00603-007-0139-6.

Karimi-Fard, M., Durlofsky, L. J., & Aziz, K. (2004). An efficient discrete-fracture model applicable for general-purpose reservoir simulators. *SPE Journal*, *9*, 227–236. doi:10.2118/88812-PA.

Kasap, E., & Lake, L. W. (1990). Calculating the effective permeability tensor of a gridblock. *SPE Formation Evaluation*, *5*, 192–200. doi:10.2118/18434-PA.

Kato, H., Yoshizawa, A., Ueno, G., & Obayashi, S. (2015). A data assimilation methodology for reconstructing turbulent flows around aircraft. *Journal of Computational Physics*, *283*, 559–581. doi:10.1016/j.jcp.2014.12.013.

Kazemi, H., Merrill, J., L. S., Porterfield, K. L., & Zeman, P. R. (1976). Numerical simulation of water-oil flow in naturally fractured reservoirs. *Society of Petroleum Engineers Journal*, *16*, 317–326. doi:10.2118/5719-PA.

Keller, J., Hendricks Franssen, H.-J., & Marquart, G. (2018). Comparing seven variants of the ensemble kalman filter: How many synthetic experiments are needed? *Water Resources Research*, *0*. doi:10.1029/2018WR023374.

Kleb, W. L., Batina, J. T., & Williams, M. H. (1992). Temporal adaptive euler/navier-stokes algorithm involving unstructured dynamic meshes. *AIAA Journal*, *30*, 1980–1985. doi:10.2514/3.11169.

Koren, B. (1993). A robust upwind discretization method for advection, diffusion and source terms. In C. B. Vreugdenhil, & B. Koren (Eds.), *Numerical Methods for Advection-Diffusion Problems* Notes on Numerical Fluid Mechanics (pp. 117–138). Braunschweig/Wiesbaden: Vieweg.

Kulka, V., & Jenny, P. (2022). Temporally adaptive conservative scheme for unsteady compressible flow. *Journal of Computational Physics*, *455*, 110918. doi:10.1016/j.jcp.2021.110918.

Le, D. H., Emerick, A. A., & Reynolds, A. C. (2016). An adaptive ensemble smoother with multiple data assimilation for assisted history matching. *SPE Journal*, *21*, 2195–2207. doi:10.2118/173214-PA.

van Leeuwen, P. J. (2020). A consistent interpretation of the stochastic version of the ensemble kalman filter. *Quarterly Journal of the Royal Meteorological Society*, *146*, 2815–2825. doi:10.1002/qj.3819.

van Leeuwen, P. J., & Evensen, G. (1996). Data assimilation and inverse methods in terms of a probabilistic formulation. *Monthly Weather Review*, *124*, 2898–2913. doi:10.1175/1520-0493(1996)124<2898:DAAIMI>2.0.CO;2.

van Leeuwen, P. J., Künsch, H. R., Nerger, L., Potthast, R., & Reich, S. (2019). Particle filters for high-dimensional geoscience applications: A review. *Quarterly Journal of the Royal Meteorological Society*, *145*, 2335–2365. doi:10.1002/qj.3551.

Lei, Q., & Barton, N. (2022). On the selection of joint constitutive models for geomechanics simulation of fractured rocks. *Computers and Geotechnics*, *145*, 104707. doi:10.1016/j.compgeo.2022.104707.

Lei, Q., Latham, J.-P., & Tsang, C.-F. (2017). The use of discrete fracture networks for modelling coupled geomechanical and hydrological behaviour of fractured rocks. *Computers and Geotechnics*, *85*, 151–176. doi:10.1016/j.compgeo.2016.12.024.

LeVeque, R. J. (2002). High-resolution methods. In *Finite Volume Methods for Hyperbolic Problems* Cambridge Texts in Applied Mathematics (pp. 100–128). Cambridge: Cambridge University Press. doi:10.1017/CBO9780511791253.007.

Li, L., & Lee, S. H. (2008). Efficient field-scale simulation of black oil in a naturally fractured reservoir through discrete fracture networks and homogenized media. *SPE Reservoir Evaluation & Engineering*, *11*, 750–758. doi:10.2118/103901-PA.

Li, L., Zhou, H., Gómez-Hernández, J. J., & Hendricks Franssen, H.-J. (2012). Jointly mapping hydraulic conductivity and porosity by assimilating concentration data via ensemble kalman filter. *Journal of Hydrology*, *428-429*, 152–169. doi:https://doi.org/10.1016/j.jhydrol.2012.01.037.

Li, Z., Zhang, H., Bailey, S. C. C., Hoagg, J. B., & Martin, A. (2017). A data-driven adaptive reynolds-averaged navier–stokes k–ω model for turbulent flow. *Journal of Computational Physics*, *345*, 111–131. doi:10.1016/j.jcp.2017.05.009.

Lie, K., & Møyner, O. (Eds.) (2021). *Advanced Modeling with the MATLAB Reservoir Simulation Toolbox*. Cambridge: Cambridge University Press. doi:10.1017/9781009019781.

Liem, M., Conti, G., Matthai, S. K., & Jenny, P. (2023a). Data collection: Prior with far-field stress approximation for ensemble-based data assimilation in naturally fractured reservoirs. ETH Zurich. doi:10.3929/ethz-b-000632502.

Liem, M., Conti, G., Matthai, S. K., & Jenny, P. (2023b). Prior with far-field stress approximation for ensemble-based data assimilation in naturally fractured reservoirs. *ESS Open Archive*, *Preprint*. doi:10.22541/essoar.169651311.16504949/v1. Submitted to Water Resources Research.

Liem, M., & Jenny, P. (2020). Two-stage ensemble kalman filter approach for data assimilation applied to flow in fractured media. In *ECMOR 2020* (pp. 1–14). European Association of Geoscientists & Engineers volume 2020. doi:10.3997/2214-4609.202035126.

Liem, M., Matthai, S., & Jenny, P. (2022a). Adaptive conservative time integration for transport in fractured porous media. *Advances in Water Resources*, *165*, 104213. doi:10.1016/j.advwatres.2022.104213.

Liem, M., Matthai, S. K., & Jenny, P. (2022b). Estimation of fracture aperture in naturally fractured reservoirs using an ensemble smoother with multiple data assimilation. In *ECMOR 2022* (pp. 1–18). European Association of Geoscientists & Engineers volume 2022. doi:10.3997/2214-4609.202244068.

Lim, E., Shi, Y., Leo, H. L., & Al Abed, A. (2023). Editorial: Data assimilation in cardiovascular medicine: Merging experimental measurements with physics-based computational models. *Frontiers in Physiology*, *14*. doi:10.3389/fphys.2023.1153861.

Liu, E., & Martinez, A. (2012). *Seismic Fracture Characterization*. Oxford: EAGE.

Liu, Q., Xue, L., Sarout, J., Lin, Q., Pan, W., Liu, Y., & Feng, R. (2022). Automatic history matching of multistage fractured shale gas reservoir constrained by microseismic data. *Journal of Petroleum Science and Engineering*, *213*, 110357. doi:doi.org/10.1016/j.petrol.2022.110357.

Liu, R., Li, B., Jiang, Y., & Huang, N. (2016). Review: Mathematical expressions for estimating equivalent permeability of rock fracture networks. *Hydrogeology Journal*, *24*, 1623–1649. doi:10.1007/s10040-016-1441-8.

Liu, X., Dai, C., Xue, L., & Ji, B. (2018). Estimation of fracture distribution in a co2-eor system through ensemble kalman filter. *Greenhouse Gases: Science and Technology*, *8*, 257–278. doi:10.1002/ghg.1735.

Long, J. C. S., & Witherspoon, P. A. (1985). The relationship of the degree of interconnection to permeability in fracture networks. *Journal of Geophysical Research: Solid Earth*, *90*, 3087–3098. doi:doi.org/10.1029/JB090iB04p03087.

Lorenc, A. C. (1986). Analysis methods for numerical weather prediction. *Quarterly Journal of the Royal Meteorological Society*, *112*, 1177–1194. doi:10.1002/qj.49711247414.

Lorentzen, R. J., Fjelde, K. K., Frøyen, J., Lage, A. C. V. M., Nævdal, G., & Vefring, E. H. (2001). Underbalanced and low-head drilling operations: Real time interpretation of measured data and operational support. In *SPE Annual Technical Conference and Exhibition* (p. 12). SPE: Society of Petroleum Engineers. doi:10.2118/71384-MS.

Lu, J., Kordi, M., Hovorka, S. D., Meckel, T. A., & Christopher, C. A. (2013). Reservoir characterization and complications for trapping mechanisms at cranfield co2 injection site. *International Journal of Greenhouse Gas Control*, *18*, 361–374. doi:doi.org/10.1016/j.ijggc.2012.10.007.

Lu, L., & Zhang, D. (2015). Assisted history matching for fractured reservoirs by use of hough-transform-based parameterization. *SPE Journal*, *20*, 942–961. doi:10.2118/176024-PA.

Luo, X., & Bhakta, T. (2020). Automatic and adaptive localization for ensemble-based history matching. *Journal of Petroleum Science and Engineering*, *184*, 106559. doi:10.1016/j.petrol.2019.106559.

Matthäi, S. K., & Belayneh, M. (2004). Fluid flow partitioning between fractures and a permeable rock matrix. *Geophysical Research Letters*, *31*. doi:10.1029/2003GL019027.

Matthäi, S. K., Geiger, S., & Roberts, S. G. (2001). *Complex Systems Platform: CSP3D3.0. user's guide*. Report ETH, Eidgenössische Technische Hochschule Zürich, Institut für Isotopengeologie und Mineralische Rohstoffe. doi:10.3929/ethz-a-004432279.

Matthäi, S. K., Geiger, S., Roberts, S. G., Paluszny, A., Belayneh, M., Burri, A., Mezentsev, A., Lu, H., Coumou, D., Driesner, T., & Heinrich, C. A. (2007). Numerical simulation of multi-phase fluid flow in structurally complex reservoirs. *Geological Society, London, Special Publications*, *292*, 405. doi:10.1144/SP292.22.

Metz, B., Davidson, O., De Coninck, H. C., Loos, M., & Meyer, L. (2005). *IPCC special report on carbon dioxide capture and storage*. Cambridge: Cambridge University Press.

Milliotte, C., Jonoud, S., Wennberg, O. P., Matthäi, S. K., Jurkiw, A., & Mosser, L. (2018). Well-data-based discrete fracture and matrix modelling and flow-based upscaling of multi-

layer carbonate reservoir horizons. *Geological Society, London, Special Publications*, *459*, 191. doi:10.1144/SP459.7.

Moinfar, A., Varavei, A., Sepehrnoori, K., & Johns, R. T. (2013). Development of an efficient embedded discrete fracture model for 3d compositional reservoir simulation in fractured reservoirs. *SPE Journal*, *19*, 289–303. doi:10.2118/154246-PA.

Multiphysics, C. (2013). Comsol multiphysics reference manual. *COMSOL: Grenoble, France*, *1084*, 834.

Neuman, S. P. (1977). Theoretical derivation of darcy's law. *Acta Mechanica*, *25*, 153–170. doi:10.1007/BF01376989.

Nutaro, J., Zeigler, B. P., Jammalamadaka, R., & Akerkar, S. (2003). Discrete event solution of gas dynamics within the evs framework. In P. M. A. Sloot, D. Abramson, A. V. Bogdanov, Y. E. Gorbachev, J. J. Dongarra, & A. Y. Zomaya (Eds.), *Computational Science – ICCS 2003* (pp. 319–328). Springer Berlin Heidelberg. doi:10.1007/3-540-44864-0_33.

Nævdal, G., Johnsen, L. M., Aanonsen, S. I., & Vefring, E. H. (2005). Reservoir monitoring and continuous model updating using ensemble kalman filter. *SPE Journal*, *10*, 66–74. doi:10.2118/84372-PA.

Oda, M. (1985). Permeability tensor for discontinuous rock masses. *Géotechnique*, *35*, 483–495. doi:10.1680/geot.1985.35.4.483.

Odling, N. E. (1997). Scaling and connectivity of joint systems in sandstones from western norway. *Journal of Structural Geology*, *19*, 1257–1271. doi:10.1016/S0191-8141(97)00041-2.

Ojo, O., & Brook, N. (1990). The effect of moisture on some mechanical properties of rock. *Mining Science and Technology*, *10*, 145–156. doi:10.1016/0167-9031(90)90158-0.

Osher, S., & Sanders, R. (1983). Numerical approximations to nonlinear conservation laws with locally varying time and space grids. *Mathematics of Computation*, *41*, 321–336. doi:10.1090/S0025-5718-1983-0717689-8.

O'Sullivan, M., Yeh, A., & Mannington, W. (2010). Renewability of geothermal resources. *Geothermics*, *39*, 314–320. doi:10.1016/j.geothermics.2010.09.003.

Paluszny, A., Matthäi, S. K., & Hohmeyer, M. (2007). Hybrid finite element–finite volume discretization of complex geologic structures and a new simulation workflow demonstrated on fractured rocks. *Geofluids*, *7*, 186–208. doi:10.1111/j.1468-8123.2007.00180.x.

Paluszny, A., Thomas, R. N., Saceanu, M. C., & Zimmerman, R. W. (2020). Hydro-mechanical interaction effects and channelling in three-dimensional fracture networks undergoing growth and nucleation. *Journal of Rock Mechanics and Geotechnical Engineering*, *12*, 707–719. doi:10.1016/j.jrmge.2020.04.004.

Pervaiz, M. M., & Baron, J. R. (1989). Spatiotemporal adaptation algorithm for two-dimensional reacting flows. *AIAA Journal*, *27*, 1368–1376. doi:10.2514/3.10273.

Pezzulli, E., Nejati, M., Salimzadeh, S., Matthäi, S. K., & Driesner, T. (2022a). An enhanced j-integral for hydraulic fracture mechanics. *International Journal for Numerical and Analytical Methods in Geomechanics*, *46*, 2163–2190. doi:10.1002/nag.3383.

Pezzulli, E., Nejati, M., Salimzadeh, S., Matthäi, S. K., & Driesner, T. (2022b). Finite element simulations of hydraulic fracturing: A comparison of algorithms for extracting the propagation velocity of the fracture. *Engineering Fracture Mechanics*, *274*, 108783. doi:10.1016/j.engfracmech.2022.108783.

Phillips, O. M. (1990). Flow-controlled reactions in rock fabrics. *Journal of Fluid Mechanics*, *212*, 263–278. doi:10.1017/S0022112090001951.

Phillips, O. M. (1991). *Flow and reactions in permeable rocks*. Cambridge [etc.]: Cambridge University Press.

Ping, J., Al-Hinai, O., & Wheeler, M. F. (2017). Data assimilation method for fractured reservoirs using mimetic finite differences and ensemble kalman filter. *Computational Geosciences*, *21*, 781–794. doi:10.1007/s10596-017-9659-7.

Ping, J., & Zhang, D. (2013). History matching of fracture distributions by ensemble kalman filter combined with vector based level set parameterization. *Journal of Petroleum Science and Engineering*, *108*, 288–303. doi:10.1016/j.petrol.2013.04.018.

Piroozmand, P., Brenner, O., & Jenny, P. (2023). Dimensionality reduction for regularization of sparse data-driven rans simulations. *Journal of Computational Physics*, *492*, 112404. doi:10.1016/j.jcp.2023.112404.

Pollard, D. D., & Aydin, A. (1988). Progress in understanding jointing over the past century. *GSA Bulletin*, *100*, 1181–1204. doi:10.1130/0016-7606(1988)100<1181:PIUJOT>2.3.CO;2.

Pollard, D. D., & Segall, P. (1987). 8 - theoretical displacements and stresses near fractures in rock: With applications to faults, joints, veins, dikes, and solution surfaces. In B. K. Atkinson (Ed.), *Fracture Mechanics of Rock* (pp. 277–349). London: Academic Press. doi:10.1016/B978-0-12-066266-1.50013-2.

Prensky, S. E. (1999). Advances in borehole imaging technology and applications. *Geological Society, London, Special Publications*, *159*, 1. doi:10.1144/GSL.SP.1999.159.01.01.

Quaife, T., Lewis, P., De Kauwe, M., Williams, M., Law, B. E., Disney, M., & Bowyer, P. (2008). Assimilating canopy reflectance data into an ecosystem model with an ensemble kalman filter. *Remote Sensing of Environment*, *112*, 1347–1364. doi:10.1016/j.rse.2007.05.020.

Rafiee, J., & Reynolds, A. C. (2017). Theoretical and efficient practical procedures for the generation of inflation factors for es-mda. *Inverse Problems*, *33*, 115003. doi:10.1088/1361-6420/aa8cb2.

Rahman, M. K., Hossain, M. M., & Rahman, S. S. (2002). A shear-dilation-based model for evaluation of hydraulically stimulated naturally fractured reservoirs. *International Journal for Numerical and Analytical Methods in Geomechanics*, *26*, 469–497. doi:10.1002/nag.208.

Rawnsley, K. D., Peacock, D. C. P., Rives, T., & Petit, J. P. (1998). Joints in the mesozoic sediments around the bristol channel basin. *Journal of Structural Geology*, *20*, 1641–1661. doi:doi.org/10.1016/S0191-8141(98)00070-4.

Reichenberger, V., Jakobs, H., Bastian, P., & Helmig, R. (2006). A mixed-dimensional finite volume method for two-phase flow in fractured porous media. *Advances in Water Resources*, *29*, 1020–1036. doi:10.1016/j.advwatres.2005.09.001.

Renshaw, C. E. (1995). On the relationship between mechanical and hydraulic apertures in rough-walled fractures. *Journal of Geophysical Research: Solid Earth*, *100*, 24629–24636. doi:10.1029/95JB02159.

Sakov, P., & Bertino, L. (2011). Relation between two common localisation methods for the enkf. *Computational Geosciences*, *15*, 225–237. doi:10.1007/s10596-010-9202-6.

Sakov, P., Evensen, G., & Bertino, L. (2010). Asynchronous data assimilation with the enkf. *Tellus A*, *62*, 24–29. doi:10.1111/j.1600-0870.2009.00417.x.

Schwenck, N., Flemisch, B., Helmig, R., & Wohlmuth, B. I. (2015). Dimensionally reduced flow models in fractured porous media: crossings and boundaries. *Computational Geosciences*, *19*, 1219–1230. doi:10.1007/s10596-015-9536-1.

Seabra, G. S., de Hoop, S., Voskov, D., & Vossepoel, F. C. (2023). Understanding of naturally fractured geothermal reservoirs using data assimilation. In *48th Workshop on Geothermal Reservoir Engineering*.

Segall, P., & Pollard, D. D. (1980). Mechanics of discontinuous faults. *Journal of Geophysical Research: Solid Earth*, *85*, 4337–4350. doi:10.1029/JB085iB08p04337.

Shao, Q., Matthai, S., Driesner, T., & Gross, L. (2021). Predicting plume spreading during co2 geo-sequestration: benchmarking a new hybrid finite element–finite volume compositional simulator with asynchronous time marching. *Computational Geosciences*, *25*, 299–323. doi:10.1007/s10596-020-10006-1.

Shao, Q., Matthäi, S. K., & Gross, L. (2019). Efficient modelling of solute transport in heterogeneous media with discrete event simulation. *Journal of Computational Physics*, *384*, 134–150. doi:10.1016/j.jcp.2019.01.026.

Sibson, R. H. (1985). Stopping of earthquake ruptures at dilational fault jogs. *Nature*, *316*, 248–251. doi:10.1038/316248a0.

Singhal, B. B. S., & Gupta, R. P. (2010). *Applied Hydrogeology of Fractured Rocks : Second Edition*. (2nd ed.). Dordrecht: Springer Netherlands. doi:10.1007/978-90-481-8799-7.

Skjervheim, J. A., Evensen, G., Aanonsen, S. I., Ruud, B. O., & Johansen, T. A. (2007). Incorporating 4d seismic data in reservoir simulation models using ensemble kalman filter. *SPE Journal*, *12*, 282–292. doi:10.2118/95789-PA.

Skjervheim, J.-a., Evensen, G., Hove, J., & Vabø, J. G. (2011). An ensemble smoother for assisted history matching. In *SPE Reservoir Simulation Symposium* (p. 15). SPE: Society of Petroleum Engineers. doi:10.2118/141929-MS.

Smith, M. (2009). *ABAQUS/Standard User's Manual, Version 6.9*. Providence, RI: Dassault Systèmes Simulia Corp.

Stefansson, I., Berre, I., & Keilegavlen, E. (2021). A fully coupled numerical model of thermo-hydro-mechanical processes and fracture contact mechanics in porous media. *Computer Methods in Applied Mechanics and Engineering*, *386*, 114122. doi:10.1016/j.cma.2021.114122.

Stefansson, V. (2000). The renewability of geothermal energy. In *Proceedings of the 2000 World Geothermal Congress* (pp. 883–888). Kyushu-Tohoku, Japan.

Szwedzicki, T. (2007). A hypothesis on modes of failure of rock samples tested in uniaxial compression. *Rock Mechanics and Rock Engineering*, *40*, 97–104. doi:10.1007/s00603-006-0096-5.

Taylor, W. L., Pollard, D. D., & Aydin, A. (1999). Fluid flow in discrete joint sets: Field observations and numerical simulations. *Journal of Geophysical Research: Solid Earth*, *104*, 28983–29006. doi:10.1029/1999JB900179.

Thomas, R. N., Paluszny, A., & Zimmerman, R. W. (2020). Permeability of three-dimensional numerically grown geomechanical discrete fracture networks with evolving geometry and mechanical apertures. *Journal of Geophysical Research: Solid Earth*, *125*, e2019JB018899. doi:doi.org/10.1029/2019JB018899.

Todaro, V., D'Oria, M., Tanda, M. G., & Gómez-Hernández, J. J. (2021). Ensemble smoother with multiple data assimilation to simultaneously estimate the source location and the release history of a contaminant spill in an aquifer. *Journal of Hydrology*, *598*, 126215. doi:10.1016/j.jhydrol.2021.126215.

Torsvik, T. H., Sturt, B. A., Ramsay, D. M., Bering, D., & Fluge, P. R. (1988). Palaeomagnetism, magnetic fabrics and the structural style of the hornelen old red sandstone, western norway. *Journal of the Geological Society*, *145*, 413–430. doi:10.1144/gsjgs.145.3.0413.

Townend, J., & Zoback, M. D. (2000). How faulting keeps the crust strong. *Geology*, *28*, 399–402. doi:10.1130/0091-7613(2000)28<399:HFKTCS>2.0.CO;2.

Tsang, C.-F., Neretnieks, I., & Tsang, Y. (2015). Hydrologic issues associated with nuclear waste repositories. *Water Resources Research*, *51*, 6923–6972. doi:10.1002/2015WR017641.

Tsang, Y. W. (1992). Usage of "equivalent apertures" for rock fractures as derived from hydraulic and tracer tests. *Water Resources Research*, *28*, 1451–1455. doi:10.1029/92WR00361.

Ucar, E., Berre, I., & Keilegavlen, E. (2018). Three-dimensional numerical modeling of shear stimulation of fractured reservoirs. *Journal of Geophysical Research: Solid Earth*, *123*, 3891–3908. doi:10.1029/2017JB015241.

Uleberg, K., & Kleppe, J. (1996). Dual porosity, dual permeability formulation for fractured reservoir simulation. In *Norwegian university of science and technology, Trondheim RUTH Seminar, Stavanger*.

United Nations (2023). *The Sustainable Development Goals Report 2023: Special Edition*. Report United Nations New York, NY, USA. URL: https://unstats.un.org/sdgs/report/2023/.

Vilarrasa, V., Koyama, T., Neretnieks, I., & Jing, L. (2011). Shear-induced flow channels in a single rock fracture and their effect on solute transport. *Transport in Porous Media*, *87*, 503–523. doi:10.1007/s11242-010-9698-1.

Vogt, C., Marquart, G., Kosack, C., Wolf, A., & Clauser, C. (2012). Estimating the permeability distribution and its uncertainty at the egs demonstration reservoir soultz-sous-forêts using the ensemble kalman filter. *Water Resources Research*, *48*. doi:10.1029/2011WR011673.

Wang, J., Xie, H.-P., Matthai, S. K., Hu, J.-J., & Li, C.-B. (2023). The role of natural fracture activation in hydraulic fracturing for deep unconventional geo-energy reservoir stimulation. *Petroleum Science*, *20*, 2141–2164. doi:10.1016/j.petsci.2023.01.007.

Wang, Y., Voskov, D., Khait, M., & Bruhn, D. (2020). An efficient numerical simulator for geothermal simulation: A benchmark study. *Applied Energy*, *264*, 114693. doi:10.1016/j.apenergy.2020.114693.

Warren, J. E., & Root, P. J. (1963). The behavior of naturally fractured reservoirs. *Society of Petroleum Engineers Journal*, *3*, 245–255. doi:10.2118/426-PA.

Westergaard, H. M. (1939). Bearing pressures and cracks: Bearing pressures through a slightly waved surface or through a nearly flat part of a cylinder, and related problems of cracks. *Journal of Applied Mechanics*, *6*, A49–A53. doi:10.1115/1.4008919.

Willis-Richards, J., Watanabe, K., & Takahashi, H. (1996). Progress toward a stochastic rock mechanics model of engineered geothermal systems. *Journal of Geophysical Research: Solid Earth*, *101*, 17481–17496. doi:10.1029/96JB00882.

Wu, H., Fu, P., Hawkins, A. J., Tang, H., & Morris, J. P. (2021). Predicting thermal performance of an enhanced geothermal system from tracer tests in a data assimilation framework. *Water Resources Research*, *57*, e2021WR030987. doi:10.1029/2021WR030987.

Yang, B., Shao, C., Hu, X., Ngata, M. R., & Aminu, M. D. (2023). Advances in carbon dioxide storage projects: Assessment and perspectives. *Energy & Fuels*, *37*, 1757–1776. doi:10.1021/acs.energyfuels.2c03826.

Yao, M., Chang, H., Li, X., & Zhang, D. (2018). Tuning fractures with dynamic data. *Water Resources Research*, *54*, 680–707. doi:10.1002/2017WR022019.

Yao, M., Chang, H., Li, X., & Zhang, D. (2019). An integrated approach for history matching of multiscale-fractured reservoirs. *SPE Journal*, *24*, 1508–1525. doi:10.2118/195589-PA.

Zhang, K., Zhang, J., Ma, X., Yao, C., Zhang, L., Yang, Y., Wang, J., Yao, J., & Zhao, H. (2021a). History matching of naturally fractured reservoirs using a deep sparse autoencoder. *SPE Journal*, *26*, 1700–1721. doi:10.2118/205340-PA.

Zhang, X., Huang, Z., Lei, Q., Yao, J., Gong, L., Sun, Z., Yang, W., Yan, X., & Li, Y. (2021b). Impact of fracture shear dilation on long-term heat extraction in enhanced geothermal systems: Insights from a fully-coupled thermo-hydro-mechanical simulation. *Geothermics*, *96*, 102216. doi:10.1016/j.geothermics.2021.102216.

Zhang, X. D., Trepanier, J. Y., Reggio, M., & Camarero, R. (1994). Time-accurate local time stepping method based on flux updating. *AIAA Journal*, *32*, 1926–1929. doi:10.2514/3.12195.

Zhao, Z., Peng, H., Wu, W., & Chen, Y.-F. (2018). Characteristics of shear-induced asperity degradation of rock fractures and implications for solute retardation. *International Journal of Rock Mechanics and Mining Sciences*, *105*, 53–61. doi:10.1016/j.ijrmms.2018.03.012.

Zhe, L., Younis, R., & Jiang, J. (2016). A diagnostic framework for "bashed" wells in unconventional reservoirs: A numerical simulation and model selection theory approach. In *SPE/AAPG/SEG Unconventional Resources Technology Conference* (p. 17). URTEC: Unconventional Resources Technology Conference. doi:10.15530/URTEC-2016-2448463.

Zhou, H., Gómez-Hernández, J. J., Hendricks Franssen, H.-J., & Li, L. (2011). An approach to handling non-gaussianity of parameters and state variables in ensemble kalman filtering. *Advances in Water Resources*, *34*, 844–864. doi:10.1016/j.advwatres.2011.04.014.

Zimmerman, R. W. (2017). *The Imperial College Lectures in Petroleum Engineering*. WORLD SCIENTIFIC (EUROPE). doi:10.1142/q0146.

Zoback, M. D. (2007). *Reservoir Geomechanics*. Cambridge: Cambridge University Press. doi:10.1017/CBO9780511586477.

Subsurface applications such as geothermal heat extraction or CO_2 sequestration are vital for solving today's energy and climate challenges. Their reservoir rock typically consists of fractured porous media, whose fractures can greatly affect flow, transport, and mechanics. Accurate and efficient modelling of the relevant physical processes and characterising the related parameters are crucial for performance estimation and risk assessment. This simulation-based thesis aims to enhance these aspects.

Time-dependent hyperbolic partial differential equations (PDEs) are commonly used for modelling transport phenomena and seismic activity. Adaptive time stepping methods, like the adaptive conservative time integration (ACTI) scheme, improve the efficiency of explicit time integration by allowing variable local time steps. We extend ACTI to tracer transport in fractured porous media, achieving accurate results while reducing computational costs by orders of magnitude compared to global time stepping.

Limited observability of subsurface reservoirs and substantial uncertainties, particularly concerning fractures and their apertures, pose challenges to accurate modelling. Ensemble-based data assimilation (DA) methods, like the ensemble smoother with multiple data assimilation (ES-MDA), are established tools for reducing uncertainty in model parameters and improving simulation results. We demonstrate the significant impact of measurement strategies and matrix permeability on DA results, highlighting the utility of intermediate measurements during reservoir stimulation and the influence of matrix permeability on fracture parameter estimation.

Constructing a prior ensemble that accurately reflects available knowledge is crucial for ensemble-based DA methods. We introduce the far-field stress approximation (FFSA), a proxy model which projects the far-field stresses onto the fracture planes and approximates shear displacement with linear elastic theory. The FFSA efficiently generates reasonable prior realisations of fracture apertures in a realistic two-dimensional fracture network. The resulting posterior ensemble matches the flow and transport behaviour of the synthetic reference at measurement locations. It improves the estimation of the fracture apertures, markedly outperforming results from prior ensembles based on naïve stochastic approaches.

In conclusion, this thesis contributes to a more efficient and accurate simulation of fractured porous media, paving the way for improved reservoir management and decision-making in various subsurface applications.